O'Brien, P.E., Cooper, A.K., Richter, C., et al., 2001
Proceedings of the Ocean Drilling Program, Initial Reports Volume 188

5. SITE 1167[1]

Shipboard Scientific Party[2]

PRINCIPAL RESULTS

Hole 1167A

Position: 66°24.01′S, 72°17.05′E
Start hole: 2200 hr, 22 February 2000
End hole: 0825 hr, 28 February 2000
Time on hole (hr): 130.42
Seafloor (drill-pipe measurement from rig floor, mbrf): 1651.3
Distance between rig floor and sea level (m): 11.3
Water depth (drill-pipe measurement from sea level, m): 1640.0
Total depth (drill-pipe measurement from rig floor, mbrf): 2098.8
Penetration (mbsf): 447.5
Coring totals: type: APC; number: 6; cored: 39.7 m; recovered: 86.3%; type: XCB; number: 43; cored: 407.8 m; recovered: 38.5%
Lithology:

Unit I–clay and sandy clay with isolated beds of fine sand and rare lonestones
Unit II–clayey silty sand and diamictons with abundant dispersed granules and pebbles, coarse sand, and clay

Hole 1167B

Position: 66°23.98′S, 72°17.01′E
Start hole: 0825 hr, 28 February 2000
End hole: 1730 hr, 29 February 2000
Time on hole (hr): 33.08
Seafloor (drill-pipe measurement from rig floor, mbrf): 1651.3
Distance between rig floor and sea level (m): 11.3
Water depth (drill-pipe measurement from sea level, m): 1640.0
Total depth (drill-pipe measurement from rig floor, mbrf): 2098.8

[1] Examples of how to reference the whole or part of this volume.
[2] Shipboard Scientific Party addresses.

Ms 188IR-105

Penetration (mbsf): 261.8
Coring totals: Dedicated logging while drilling hole

Site 1167 is located in the middle of the Prydz Channel Trough Mouth Fan. Construction of the fan started in late Miocene to mid-Pliocene time when the Lambert Glacier formed a fast-flowing ice stream on the western side of Prydz Bay. The fan has grown most during episodes when the Lambert Glacier grounded at the shelf edge, delivering basal debris to the fan apex. This material was then redistributed by sediment gravity flows and meltwater plumes. Models of trough mouth fan sedimentation suggest that thick siliciclastic units should correspond to peaks in Antarctic ice volume, whereas periods of reduced ice volume should be represented by hemipelagic sediments. Thus, the alternation of facies should reflect the number of times the East Antarctic Ice Sheet has expanded to the shelf edge in latest Neogene time.

Hole 1167A was cored with the advanced hydraulic piston corer (APC) system to refusal at 39.7 meters below sea floor (mbsf). Coring then proceeded with the extended core barrel (XCB) system to a total depth of 447.5 mbsf. Planned drilling time at the site was shortened by 42 hr because of icebergs and a ship schedule change, and the target depth of 620 mbsf (base of the Prydz Trough Mouth Fan) was not achieved. Four icebergs approached to within 0.1 nmi of the drill site, causing a total of 27 hr delay.

The sedimentary section at Site 1167 comprises a 447.5-m-thick sequence of clayey silty sands with dispersed rock clasts with minor beds of coarse sands, clays, and sandy clays. Two lithostratigraphic units are identified.

Unit I (0–5.17 mbsf) is composed of olive and reddish brown clay and sandy clay with minor admixtures of biogenic components (e.g., as much as 2% diatoms and 1% sponge spicules). There are isolated beds of fine sand and rare lonestones. Diffuse reddish brown color bands are present in several thin intervals. The transition to Unit II is gradational. Unit I records a period of hemipelagic deposition when fine particles, biogenic material, and ice-rafted debris (IRD) settled out of the water column.

Unit II (5.17–447.5 mbsf) makes up the majority of the section at Site 1167 and is composed of one major facies (II-1) and three minor facies. Facies II-1 is composed of interbedded, poorly sorted dark gray sandy silt, silty sand, clayey sand, and clast-poor diamicton. Numerous color alternations of dark gray and dark reddish gray with sharp contacts occur between 64 and 98 mbsf. Some decimeter- to meter-scale successions of clast-poor diamicton and gravel beds are noted. Lonestones are common, with variable lithologies including granite, granite gneiss, garnet-bearing gneiss, metaquartzite, and sandstone. Dolerite, schist, conglomerate, and rare carbonized wood are also present. Sandstone and granite components vary systematically in the hole, with sandstone lonestones common below 200 mbsf and granite lonestones common above 200 mbsf. Facies II-2 is composed of gray, moderately sorted coarse sand. Grains are subrounded and predominately quartz, K-feldspar, and mafic minerals. The first occurrence of Facies II-2 downcore is at 179 mbsf. Facies II-3 is composed of dark gray clay with silt laminations, rare sand grains, and no lonestones. Sharp contacts mark the top and base of this facies. Some silt laminae converge and indicate crossbedding. Facies II-4 is composed of green gray clay with dispersed clasts, abundant foraminifers, and few nannofossils. The upper contact is sharp, and the lower contact is gradational to sharp.

Unit II (Facies II-1 and II-2) records deposition by mass transport, probably massive debris flows, as evidenced by poor sorting, abundant floating clasts, little visible grading, and a lack of biogenic components. The debris flows most likely represent deposition during glacial periods when ice extended to the shelf break and could deliver large volumes of sediment to the upper continental slope. Individual flows cannot be identified visually. The thin intervals of fine-grained sediment (Facies II-3 and II-4) are similar in appearance and composition to muddy contourites observed at Site 1165 and, hence, may denote times when contour currents were active on the fan. The silt laminae and bioturbation in Facies II-3 are not consistent with turbidite deposition. Facies II-4 may record short intervals, possibly interglacials, when pelagic deposition dominated.

Sixteen lithologic varieties of lonestones were cataloged, and they generally vary randomly in size, with only a small size increase downhole to 200 mbsf. Below ~160 mbsf, the number of lonestones per meter remains fairly consistent, except for three intervals (160–210, 300–320, and 410–420 mbsf) where there are downward increases. Systematic variations in concentration of sandstone and granite clasts (noted above) suggest that two different source areas may have delivered material to Site 1167 at different times.

X-ray diffraction (XRD) analyses show that the total clay mineral content is relatively constant throughout the hole. XRD analyses of clay types give mixed results for Units I and II, with smectite more common in Unit I and at depths below 382 mbsf than elsewhere and illite found in all samples. Further detailed analyses are likely to clarify whether changes in illite-smectite ratios relate to times of glacial advances.

Chronostratigraphy at Site 1167 is poorly controlled because of the unexpected paucity of siliceous microfossils; however, dates in Unit I are younger than 0.66 Ma, and a sample from ~215 mbsf seems to be of early or middle Pleistocene age. Foraminifers are present consistently throughout the section and include pelagic foraminifer shelf faunas in diamictons and in situ midbathyal faunas in a few samples. Changes in foraminifer faunas closely match changes detected in various lithological parameters. Age control at this time is not adequate to determine average sedimentation rates.

Magnetostratigraphic analyses identified the Matuyama/Brunhes boundary between 30 and 34 mbsf. The magnetic polarity below 34 mbsf remains mainly reversed and possibly includes the Jaramillo and Olduvai Subchrons. The concentration-dependent magnetic parameters (susceptibility and anhysteretic and isothermal remanent magnetization) indicate that magnetite concentrations have large-scale cyclic (tens to hundreds of meters) variations, which are not commonly seen. The values increase abruptly uphole at ~208 mbsf, between 113 and 151.2 mbsf, and between 55 and 78.5 mbsf, followed by a nearly linear uphole decrease. Superimposed on the large-scale cycles are small-scale variations. The anhysteretic over isothermal remanent magnetization ratio indicates that the magnetic grain size changes uphole from finer to coarser above 217 mbsf. The origin of the large-scale cycles is not yet understood, but it is likely related to systematic changes in sediment provenance caused by changes in the volume of ice from different sources and the location of areas of maximum erosion during glacial periods.

Interstitial water profiles document downhole sediment diagenesis, mixing of chemically distinct subsurface interstitial waters, and diffu-

sional exchange with modern bottom seawater. From 0 to 20 mbsf, chlorinity and sulfate increase by ~3% over seafloor values, suggesting that high-salinity last-glacial-maximum seawater is preserved. Sulfate decreases downhole from the seafloor (30 mM) to 433 mbsf (24 mM) in a stepped profile, raising the possibility that a number of "fossil" sulfate reduction zones may also be preserved. Dissolved manganese increases downhole from 15 to 20 mM between the seafloor and ~25 mbsf. Alkalinity decreases downhole from 3 to 1.3 mM between the seafloor and 40 mbsf before steadily increasing to 2 mM at 433 mbsf. From 0 to ~60 mbsf, dissolved downhole profiles of calcium (10–25 mM), magnesium (56–42 mM), potassium (12–2 mM), and lithium (30–5 mM) all suggest diagenetic silicate-clay reactions are occurring. Below 5 mbsf, dissolved silica concentrations are enriched slightly over modern bottom waters (~300 vs. ~220 mM), reflecting the absence of biogenic opal within the sediments. Calcium carbonate is a minor component in the matrix sediments throughout the hole and is slightly more abundant in lithostratigraphic Unit II than in Unit I.

The concentration of hydrocarbon gases was at background levels (4–10 ppmv) for methane, and ethane was present above detection limits only in a few cores from deeper than 350 mbsf. The organic carbon (OC) content averages ~0.4 wt% with no apparent trend with depth. Organic matter characterization by Rock-Eval pyrolysis indicates that all samples contain predominantly recycled and degraded thermally mature organic matter.

Sediment water content and void ratio decrease sharply with depth in lithostratigraphic Unit I, reflecting normal compaction. Within Unit II, these properties were relatively uniform, except for a downhole decrease at 210 mbsf, where grain density and magnetic susceptibility values also decrease abruptly. *P*-wave velocities increase at this depth. Undrained shear strength values increase uniformly throughout the hole at a lower than typical rate, possibly because of the clay mineralogy combined with the high proportions of silt and sand within the sediment. There is no evidence of sediment overcompaction.

Wireline logging operations in Hole 1167A were attempted with the triple combination (triple combo) tool string. The tool string was lowered to 151 mbsf, where an obstruction halted further progress. A conglomerate interval was noted in the cores at this depth. Log data were collected from this depth to the base of pipe at 86.9 mbsf, covering an interval of 66 m. Time constraints, poor hole conditions, and problems encountered with the lockable flapper valve resulted in a decision to switch to logging while drilling (LWD) in a new hole. Excellent spectral gamma-ray and resistivity data were recorded to 261.8 mbsf before time ran out. Resistivity data show several clay and gravel-rich beds, with high gamma-ray values for a red bed interval at 60–90 mbsf, and low values between 90 and 120 and 215 and 255 mbsf. The change to low values may be due to a reduced concentration of granitic clasts or a change from a clay-rich to a sandier matrix.

Site 1167 is the first drill site where the sedimentary fans that are common on the upper continental slope around Antarctica, seaward of glacially carved sections of the continental shelf, were directly sampled. The site reveals previously unknown large-scale (20 m to >200 m thick) cycles in magnetic susceptibility and other properties that are not yet fully explained but are likely due to systematic changes in the Lambert Glacier ice-drainage basin during Pleistocene and late Pliocene(?) time. Within the large cycles are likely many separate debris flows and interbedded hemipelagic muds that indicate times of individual advances

and retreats of the ice front to, or near, the continental shelf edge. The debris flows are well represented in the cores, but the mud intervals are sparse and may either have not been recovered or have been removed by younger flows. Because there are few age control points, it is not yet possible to determine sedimentation rates at Site 1167. If the rates are high, as we suspect from the few available age dates, then almost all sediment during the latest Neogene glacial intervals sampled at Site 1167 were deposited as debris flows on the trough mouth fan and did not reach Wild Drift (Site 1165), where sediment rates are low. Alternatively, some of the fine component of the latest Neogene glacial sediment is being carried away by deep ocean currents.

BACKGROUND AND OBJECTIVES

The Amery Ice Shelf–Lambert Glacier ice drainage system drains ~22% of the East Antarctic Ice Sheet (EAIS); therefore, Lambert Glacier responds to fluctuations in the EAIS. During Cenozoic glacial episodes, the Lambert Glacier advanced to various points on the shelf, sometimes to the shelf edge, prograding the shelf (see Figs. **F1,** p. 29, and **F2,** p. 30, in the "Leg Summary" chapter; Fig. **F1**). A major change in Prydz Bay shelf progradation took place in late Neogene time when a fast-flowing ice stream developed and excavated a channel (Prydz Channel) across the shelf on the western side of Prydz Bay (see Fig. **F3,** p. 31, in the "Leg Summary" chapter). The erosion surface marking this change can be mapped from the shelf to the continental rise (Surface PP12; Surface A of Mitzukoshi et al., 1986). Since then, basal debris carried to the shelf edge by the ice stream has been deposited in a trough mouth fan on the upper slope, similar to fans deposited on other high-latitude margins (Boulton, 1990; Larter and Cunningham, 1993). This change may reflect the earliest growth of thick ice on the Ingrid Christensen Coast, deflecting the Lambert Glacier when it advanced (O'Brien and Harris, 1996).

Grounding zone wedges formed by Lambert Glacier in the Prydz Channel are only ~80 km seaward of the current Amery Ice Shelf edge (O'Brien et al., 1999). Domack et al. (1998) used ^{14}C accelerated mass spectrometry dating of cores from the wedge crests and Prydz Channel to demonstrate that these wedges are last glacial maximum (LGM) grounding zone deposits, indicating that Lambert Glacier did not ground at the shelf edge during the LGM. This raises questions as to which glacial episodes throughout late Neogene time produced a major advance and what paleoenvironmental conditions existed when the major advance occurred. The best location to find answers to these questions is in the trough mouth fan, which received siliciclastic sediment from the ice front when the shelf eroded during major ice advances and deposited hemipelagic material during interglacials and smaller glaciations.

Site 1167 was located in the middle of the Prydz Channel Fan with the intent of drilling through a section that was reasonably complete without being so close to the shelf edge that it would have been affected by large-scale slumping (Fig. **F2**). Models of trough mouth fan sedimentation (e.g., Boulton, 1990) suggest that thick siliciclastic units should correspond to peaks in Antarctic ice volume, whereas periods of reduced ice volume should be represented by hemipelagic sediments.

F1. Location of Site 1167 on the axis of the Prydz Channel Fan, p. 38.

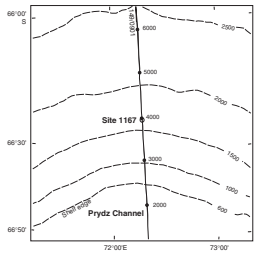

F2. Part of seismic line AGSO 149/0901 through Site 1167, p. 39.

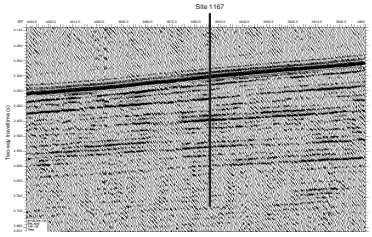

OPERATIONS

Hole 1167A

The 97-nmi voyage to Site 1167 was accomplished at an average speed of 11.4 kt. The vessel approached the Global Positioning System coordinates of proposed site PBF-6A on 22 February at 2200 hr, and a beacon was deployed at 2238 hr. Hole 1167A was spudded with the APC at 0925 hr on 23 February. The seafloor depth was established from the recovery of the first core at 1651.3 meters below sea level. APC coring proceeded without incident, but with varying recovery (77%–103%), to 39.7 mbsf (Tables T1, T2). APC refusal was reached when the core barrel of Core 6H did not achieve a full stroke and was recovered empty and partially bent. A successful Adara tool heat-flow measurement was taken at the mudline and on Core 5H (see "In Situ Temperatures," p. 30). Coring with the XCB system resumed at 1445 hr with Core 7X and continued through Core 21X to a depth of 179.2 mbsf, when operations had to be suspended because of an approaching iceberg. After pumping a 30-bbl sepiolite mud sweep, the pipe was pulled to 42.6 mbsf while the movement of the iceberg was monitored. The iceberg came to within 0.1 nmi before passing the drill site. The decision was made to run back to bottom and resume coring by 1000 hr, when the iceberg had reached a range of 0.3 nmi and was moving away from the drill site. XCB coring was resumed and continued until Core 28X was recovered from a depth of 246.5 mbsf. Another iceberg approached the drill site at 2345 hr on 24 February. This iceberg came to within 0.5 nmi of the vessel. The iceberg was monitored for an hour, during which time it passed the drill site and was moving away. The drill string was again run to bottom with the top drive still in place. At a depth of 161.7 mbsf, the driller noted 25,000 lb of downward drag. Light reaming was required to reach bottom. A core barrel was deployed, and at 0600 hr on 25 February XCB coring resumed.

Coring operations were short lived, however, when another iceberg arrived on the scene. After recovering Core 34X from a depth of 303.2 mbsf, the drill string was once again pulled back to the seafloor, with the end of the pipe placed at 42.6 mbsf.

The plan was to deploy a free fall funnel (FFF) once the pipe was at a safe depth below the seafloor. This plan had to be changed when the iceberg increased its approach speed and changed course, moving directly toward Site 1167. The decision was made to not deploy the FFF and to remain in position to pull the remaining drill pipe free of the seafloor should the need arise.

On 25 February at 2145 hr, the iceberg had moved to a distance of 1.5 nmi from the drill site and was continuing away at a rapid rate. The decision was made to deploy the FFF at this point because more icebergs were in the vicinity. The drill string was once again run into the hole. As before, the driller encountered an obstruction at 168.7 mbsf, resulting in 25,000 lb of down drag and requiring light reaming to reach the bottom.

Coring continued to Core 49X, a total depth of 447.5 mbsf. Recovery and rate of penetration were extremely variable throughout the coring cycle, as we intermittently drilled through coarse sand and gravel beds and encountered occasional dropstones. The decision was made to halt coring operations short of the 620 mbsf objective, to conserve adequate time for wireline logging and LWD operations and to meet the 15-hr

T1. Coring summary, p. 85.

T2. Expanded coring summary, p. 86.

early departure from the site required as an additional transit-time contingency.

Logging Operations in Hole 1167A

In preparation for logging, the XCB bit was placed at a depth of 86.9 mbsf and the Schlumberger wireline sheaves were rigged up. The first suite of logging tools to be deployed was the triple combo consisting of the dual-induction tool model E (DIT), high-temperature lithodensity sonde (HLDS), neutron array porosity sonde (APS), and high-temperature natural gamma sonde (HNGS). The tools were deployed on 27 February at 1905 hr; however, they could only be lowered to a depth of 148.7 mbsf, or 61.7 m below the end of the pipe. This short section was logged back to the bit. The tool could not be retracted back into the pipe without circulating the rig pumps to open the flapper valve.

While the logging tools were being recovered, it was decided that further wireline logging efforts had to be abandoned. The logging tools were laid out, and by 2400 hr on 27 February the Schlumberger wireline sheaves were rigged down. The hole was filled with a 30-m cement plug, and the pipe was pulled clear of the seafloor by 0215 hr. The bit cleared the rotary table at 0825 hr, ending Hole 1167A. Total time lost because of icebergs and ice-related problems amounted to 26.75 hr at Hole 1167A.

Hole 1167B

The vessel was offset 50 m to the northwest for a dedicated LWD/MWD hole. After waiting on weather for 4.25 hr, the drill string was tripped to the bottom and Hole 1167B was spudded at 2100 hr on 28 February. Drilling with the LWD/MWD system proceeded smoothly throughout the night with excellent results. The time allocated for this operation ran out at 0930 hr on 29 February, and drilling was halted at a depth of 261.8 mbsf. All LWD/MWD systems and the real time data telemetry equipment performed perfectly.

The hole was displaced with 66 bbl of bentonite gel mud, and the pipe was recovered, clearing the seafloor at 1110 hr on 29 February. During the pipe trip, the positioning beacons were released and recovered. While we attempted to release the third beacon, the portable command unit cable was sucked into the No. 6 thruster well. The cable was severed immediately, and the transducers head was lost. As a result, beacon No. 3 could not be released. The hydrophones and thrusters were retracted, and the drilling equipment was secured for transit. At 1730 hr on 29 February 2000, the vessel departed the last site of Leg 188 and began the transit to Hobart, Tasmania.

LITHOSTRATIGRAPHY

Hole 1167A was drilled to a maximum depth of 447.5 mbsf. We recovered a succession of predominately clayey silty sands with dispersed rock clasts and minor beds of coarse sands, clays, and sandy clays. Two lithostratigraphic units are identified (Figs. F3, F4). Unit I is composed of olive and reddish brown clay and sandy clay with minor admixtures of biogenic components. There is a gradational transition into Unit II, which makes up the majority of the section at Site 1167 and is composed of one major facies (Facies II-1) along with three minor facies. Fa-

F3. Lithostratigraphic units and facies, p. 40.

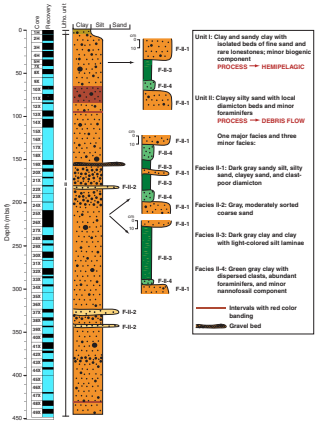

F4. Composite stratigraphic section showing core recovery, a simplified summary of lithology, age, lonestone, XRD, and color reflectance data, p. 41.

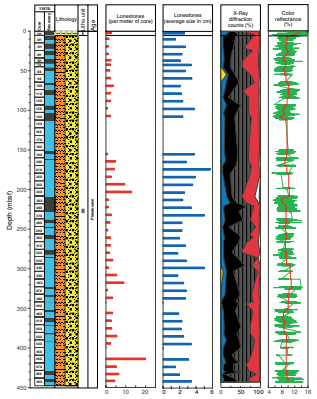

cies II-1 is composed of interbedded, poorly sorted dark gray sandy silt, silty sand, clayey sand, and clast-poor diamicton. Facies II-2 is composed of moderately sorted gray coarse sand. Facies II-3 is composed of dark gray clay with silt laminations. Facies II-4 is composed of green-gray clay with dispersed clasts, abundant foraminifers, and rare nannofossils. Calcium carbonate is a minor component in the matrix sediments throughout the hole and is slightly more abundant in Unit II than in Unit I.

Unit I

Interval: Section 188-1167A-1H-1, 0 cm, through Section 1H-CC, 15 cm
Depth: 0–5.17 mbsf
Age: Holocene to Pleistocene (<0.66 Ma)

Unit I comprises a relatively short interval at the top of the hole and is composed of olive (5Y 4/3) clay and sandy clay with isolated beds of fine sand and rare lonestones and brown to reddish brown (10YR 4/3) sandy clay (Figs. **F3, F5**). The sediments are very low in $CaCO_3$ content, with a maximum of only 0.50 wt% (see **"Organic Geochemistry,"** p. 24). Unit I contains up to 2% diatoms and 1% sponge spicules (see **"Smear Slides,"** p. 12).

Diffuse reddish brown color bands (10YR 4/3) are present in several short intervals in Unit I (188-1167A-1H-1, 143–146 cm; 1H-2, 42–58 cm, and 69–76 cm; 1H-3, 50–59 cm; and 1H-3, 140–145 cm). A normally graded sand bed is found in interval 188-1167A-1H-2, 92–106 cm (2.42–2.56 mbsf), and grades upward from granules and very coarse sand at the bottom to medium sand at the top (Fig. **F5**).

F5. Clay and sandy clay typical of Unit I, p. 43.

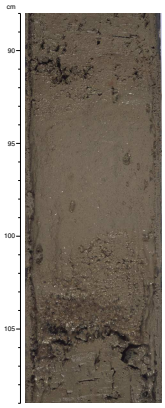

Interpretation

Unit I sediments record a period of hemipelagic deposition. This interpretation is supported by the fine-grained nature of the sediments as well as the presence of diatoms and sponge spicules (1%–2% recorded from smear slides). The lonestones that are present are likely IRD. The normally graded sand bed can be interpreted as the T_a unit in the subdivision of turbidites by Bouma (1962).

Unit II

Interval: Section 188-1167A-2H-3, 0 cm, through Section 49X-CC, 22 cm
Depth: 5.17–447.5 mbsf
Age: Pleistocene and Holocene

At the lower boundary of Unit I, there is a sharp color change and gradational transition from the clays and sandy clays into the coarser sediments of Unit II. Unit II comprises the rest of the section and is composed of four facies. Facies II-1 is the primary component of the unit and consists of diamictons and sediments characterized by abundant dispersed granules and pebbles in a matrix of varying proportions of sand, silt, and clay. Facies II-2 consists of coarse sands, Facies II-3 consists of gray clays and common silt laminations, and Facies II-4 consists of biogenic-rich green-gray clays. These three facies comprise only thin interbeds and collectively account for <2% of the sediment in Unit II. Calci-

um carbonate content is generally <1 wt% but is relatively higher than in Unit I and ranges from 0.50 to 1.25 wt%. Smear-slide data indicate that quartz and clay minerals are the primary components of the matrix sediment throughout Unit II. Heavy minerals, opaques, and garnet make up the majority of other components, but their percentages decrease below Section 188-1167A-26X-6, 90 cm.

Facies II-1

Facies II-1 consists of dark gray (5Y 4/1), very dark gray (5Y 3/1, 10YR 3/1), and reddish gray (5YR 4/2) poorly sorted sandy silt, silty sand, clayey sand, and clast-poor diamicton with dispersed granules and pebbles of varying sizes and lithologies (Figs. F3, F6). The relative proportions of sand, silt, clay, and clasts change frequently, and few clast-supported beds are present.

Lonestones are common throughout Facies II-1 and consist of variable lithologies including granite, granite gneiss, garnet-bearing gneiss, metaquartzite, and sandstone. Dolerite, schist, conglomerate, various minerals, and rare carbonized wood are also present (Fig. F7). The distribution of granite and sandstone lonestones varies systematically. From 425 to 200 mbsf, sandstone lonestones are more abundant than above 200 mbsf, whereas granite lonestones are more abundant from 200 mbsf to the top of the hole (Fig. F8).

The highest concentrations of rock clasts (>5%) are within interval 188-1167A-19X-2, 0 cm, through 24X-1, 88 cm. Several decimeter- to meter-scale successions of clast-poor diamicton are present in this interval. Clast-poor diamictons are also present in intervals 188-1167A-5H-4, 25–90 cm; 30X-4, 28–41 cm; 37X-CC, 0–10 cm; and 43X-2, 0–90 cm. Diamictons have a sandy silt or silty sand matrix. Gravel beds are interbedded with poorly sorted sandy silt in interval 188-1167A-19X-1, 124 cm, through 19X-2, 130 cm (151.6–153.1 mbsf), and are characterized by subangular to subrounded granules and small pebbles. One gravel bed in interval 188-1167A-19X-2, 50–80 cm (150.8–151.1 mbsf), is composed of ~60% clasts and 40% matrix material (Fig. F9). Additionally, sand and gravel concentrations are present in intervals 188-1167A-13X-2, 60–65 cm; 13X-4, 30–44 cm, and 65–67 cm; and 41X-3, 54–57 cm.

Numerous color alternations of dark gray (5Y 4/1) and dark reddish gray (5YR 4/2) are present in interval 188-1167A-10X-1, 8 cm, through 13X-4, 21 cm (64.38–97.59 mbsf), and minor reddish gray color banding is present in interval 1167A-48X-2, 30–40 cm (430.1–430.2 mbsf). The color contacts are fairly sharp and are both planar and wavy. No apparent lithologic change or sedimentary structures are associated with the color transitions (Fig. F10). Facies II-1 is barren of diatoms and radiolarians, whereas foraminifers are a minor component in this facies (see "Biostratigraphy and Sedimentation Rates," p. 14).

Facies II-2

Facies II-2 consists of moderately sorted gray coarse sand with rare to common dispersed granules (Fig. F3). Grains are subrounded and predominantly composed of quartz, K-feldspar, and mafic minerals. The first occurrence of sand is at the top of the core in interval 188-1167A-22X-1, 0–50 cm (179.2–179.7 mbsf), and drilling operation contamination cannot be ruled out. Dispersed mud clasts as large as 2 cm in diameter are common in the Facies II-2 sand bed in interval 188-1167A-37X-1, 0 cm, through 37X-3, 89 cm (322.5–326.39 mbsf) (Fig. F11). The sand

F6. Silty sand with dispersed clasts typical of Facies II-1, p. 44.

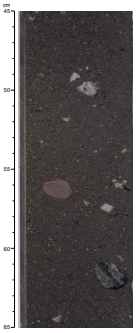

F7. Lonestone lithologies and distribution in Hole 1167A, p. 45.

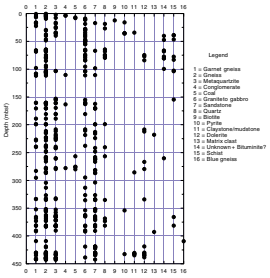

F8. Distribution and frequency of sandstone vs. granite/igneous lonestones in Hole 1167A, p. 46.

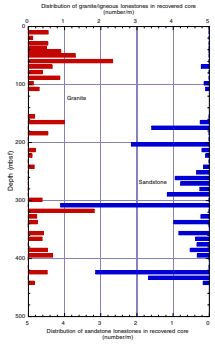

F9. Gravel bed from Facies II-1, p. 47.

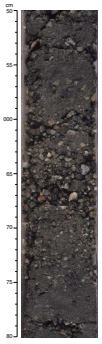

in interval 188-1167A-39X-1, 0 cm, through 39X-2, 70 cm, of Facies II-2 (341.7–343.9 mbsf) displays slight normal grading from very coarse to coarse sand. Rock granules are rare in this sand interval.

Facies II-3

Facies II-3 consists of decimeter-scale beds of dark gray (5Y 4/1 and N4) clay and clay with thin (<1 mm) silt laminae and burrowed intervals (Figs. F3, F12). In intervals 188-1167A-25X-1, 88–98 cm (208.88–208.98 mbsf), and 25X-1, 104–136 cm (209.04–209.36 mbsf), the Facies II-3 clay intervals contain rare sand grains and are barren of lonestones. At the top of interval 188-1167A-5H-3, 10–32 cm (36.8–37.02 mbsf), cross-stratification within the clay laminae is observed along with a few discontinuous silt laminae at interval 188-1167A-5H-3, 14–21 cm. There are sharp contacts at the top and the base of this facies (Fig. F13). Within interval 188-1167A-25X-6, 129 cm, through 25X-CC, 21 cm (216.79–217.64 mbsf), there are numerous 1- to 2-mm-thick discontinuous silt laminae. Some silt laminae are subparallel or convergent and indicate cross-bedding (Fig. F12).

Facies II-4

Facies II-4 consists of centimeter- to decimeter-scale beds of greenish gray (5GY 4/1) to dark gray (N4) sandy clay with dispersed rock granules. This facies is present in intervals 188-1167A-5H-3, 32–40 cm (37.02–37.1 mbsf); 25X-1, 64–88 cm (208.64–208.88 mbsf); 25X-1, 136–145 cm (209.36–209.45 mbsf); and 25X-CC, 21–25 cm (217.64–217.68 mbsf) (Fig. F3). The upper contact of Facies II-4 is sharp, and the lower contact is gradational to sharp (Fig. F14). In contrast to the other facies, the biogenic content of Facies II-4 is relatively high. Foraminifers are abundant and nannofossils are common.

In Cores 188-1167A-5H and 25X, a succession of alternating coarse- and fine-grained facies is present. In this succession, Facies II-1 dark gray silty sands and clayey sands have sharp lower contacts with the planar, cross-laminated dark gray clays of Facies II-3. At the base of Facies II-3, there is a sharp contact with decimeter-thick greenish gray clays (Facies II-4) (Figs. F3, F15). The succession ends with sharp contacts between Facies II-1 and II-4 sediments. This succession is present in four intervals: 188-1167A-5H-3, 10–40 cm; 25X-1, 64–98 cm, and 104–145 cm; 25X-6, 129 cm; and 25X-CC, 25 cm. In one interval (188-1167A-25X-1, 64–98 cm), a bed of Facies II-4 sediment also overlies Facies II-3 (Fig. F3).

Interpretation

Facies II-1 and II-2 record deposition by mass-transport processes, probably massive debris flows. Debris-flow deposits are evidenced by poor sorting, abundant matrix-supported clasts and mud clasts, a general absence of visible grading, and a lack of pelagic biogenic components. The debris flows may represent deposition during glacial periods when ice extended to the shelf break and could deliver large volumes of sediment to the upper continental slope. At present, the thickness and frequency of individual flows are uncertain. The only apparent breaks in debris-flow deposits are in Cores 188-1167A-5H and 25X, where Facies II-3 and II-4 are found (Fig. F3); however, contacts between additional individual flows may not be megascopically recognizable.

F10. Example of dark gray and dark reddish gray color banding, p. 48.

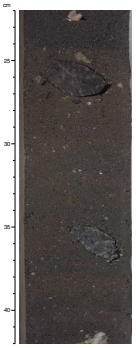

F11. Facies II-2 coarse sand with dispersed mud clasts, p. 49.

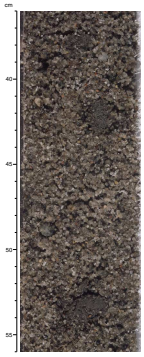

F12. Facies II-3 clay with silt laminae, p. 50.

F13. Sharp contacts at the top of Facies II-3 clay, p. 51.

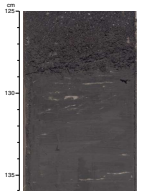

The thin intervals of fine-grained sediments in Facies II-3 and II-4 indicate a change in the mode of sedimentation and a break in debris-flow deposition. Clays with silt laminae are similar in appearance and composition to the sediments of lithostratigraphic Unit III at Site 1165 (see "Lithostratigraphy," p. 7), which are interpreted as muddy contourites. Therefore, Facies II-3 may record short intervals when contour currents were active on the fan. The nature of the silt laminae and bioturbation within Facies II-3 would argue against deposition by turbidity currents. The abundance of pelagic foraminifers in Facies II-4 suggests pelagic deposition, whereas the dispersed sand and granules suggest deposition of IRD. This facies thus appears to represent short intervals, possibly interglacials, when mass transport and contour-current deposition were interrupted and pelagic deposition was dominant.

Lonestones

Lonestones from Site 1167 (>1 cm largest visible diameter on the cut face of each core) were cataloged and assigned to one of 16 lithologic varieties (Table T3). Figure F4 illustrates the downhole variation in average size of the lonestone clasts. In general, size variations seem to be random with only a minor increase downhole from 0 to ~200 mbsf. The number of lonestones per meter of core remains fairly consistent from 0 to ~160 mbsf, below which there is a series of downward increases in lonestone concentration from 160 to 210, 300 to 320, and 410 to 420 mbsf. A slight overall downhole increase in lonestones per meter is also noted below 200 mbsf (Fig. F4).

The distribution of the 16 lithologies was plotted against depth to examine possible changes in provenance of the penetrated sediments (Fig. F7). In general, the vertical distribution of lithology groups appears to be random; however, closer inspection of items 6 (granite group) and 7 (sandstone group) suggests that this is not the case. These two lithology groups, granite (including diorites and gabbros for the purposes of binning) and sandstone, show systematic changes in distribution downhole (Fig. F8). The granite group is most abundant in the upper part of the hole and decreases downhole between 0 and ~200 mbsf. Below this point, the abundance of granite group clasts is significantly reduced. In contrast, the sandstone group clasts demonstrate the opposite trend: few or no sandstone clasts appear down to ~180 mbsf, below which the number of sandstone clasts per meter of core increases significantly (Fig. F7). This type of distribution (i.e., an inverse relationship between clast groups) suggests the possibility that two different source areas delivered material to Site 1167 and that one source area (granite) gave way to the other (sandstone). In addition to the variation in sandstone and granite distributions, a greater abundance of schist clasts (item 15 in Fig. F7) and dark clasts of unknown composition (item 14 in Fig. F7) above 180 mbsf may also indicate a change in the predominance of source areas.

Blue gneiss with cordierite is present in Section 188-1167A-46X-CC, 25 cm. Blue gneiss with cordierite is a conspicuous lithology in the Larseman Hills region of Princess Elizabeth Land (Tingey, 1991); therefore, the blue gneiss in Core 188-1167A-46X is possible evidence that this region was a source area for the recovered sediments at Site 1167.

A possible bituminite clast is present in Section 188-1167A-30X-3, 105 cm (~260 mbsf) (Fig. F7). This 2-cm elongate clast is black, rounded, striated, and malleable and exhibits a low specific gravity. Possible sources of this clast are unclear.

F14. Sharp contact at the top and gradational contact at the base of Facies II-4 clay, p. 52.

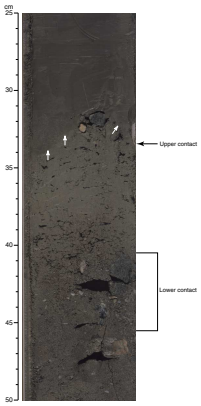

F15. Typical succession of coarse- and fine-grained facies, p. 53.

T3. List of lonestone and dispersed granules, p. 87.

Smear Slides

The mineralogy of smear slides reveals no trend at this site. Similarly, the grain-size distribution within the mud-sized sediments and the matrix of the coarser grained varieties estimated using smear slides presents no systematic trend (Fig. F16). Several peaks in the abundance of clay-sized and silt-sized components reflect minor changes in sediment type as described in the body of the report.

X-Ray Diffraction Mineralogy

At Site 1167, 44 samples were analyzed for bulk mineralogy and 13 samples were analyzed for clay minerals. XRD bulk mineralogy data show that the sediments are primarily composed of quartz, plagioclase, K-feldspar, and a mixture of clay minerals (Fig. F4). In Sample 188-1167A-9X-1, 25–26 cm, a minor amount of hornblende and calcite is present. Total clay content remains relatively constant throughout the hole. Total quartz content in the upper 208 mbsf is slightly less than in deeper portions of the hole, whereas from 208 mbsf downhole, the relative abundance of plagioclase decreases and the abundance of K-feldspar stays constant. Poor sorting and differences in abundance of very coarse material in sediments may cause the slight irregular variability in quartz content downhole.

Thirteen samples were chosen for an overview of clay mineralogy changes in Units I and II. These samples were taken from the clay of Unit I, clayey silty sands and diamictons of Unit II, and three thin clay beds in intervals 188-1167A-5H-3, 12–13 cm; 25X-1, 126–127 cm; and 25X-7, 17–18 cm. In Unit I, an olive-gray clay (4.93 mbsf; Sample 188-1167A-1H-4, 43–44 cm) contains kaolinite, smectite, and illite, with some clay-sized quartz, plagioclase, and K-feldspar (Fig. F17). A sample from the underlying dark gray poorly sorted sandy clay with some dispersed granules of Facies II-1 (36.82 mbsf; Sample 188-1167A-5H-3, 12–13 cm) mainly consists of illite, kaolinite, and minor chlorite (Fig. F17). Smectite is absent, and there is more illite and less kaolinite than found in the clays of Unit I. The gray to greenish gray clay bed of Facies II-4 (209.26 mbsf; Sample 188-1167A-25X-1, 126–127 cm) exhibits a very similar clay mineral distribution to the sample at the top of the hole in Unit I; however, a Facies II-3 sample of the dark clay with few silt laminae (217.2 mbsf; Sample 188-1167A-25X-7, 17–18 cm) shows a distinctively different clay-mineral assemblage including kaolinite, less illite, and no smectite (Fig. F18).

The Facies II-1 color-banded reddish gray poorly sorted clayey sand with dispersed clasts (64.61 mbsf; Sample 188-1167A-10R-1, 31–32 cm) contains kaolinite, illite, and smectite (Fig. F19). The most typical lithology of Facies II-1 (Samples 188-1167A-14X-1, 39–40 cm; 27X-1, 39–40 cm; 33X-2, 43–44 cm; 38X-1, 58–59 cm; 43X-2, 104–105 cm; 47X-1, 55–56 cm; and 48X-2, 35–38 cm) demonstrates these same clay minerals; however, the ratio of smectite to illite varies slightly and compared to the abundance of kaolinite remains fairly constant throughout the section (Fig. F19). Below 382 mbsf, the abundance of smectite is higher compared to upper portions of the sediments. The poorly sorted sandy silt to silty sand of Facies II-1 (429.13 mbsf; Sample 188-1167A-48X-1, 83–84 cm) contains predominantly kaolinite, illite, smectite, and also a minor amount of chlorite (Fig. F19).

The presence of smectite in clays of Facies II-4 at two different horizons (4.93 and 209.26 mbsf), coupled with the presence of biogenic

F16. Percentages of sand, silt, and clay from smear slides, p. 54.

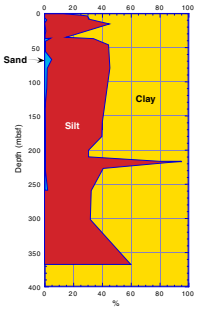

F17. X-ray diffractograms of clay-sized fractions of sediment from Cores 188-1167A-1H and 5X, p. 55.

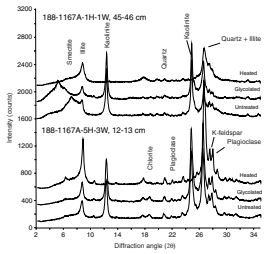

F18. X-ray diffractograms of clay-sized fractions of sediment from Core 188-1167A-25X, p. 56.

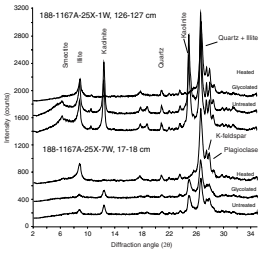

F19. X-ray diffractograms of clay-sized fractions of sediment from Cores 188-1167A-10X, 14X, and 48X, p. 57.

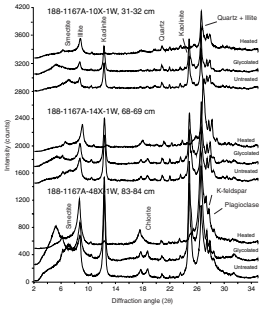

components, suggests more hemipelagic sedimentation in these intervals. The clay-rich intervals with silty laminae of Facies II-3 (36.82 and 217.2 mbsf) are dominated by illite and resemble those overlying and underlying poorly sorted sandy silts to silty sands of Facies II-1, which suggests a similar sediment source for both these clays and the debris flows. Slight changes in illite/smectite ratios may relate to variations in sediment sources or may result from different glacial and gravitational flow processes (cf. Ehrmann and Fütterer, 1994). Thus, changes in the clay-mineral assemblages in trough-mouth fan deposits may provide indirect information about periods of glacial advances to the shelf edge during late Pliocene–Pleistocene time; however, smectite dominance in the hole below 382 mbsf is probably more directly linked to sediment-source characteristics, as is the slightly higher total quartz content below 208 mbsf. Overall, the presence of kaolinite relates only to the source area characteristics, where chemically weathered basement and sedimentary rocks were common. During the Pliocene–Pleistocene, less weathered sources were likely available, and these provided the various amounts of illite and smectite observed in the sediments.

Environmental Interpretation

Subtle changes in composition downcore at Site 1167 may suggest important implications for the glacial history in the Prydz Bay region. Unit I, the thin Holocene to upper Pleistocene hemipelagite interval, records the most recent deposition on the slope and represents interglacial conditions when fine particles and biogenic material settled out of the water column, and IRD was supplied by icebergs.

Unit II records a thick succession of debris flows on the slope. The relatively thin intervals of Facies II-3 and II-4 clays represent relatively short periods when conditions changed and an alternate form of sedimentation (i.e., current-driven or hemipelagic) was preserved. It is possible that these intervals represent changes from glacial to interglacial conditions or minor fluctuations during a glacial period.

Changes in sediment composition can be identified on different scales at Site 1167. Repetitive changes in sediment composition may be caused by short-term climate cyclicity, perhaps advances and retreats of the grounding line without major shifts in glacial flow patterns. Slight changes in illite/smectite ratios may be related to these grounding-line processes; however, in sediment from the lower part of the hole, smectite dominance is probably related more to source-area characteristics than to grounding-line processes. Large-scale shifts in sediment composition may be related to major rearrangements within the Lambert Glacier–Amery Ice shelf drainage system.

Several lithologic downhole parameters change at 200–210 mbsf. Lonestone data show a significant upward change from sandstone to granite stones at ~200 mbsf, which may suggest a shift in sediment provenance. XRD bulk mineralogy shows a higher abundance of plagioclase above 210 mbsf than below, whereas quartz is more abundant below 210 mbsf than above. Clay mineralogy data shows higher kaolinite/illite ratios for the lower part of the hole than found above 210 mbsf. Additionally, magnetic susceptibility (see **"Paleomagnetism,"** p. 19), grain density and porosity (see **"Physical Properties,"** p. 25), natural gamma-ray data (see **"Downhole Measurements,"** p. 31), and data from foraminifer residues (see **"Appendix,"** p. 37) all exhibit distinctive changes near 210 mbsf.

BIOSTRATIGRAPHY AND SEDIMENTATION RATES

Introduction

Hole 1167A was drilled on the Prydz Bay Trough Mouth Fan in order to penetrate a late Miocene and younger sequence and elucidate the history of the advance and retreat of the ice sheet to and from the Antarctic continental shelf edge.

Foraminifers are the only consistently present microfossil in Hole 1167A. The dominance of *Neogloboquadrina pachyderma* (Ehrenberg) suggests that the section is late Miocene or younger in age (*N. pachyderma* Zone or AN7 of Berggren et al., 1995). The foraminifers present in the diamictons indicate that outer continental shelf faunas are being recycled. Clay-rich horizons contain in situ mid-bathyal faunas.

Diatoms indicate that Core 188-1167A-1H is <0.66 Ma (*Thalassiosira lentiginosa* Zone) in age. Calcareous nannofossils in Sample 188-1167A-5H-3, 35–36 cm, are likely to be mid-Pleistocene in age (Zones CN12–14a of Samtleben, 1980), and those in Sample 188-1167A-25X-CC, 22–23 cm, are early to mid-Pleistocene in age (Zone CN13b).

Biostratigraphic results from Hole 1167A are summarized in Figure F20.

F20. Core recovery, lithostratigraphic units, magnetostratigraphy, and biostratigraphic zones for Hole 1167A, p. 58.

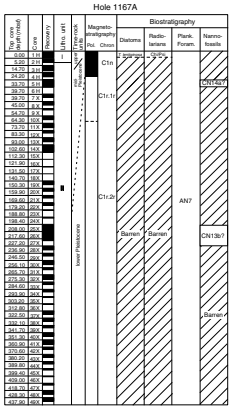

Foraminifers

Introduction

N. pachyderma (Ehrenberg) dominates all foraminferal assemblages recovered from Hole 1167A. Above 217 mbsf, all samples other than Sample 188-1167A-1H-CC contain some foraminifers; below Sample 188-1167A-25X-CC, a high proportion of samples are barren.

Two distinct associations of foraminifers are present in Hole 1167A. The most common association is with very coarse poorly sorted sandstone dominated by angular terrigenous debris. Samples from these intervals yield few foraminifers, but over many samples a diverse array emerges. These faunas are dominated by *N. pachyderma* (Ehrenberg) with one or two subordinate planktonic species. Higher in the hole, benthics comprise a few percent of each sample. Benthic shelf calcareous species, especially cassidulinids but with a few buliminid species, indicate an infaunal element. Sediments barren of foraminifers could represent times of reduced habitat availability and lower sea level (glacial maxima), and sections with greater foraminiferal content could indicate greater habitat availability during times of low ice cover and higher sea level (glacial minima). Glacial-interglacial variations in the carbonate compensation depth (CCD) may have affected carbonate preservation at Site 1167.

The second association occurs in the few gray clay samples. This lithology yields abundant (99%) planktonic foraminifers dominated by *N. pachyderma*. Benthic forms are rare but more diverse and typical of the bathyal or slope environment. The presence of echinoid spines suggests that the seafloor supported a more diverse fauna than in other samples.

The two associations represent fundamentally different environments of deposition consistent with the hypothesis of (1) periodic influx of shelf sediment and (2) pelagic conditions when the shelf

sediment influx is reduced. In the former association, benthic species represent outer continental shelf conditions (their source, but redeposited over the shelf edge). In the second case, the calcareous biogenic component of the sediment is higher and represents an in situ mid- to upper bathyal fauna. It is possible that the variation in numbers of planktonic species is a proxy for the difference in rate of influx of sediment. This assumes that the rate of production of planktonic species is roughly constant.

Other than the transport of continental shelf faunas to the slope, there is little evidence of reworking. A little glauconite is present in Samples 188-1167A-5H-CC, 12X-CC, and 27X-CC. Sample 188-1167A-1H-CC was notably different, being reddish in color and yielding sand with a high content of iron oxide–coated grains. It is the only sample examined above Core 188-1167A-25X that is barren of foraminifers.

Samples 188-1167A-5H-3, 34–35 cm, and 25X-CC, 22–23 cm, contain abundant and well-preserved foraminifers; these assemblages are dominantly planktonic (to ~6000 per sample) and contain a diverse, mid-bathyal benthic fauna that is very different from that in other samples from Hole 1167A.

The modern CCD at the continental shelf edge of Prydz Bay is at ~1500 m (Quilty, 1985); thus, dissolution was expected to be pervasive at Site 1167. However, dissolution effects are not obvious until Sample 188-1167A-25X-CC, 22–23 cm. Here, both foraminifers and ostracods show evidence of dissolution even though abundance is still relatively high. Ostracods are represented by a few valve rinds and foraminifers by partial dissolution of layers of the thick tests of *N. pachyderma*. In Sample 188-1167A-40X-CC, foraminifers are absent but there is a single pyrite pseudomorph after a species of *Globigerina* to indicate that some planktonic specimens were present but have subsequently been dissolved. Sample 188-1167A-25X-CC yielded no foraminifers but contains a few pyrite pseudomorphs that may represent infilling of benthic tests. Calcite dissolution may be diagenetic or CCD related.

Using Table **T4** for guidance, three intervals can be roughly delineated on the basis of foraminiferal abundance. Samples 188-1167A-2H-CC through 19X-CC yielded faunas that are poor to good, with the exception of the excellent preservation of a bathyal fauna in Sample 188-1167A-5H-3, 34–36 cm. Samples 188-1167A-20X-CC through 31X-CC are barren or contain very poor faunas similar to the mid-bathyal fauna of Sample 188-1167A-25X-CC, 22–23 cm. The interval 188-1167A-32X-CC through 49X-CC contains no excellent samples but provided enough specimens for Sr dating.

T4. Abundance of foraminifers in samples, Hole 1167A, p. 88.

Planktonic Foraminifers

N. pachyderma is the dominant planktonic species throughout Hole 1167A down to Sample 188-1167A-48X-CC, consistent with an age of late Miocene or younger (*N. pachyderma* Zone or AN7 of Berggren, 1992, and Berggren et al., 1995). The Pliocene–lowermost Pleistocene interval rich in other species such as *Globorotalia puncticulata* (Deshayes) recognized in Hole 1165B could not be identified in Hole 1167A. This may suggest that drilling in Hole 1167A did not reach this stratigraphic level. Although not recorded by Berggren (1992) as a zonal fauna, it is present in Sites 747 (Ocean Drilling Program [ODP] Leg 120) and 1165 and would be expected at Site 1167.

Samples 188-1167A-5H-3, 34–36 cm, and 25X-CC, 22–23 cm, are particularly noteworthy. In contrast to other samples in this interval, these

samples yielded rich faunas dominated by *N. pachyderma* but with one or two other planktonic species well represented (with a total planktonic component well over 98% of the total foraminifer fauna). Samples have been set aside for Sr dating and for detailed taxonomic study of a *Globorotalia* (*Tenuitella*) sp. that is common in the fauna. It also has a small benthic component of environmental significance. These assemblages are characteristic of the slope faunas.

Specimens of *N. pachyderma* in Sample 188-1167A-37X-CC are unusual in being very small and compact, in contrast to samples above this level, which are large, less compact, and generally more abundant. *N. pachyderma* is, as expected, almost 100% sinistrally coiled, although a few dextral specimens were seen (e.g., in Sample 188-1167A-19X-CC).

Eight samples with adequate numbers of *N. pachyderma* were set aside for postcruise Sr dating. It is expected that further samples will be obtainable when all samples have been processed. There is ample material in most samples for oxygen/carbon isotope studies.

Benthic Foraminifers

The benthic component of Hole 1167A samples is dominated by species of *Globocassidulina* and common buliminids and is considered to be an allochthonous fauna. This is the only Leg 188 section to contain evidence of a significant infauna, perhaps reflecting high nutrient conditions near a zone of upwelling. Upwelling here may simply be a function of the flow of Circumpolar Deep Water into Prydz Bay from the deeper ocean. These faunas probably represent outer shelf faunas that have been moved downslope.

Globocassidulina biora (Crespin) is a very characteristic Antarctic species; its first occurrence (FO) may, when documented fully, provide a useful chronostratigraphic marker. From preliminary observations, the FO of this taxon is noted in Sample 188-1167A-19X-CC.

Samples 188-1167A-5H-3, 34–36 cm, and 25X-CC, 22–23 cm, contain faunas that, although constituting <1% of the total foraminiferal fauna, yield forms not seen elsewhere during Leg 188. This assemblage is not a shelf fauna and includes *Planulina wuellerstorfi* (Schwager). The contrast between this fauna and the globocassidulinid-dominated shelf faunas is very marked and suggests that this fauna is in situ and not a product of transport from shallower depths.

Sample 188-1167A-8H-CC provided a well-preserved fauna with evidence (ostracods and echinoid spines) of a diverse fauna on the seafloor.

Calcareous Nannofossils

Only a few samples examined from Cores 188-1167A-1H through 49X contained calcareous nannofossils. Sample 188-1167A-5H-3, 35–36 cm, was taken from a fine-grained muddy interval at the base of a sandy diamictite. The sample contains few moderately to well-preserved nannofossils, including *Gephyrocapsa* sp. morphotypes with central bars not preserved. One specimen of *Gephyrocapsa ericsonii* was noted with a bar intact, and a few small *Pseudoemiliania lacunosa* were noted. The assemblage also included rare *Calcidiscus leptoporus* and few fragments of the calcareous dinocyst, *Thoracosphaera*. A reworked specimen of the Late Cretaceous species *Gartnerago obliquum* was observed, consistent with the suggestion by Quilty et al. (1999) of the presence of uppermost Cretaceous marine sediments in the region.

The presence of *P. lacunosa* along with *Gephyrocapsa* places this sample in nannofossil Zones CN12–CN14a of late Pliocene to mid-Pleistocene age (Fig. F20); however, the small *G. ericsonii* morphotypes probably indicate a younger mid-Pleistocene age (Zone 14a?) (Samtleben, 1980).

Within Core 188-1167A-25X, several centimeter-scale green to brown claystone intervals were sampled and contained rare to few moderately to well-preserved calcareous nannofossils. Notably, Sample 188-1167A-25X-CC, 22–23 cm, contained *P. lacunosa, Gephyrocapsa* spp., *C. leptoporus, Coccolithus pelagicus,* and rare large forms (5.5 µm) of *Gephyrocapsa caribbeanica*. A similar assemblage of rare nannofossils, without the large *Gephyrocapsa,* was also noted in Sample 188-1167A-27X-CC. The presence of *G. caribbeanica* and *P. lacunosa* indicates an early to mid-Pleistocene age (Zone CN13b) for this interval.

Discussion

Modern calcareous nannoplankton do not thrive in surface waters south of the Antarctic Divergence (>62°S) (Findlay, 1998), and few occurrences of nannofossils have been reported from Quaternary sediments of the Antarctic region. Previous drilling on the Kerguelen Plateau has revealed depauperate Pleistocene assemblages of similar composition to those noted here (Wei and Thierstein, 1991; Wei and Wise, 1992). Comparable Quaternary nannofossil assemblages were also noted in sediments of the Antarctic Peninsula Pacific margin (Barker, Camerlenghi, Acton, et al., 1999).

Particularly interesting at Site 1167 is the presence of the calcareous dinoflagellate *Thoracosphaera,* which was not previously noted in Quaternary Antarctic sediments until Villa and Wise (1998) reported rare specimens in shelf sediments of this age from the Ross Sea region (Cape Roberts Project). Because no other nannofossils were noted in their assemblages and age control is limited at both localities, it is difficult to determine whether the *Thoracosphaera*-bearing sediments of Site 1167 are correlative. Regardless, Villa and Wise (1998) point out that the presence of *Thoracosphaera* may indicate warmer conditions and/or result from its ability to develop cysts in response to rapidly changing conditions, as is noted for the Quaternary. The presence of calcareous nannofossils along with *Thoracosphaera* at Site 1167 likely suggests warmer sea-surface temperatures at this locality at various times throughout the Quaternary.

Diatoms

Diatoms are absent from the entire section of Hole 1167A, except for limited intervals within Core 188-1167A-1H and Sample 188-1167A-36X-CC (313.30 mbsf). Between the top of Core 188-1167A-1H (Sample 188-1167A-1H-1, 1–2 cm; 0.01 mbsf) and its base (Sample 188-1167A-1H-CC; 5.02 mbsf), only extant diatoms are present. This interval is placed within the *T. lentiginosa* Zone based on the absence of *Actinocyclus ingens* (last occurrence [LO] = 0.66 Ma). Diatom abundance and preservation decrease down through Core 188-1167A-1H, and they are entirely absent in Sample 188-1167A-2H-CC. A broken specimen of *A. ingens* was observed in Sample 188-1167A-1H-CC and is interpreted as reworked.

At depths below 5.02 mbsf, only one diatom specimen was observed. A slightly recrystallized specimen of *Denticulopsis dimorpha* (FO = 12.2

Ma; last common occurrence = 10.7 Ma) was noted in Sample 188-1167A-36X-CC (313.30 mbsf) and is interpreted to be reworked. Calcareous nannofossil and foraminifer biostratigraphy indicate a Pliocene–Pleistocene age for this interval.

The absence of diatoms through almost all of Hole 1167A is noteworthy, given that there are well-preserved and abundant in situ planktonic foraminiferal assemblages in several intervals. Fine-grained intervals in Core 188-1167A-25X, for example, were sampled thoroughly, and no siliceous microfossils were observed (whole frustules, fragments, or otherwise). The presence of common planktonic foraminifers and rare nannofossils in these intervals would suggest, however, that phytoplankton primary production occurred. The lack of diatoms from the foraminifer-rich sediment samples could result from numerous processes, such as (1) lightly silicified biocoenosis that was not preserved in the sediments because of dissolution in the water column and/or at the sediment/water interface or (2) the dominance of nonsiliceous phytoplankton communities that may have outcompeted, or filled a niche unfavorable to, the diatoms. Water-current winnowing is not considered a factor because of the presence of clay-dominated sediments and rare calcareous nannofossils, which are smaller than most diatoms and more susceptible to winnowing.

Hole 1167A is dominated by coarse-sediment lithofacies. Massively bedded sands and sandy diamicts present through lithostratigraphic Unit II are interpreted as representing sediment-gravity flows (see **"Lithostratigraphy,"** p. 7). The absence of diatoms in these intervals is interpreted (at least partially) to result from the dilution of biosiliceous particles by rapid accumulation of terrigenous material.

Radiolarians

A radiolarian fauna was found only in Sample 188-1167A-1H-CC. This sample contains rare, well-preserved radiolarians, but it is not clear whether it should be assigned to the Chi Zone (1.9–0.83 Ma) or the Psi Zone (0.83–0.46 Ma) of Lazarus (1992). *Triceraspyris antarctica* (Haecker) and *Lithelius nautilodes* Popofsky are both present in this sample; these taxa are reported to have a FO at the base of the Chi Zone (Lazarus, 1992). Missing from the sample, however, are *Cycladophora pliocenica* (Hays) Lombari and Lazarus, which has a LO in the middle of the Chi Zone, and *Pterocanium c. trilobum* (Haeckel), which has a LO at the top of the Chi Zone (or bottom of Psi Zone). This suggests that this sample could be assigned to the Psi Zone. Also present in this sample are *Spongotrochus*? *glacialis, Antarctissa denticulata, Antarctissa cyclindrica,* and *Phorticum clevei,* all high-latitude species consistent with assignment to the Chi or Psi Zones.

The radiolarian fauna in Sample 188-1167A-1H-CC on the continental slope are very similar to those noted in Sample 188-1166A-1R-2, 70–72 cm, from the continental shelf site. At both sites, all core-catcher samples were processed and examined for radiolarians, but both sites were nearly barren below these uppermost samples. At Site 1167, it appears that the radiolarians were never deposited, as no traces were found in any samples below the top level; at Site 1166, however, some evidence was seen of rare, poorly preserved radiolarians in Core 188-1166A-13R.

Paleontological Summary of Site 1167

At Hole 1167A, it was expected that siliceous microfossils would provide chronostratigraphic control, but except for Core 188-1167A-1H, where they indicate an age younger than 0.66 Ma, they were essentially absent. Likewise, calcareous nannofossils provided little control other than for Sample 188-1167A-25X-CC, 22–23 cm, which is assigned an age of early to mid-Pleistocene.

Foraminifers are present in most samples, but the low diversity of long-ranging planktonic taxa allows an age assessment only of late Miocene or younger. These foraminifers do, however, provide at least eight samples for postcruise Sr dating. Thus, assessment of ages through the section depends on finalizing paleomagnetic analyses and determination of Sr dates. The value of foraminifers also lies in their use for reconstruction of paleoenvironments. Two faunal associations—mid-bathyal (in situ) and outer continental shelf (recycled)—are recognized, and their distribution is consistent with changes in lithology.

Sedimentation Rates

Chronostratigraphic control in Hole 1167A is of insufficient resolution to warrant construction of an age-depth plot and interpretation of sedimentation rates. Assuming that the section is still Pleistocene at the base of the hole, the sedimentation rate may be as high as ~400 m/m.y. Improved age control may emerge as Sr dating and refined of paleomagnetic data are integrated.

PALEOMAGNETISM

Methods

All the archive-half sections from Hole 1167A (APC and XCB cores) were subjected to pass-through measurements, except for Sections 188-1167A-19X-2; 37X-1, 37X-2, and 37X-3; and 39X-1 and 39X-2 because they were sandy. The natural remanent magnetization (NRM) and remanent magnetization after alternating field (AF) demagnetization were measured routinely using the shipboard pass-through cryogenic magnetometer at 4-cm intervals. Three AF steps at 10, 20, and 30 mT were used for all core sections. A total of 252 discrete samples (standard oriented 8-cm^3 cubes) were collected from the center of the working halves at a frequency of one or two per section. The lithofacies are mainly dominated by coarse-grained sediments with dispersed clasts and minor beds of coarse sands, clays, and sandy clays (see **"Lithostratigraphy,"** p. 7). When possible, samples were selected from fine-grained horizons; however, there was often no alternative but to sample from the sandstone-dominated lithofacies.

A total of 175 samples, after measurement of NRM, were AF demagnetized at successive peak fields of 2, 7, 10, 20, 30, 40, 50, and 60 mT. Thermal demagnetization was conducted on 12 samples collected throughout the core at temperatures of 100°, 200°, 300°, 350°, 400°, 500°, 550°, 600°, 650°, and 700°C. Magnetic susceptibility was measured after each step to monitor for thermal alteration of the magnetic fraction.

Rock magnetic analyses were performed on a set of representative discrete samples after they had been subjected to AF demagnetization

in order to obtain a quantitative estimate of downcore variation in the composition, concentration, and grain size of the magnetic minerals. These variations often provide valuable information about changes in paleoenvironmental conditions in a sedimentary basin and its surrounding regions (Thompson and Olfield, 1986; Verosub and Roberts, 1995). The mineral magnetic analyses followed the same approach that was utilized at Sites 1165 and 1166.

Low-field magnetic susceptibility (k) was routinely measured for each discrete sample (252), and the resultant data were compared with the whole-core susceptibility log (see "Physical Properties," p. 25). The frequency-dependent susceptibility, *fd*(%), was measured on 59 selected samples. Anhysteretic remanent magnetization (ARM) was measured for 172 samples using a 100-mT AF with a superimposed 0.05-mT bias field. On 164 samples, an isothermal remanent magnetization (IRM) was imparted in a direct-current field of 1.3 T. On 57 of these samples, the IRM was then demagnetized by inverting the sample and applying a backfield of 300 mT to determine the S-ratio ($-IRM_{-0.3T}/IRM_{1T}$) (e.g., Verosub and Roberts, 1995). The progressive acquisition of IRM was studied for 12 selected samples.

Time constraints did not allow the investigation of the coercivity of remanence (B_{cr}) or the analysis of thermal demagnetization of the composite IRM (Lowrie, 1990).

Results

Rock Magnetism

Analyses of the rock magnetic properties from Hole 1167A suggest that the core can be divided into two main units (Units I and II) and a number of subunits based on the abundance and grain size of the magnetic minerals in the sedimentary sequence. The main unit boundary coincides with a lithologic change at 217 mbsf (see "Lithostratigraphy," p. 7), whereas the subunit boundaries cannot be directly related to visual lithologic variations in the core.

Magnetic Unit I (0–198.6 mbsf) can be divided into five subunits on the basis of changes in the concentration-dependent parameters (k, IRM intensity, and ARM intensity), which have similar patterns of variation (Fig. F21). Subunit IA (0–4 mbsf) is characterized by relatively low k, ARM, and IRM. At the boundary between Subunits IA and IB (4 mbsf), the magnetic susceptibility jumps from ~23 × 10^{-5} to 126 × 10^{-5} SI then rises in a quasi-linear fashion to ~300 × 10^{-5} SI at 55 mbsf. Between 55.0 and 78.5 mbsf (Subunit IC), the magnetic susceptibility (along with the other magnetic concentration parameters) drops to 128 × 10^{-5} SI, after which it remains approximately constant with a mean value of 160 × 10^{-5} SI. In Subunit ID (78.5–112.2 mbsf), susceptibility rises quasi-linearly to 224 × 10^{-5} SI. Lack of recovery from ~113 to 151.2 mbsf renders susceptibility levels at the base of this unit uncertain. Subunit IE (112.2/151.2–198.6 mbsf) is characterized by a quasi-linear rise in k from 178 × 10^{-5} to 214 × 10^{-5} SI.

Unit II (208.3–447.7 mbsf) can also be divided into subunits on the basis of downcore variations in k, IRM intensity, and ARM intensity. Subunit IIA (208.3–217.5 mbsf), corresponding to decimeter-scale beds of dark gray clay (lithostratigraphic Unit II-3; see "Lithostratigraphy," p. 7), is characterized by relatively constant values of k. The sharp rise in k at the base of this unit is probably related to the presence of igneous clasts in the samples. The susceptibility steadily increases downcore

F21. Downcore variation of concentration-dependent parameters, p. 59.

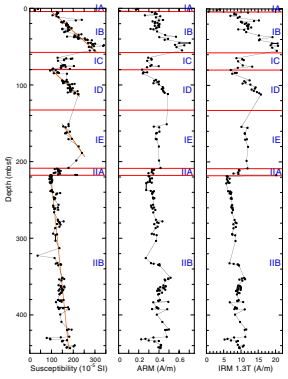

between 217.5 and 447.7 mbsf (Subunit IIB). The sandy horizon at ~325 mbsf is reflected in low susceptibility at this depth.

Preliminary mineral magnetic analyses, based on coercivity spectrum analyses and thermal demagnetization behavior, are consistent with a magnetite-dominated magnetic mineralogy in samples from much of the core. Plots of IRM acquisition display steep slopes at low magnetic inductions, and saturation is achieved between 200 and 300 mT (Fig. F22). S-ratio values (see "Paleomagnetism," p. 16, in the "Explanatory Notes" chapter) are higher than 0.96. In three thin intervals, located at 3.40, 80.0, and 431.0 mbsf, lower S-ratios and resistance to AF demagnetization indicate the prevalence of a high-coercivity mineral (e.g., hematite) as a major magnetic carrier in these horizons.

With the magnetic mineralogy constrained as magnetite, the ARM/IRM ratio can be used as a magnetic grain-size indicator because ARM is more effective in activating finer magnetite grains than IRM. In Figure F23 the ARM/IRM ratio, plotted as a function of depth, shows a considerable variation in grain size between 0 and 15 mbsf. In the interval between 15 and 217 mbsf, the ratio of ARM/IRM is relatively constant, ranging from 0.029 to 0.038 with a mean value of 0.032. Below 217 mbsf, variation of the ARM/IRM ratio is relatively minor, ranging from 0.039 to 0.053 with a mean value of 0.046. The major boundary at 217 mbsf is consistent with a shift from relatively coarse-grained magnetite (above) to relatively fine-grained magnetite (below).

We suggest that the variations in both concentration and grain size reflect changes in sediment provenance. The "sawtooth" concentration fluctuation reflects the varying importance of two or more sediment sources: one or more magnetite rich and one or more magnetite poor. Similarly, we interpret the change in magnetite grain size at 217 mbsf to reflect a change from sources containing relatively fine-grained magnetite to sources containing relatively coarse-grained magnetite. Traces of authigenic pyrite are observed in a few horizons (see "Lithostratigraphy," p. 7); however, diagenetic alteration of the core is not evident from the magnetic signal, and geochemical data are inconsistent with significant diagenesis (see "Inorganic Geochemistry," p. 23).

F22. Plot of IRM acquisition of 10 representative samples, p. 60.

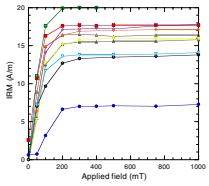

F23. Downcore variation of ARM/IRM, p. 61.

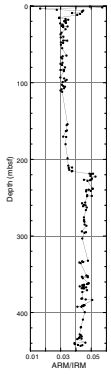

Paleomagnetic Behavior and Magnetostratigraphy

Coarse-grained sediments similar to those common in Hole 1167A have historically been deemed unsuitable for paleomagnetic investigations; however, recent paleomagnetic investigation of glaciogenic sedimentary units from the Victoria Land Basin (Ross Sea) evidence the presence of strong and stable magnetizations even in coarse-grained units (Wilson et al., 1998, in press; Roberts et al., 1998). The stability of these remanences was attributed to the presence of fine magnetic particles within the fine-grained sedimentary matrix of these otherwise coarse-grained units. Hole 1167A paleomagnetic analyses are also hindered by the presence of granules and pebbles dispersed throughout the hole. The presence of such clasts requires that care be taken in the interpretation of paleomagnetic data, especially for data originating from the archive-half sections in which it is not possible to verify the presence of clasts beneath the section surface. This emphasizes the importance of paleomagnetic analysis of discrete samples to verify the reliability of whole-core measurements.

Most of the analyzed cores display a low-coercivity, nearly vertical reversed polarity component that we interpret to represent a drilling-induced overprint (Weeks et al., 1995). In a few horizons, a normal

polarity drilling-induced overprint was also observed. In most cases this component was removed with peak AFs of <10 mT. After the removal of this overprint, a stable characteristic remanence component (ChRM) is evident for a large portion of the analyzed archive halves and discrete samples (Fig. F24). In some cases, this component and the characteristic component of magnetization have completely overlapping coercivity spectra, rendering no demagnetization interval over which only one component is removed (Dunlop, 1979). In these situations it is not possible to isolate the two components.

For 76% of the discrete samples, stable paleomagnetic behavior was evident from the vector component diagram. In most cases the ChRM direction was determined using a best-fit line that was constrained, based on principal component analysis, through the origin of the vector component diagram. In some cases the best-fit line was not constrained through the origin of the plot. The ChRM directions are in excellent agreement with the directions obtained from long-core measurements, with the exception of the reversed polarity direction indicated by a discrete sample at 16.92 mbsf where, conversely, the long-core measurement indicated a normal polarity.

Preliminary magnetostratigraphic interpretation for Hole 1167A is shown in Figure F25. The uppermost 30-m interval of the polarity record is entirely normal. Transitional directions are recorded over a stratigraphic interval of ~4 m, between 30 and 34 mbsf. Considering that the process of polarity reversal occurs over periods of ~5–10 k.y. (Jacobs, 1994), it is possible to estimate a sedimentation rate for this interval (~0.4–0.8 m/k.y.). From 34 mbsf to the bottom of the hole, the polarity is reversed with two short normal polarity intervals at ~355 and at ~380 mbsf.

Biostratigraphic data are restricted to a diatom assemblage constraining the top of Core 188-1167A-1H to <0.66 Ma and two nannofossil assemblages: a Zone CN14a assemblage at 37.05 mbsf and a Zone CN13b assemblage between ~218 and 228 mbsf, with ages of 0.4–0.9 Ma and 0.9–2.0 Ma, respectively (see **"Biostratigraphy and Sedimentation Rates,"** p. 14). Constrained by these nannofossil datums, the upper normal polarity magnetozone is correlated with the Brunhes (C1n) Chron and the long reversed interval, between 34.0 mbsf and the bottom of the hole (447.5 mbsf), is correlated with the C1r.1r and C1r.2r Chrons. We suggest that the Jaramillo Subchron (C1r.1n) is missing possibly because of unconformities in the record (e.g., at 55 m) that are suggested from sharp changes of the concentration-dependent parameters (Fig. F21).

Eight samples with adequate numbers of the planktonic species *N. pachyderma* have been collected for Sr dating (see **"Biostratigraphy and Sedimentation Rates,"** p. 14). These samples, close to the interpreted Brunhes/Matuyama boundary and to the two thin normal polarity intervals, will further constrain this preliminary magnetostratigraphic interpretation.

Notably, the inclinations downcore are consistently shallower than expected for the site latitude (66°S). We suggest that observed shallow inclinations are due to sediment compaction immediately after deposition (e.g., Anson and Kodama, 1987; Arason and Levi, 1990).

F24. Vector component diagrams of demagnetization (AF) behavior of four samples from Hole 1167A, p. 62.

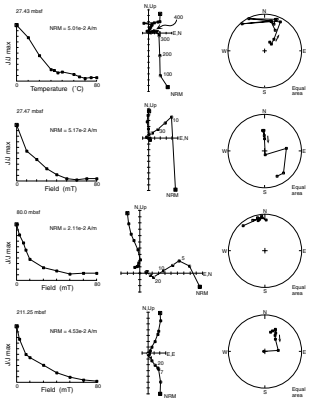

F25. Magnetostratigraphic record from Hole 1167A, p. 64.

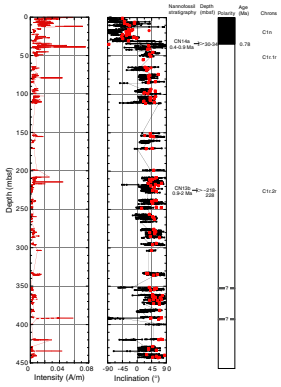

INORGANIC GEOCHEMISTRY

Thirty-seven interstitial water samples were collected from Hole 1167A and analyzed according to the procedures outlined in "Inorganic Geochemistry," p. 19, in the "Explanatory Notes" chapter (Table T5). The sampling protocol required one 5- to 15-cm-long whole-round interval from each section of core to 60 mbsf, one whole-round interval per core to 100 mbsf, and one whole-round interval every two to three cores to the bottom of the hole. The shallowest sample was taken from 1.45 mbsf and the deepest from 432.65 mbsf, ensuring coverage of diagenetic processes throughout the complete cored section.

T5. Interstitial water chemistry from shipboard measurements, p. 89.

Salinity and Chlorinity

An ~2% increase occurs in both salinity and chlorinity near the seafloor between 10 and 50 mbsf (Fig. F26). Salinity increases downhole from 35.0 at the seafloor to 35.5 at ~22 mbsf and remains at 35.5 to 50 mbsf. Chlorinity increases from 560 to 572 mM over the same interval. It is likely that the interstitial waters above ~50 mbsf represent high-salinity last-glacial seawater, although in situ hydration of clay minerals cannot be discounted with the current data. Both salinity and chlorinity decrease in parallel from 100 to 325 mbsf (34.5–34.0 and 560–540 mM, respectively). Chlorinity then increases to 433 mbsf (541–552 mM), whereas salinity remains constant.

F26. Interstitial water chemistry profiles vs. depth, p. 65.

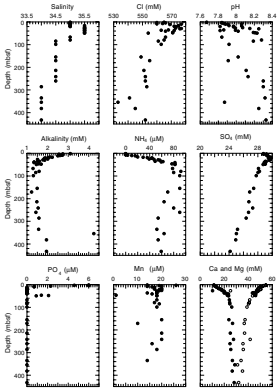

Sulfate, Ammonium, Alkalinity, Phosphate, and Manganese

Sulfate parallels salinity and chlorinity profiles between 10 and 50 mbsf, increasing from 28.8 mM near the seafloor to 29.8 mM at ~19 mbsf. From 20 to 433 mbsf, sulfate decreases in a stepped profile to 24 mM at 433 mbsf. As sulfate is not exhausted as an organic matter oxidant, CO_2 reduction does not occur at Site 1167 (cf. Site 1165).

Ammonium increases linearly from near-surface values of 0 µM to a maximum of ~80–90 µM between 60 and 100 mbsf. Below 100 mbsf, ammonium decreases steadily to ~60 µM at 433 mbsf. These low ammonium concentrations (an order of magnitude less than ammonium at Site 1165) reflect limited sulfate reduction. Two additional products of sulfate reduction, alkalinity and phosphate, behave nonconservatively. Alkalinity decreases linearly from seafloor values of ~3 mM to 1.3 mM at ~40 mbsf and remains relatively constant from 100 mbsf to the base of the hole. Similarities in the downhole profiles of alkalinity, potassium, lithium, and magnesium and the inverse trend shown by calcium (see "Magnesium, Calcium, Strontium, and Sodium," p. 24) suggest that alkalinity is responding to an unidentified diagenetic silicate mineral reaction. Seafloor concentrations of phosphate (6.0 µM) rapidly decrease to zero at 10 mbsf. Aside from a small excursion to 2.1 µM between 46 and 49 mbsf, phosphate concentrations remain below the detection limit to the base of the core.

Dissolved manganese decreases rapidly from 25 to 15 µM in the first 10 m of the core. Below 10 mbsf, manganese concentrations increase to 20 µM at 22 mbsf and then decrease to ~17 µM at ~30 mbsf, where they remain more or less constant to the base of the core. High manganese concentrations between 20 and 30 mbsf are the product of the reduction of manganese oxides during the oxidation of OC. Comparison of

the phosphate and manganese profiles (Fig. F26) suggests that phosphate may be adsorbed onto the surface of manganese (or iron) hydroxides.

Magnesium, Calcium, Strontium, and Sodium

Dissolved magnesium concentrations decrease rapidly from 54.5 mM at the seafloor to ~40 mM at 50 mbsf. Between 50 and 433 mbsf, magnesium decreases from 40 to 30 mM, with a small change in gradient at ~100 mbsf. Dissolved calcium concentrations show an inverse trend, increasing rapidly from 11 mM at the seafloor to 24 mM at 50 mbsf. Between 50 and 433 mbsf, calcium concentrations increase from 24 to 28 mM. A small change in gradient is again apparent at ~100 mbsf. The strong negative linear correlation ($\Delta Ca^{2+}/\Delta Mg^{2+} = -1$) observed throughout the core is likely due to silicate reconstitution reactions. The general downhole decrease in sodium concentration may reflect the albitization of plagioclase, with the associated release of calcium to the interstitial waters. Clay mineral reactions (e.g., smectite formation) may partially account for the magnesium decrease. Dissolved strontium concentrations increase downhole from ~100 µM at the seafloor to ~200 µM at 335 mbsf (Fig. F26). The strontium profile is consistent with a minor downhole increase in calcium carbonate reconstitution reactions.

Potassium, Lithium, and Silica

Dissolved potassium decreases from ~12 to ~2 mM between the seafloor and 100 mbsf (Fig. F26), with a marked change in slope at ~50 mbsf. Below 100 mbsf, potassium concentrations remain at ~2 mM to 433 mbsf. Lithium decreases from ~30 µM at the seafloor to ~5 µM at ~40 mbsf. Below ~40 mbsf, lithium concentrations increase nonlinearly to ~10 µM at 335 mbsf. The profiles suggest that both potassium and lithium are participating in the same diagenetic reactions as calcium and magnesium. The overall low lithium concentrations argue against the alteration of volcanic material as a major contributing factor.

Dissolved silica concentrations are high from the seafloor to 5 mbsf (568–673 µM) because of the dissolution of siliceous microplankton in the near-surface sediments (see "Biostratigraphy and Sedimentation Rates," p. 14). Immediately below this zone, silica values return to ~200 µM, approximating the concentrations found in modern undersaturated bottom seawater. Silica concentrations increase gradually downhole to ~300 µM at 433 mbsf.

ORGANIC GEOCHEMISTRY

Shipboard organic geochemical studies of cores from Site 1167 included monitoring of hydrocarbon gases, carbonate and OC, total sulfur (TS) and total nitrogen (TN) content, and Rock-Eval pyrolysis characterization of organic matter. Procedures are summarized in "Organic Geochemistry," p. 20 in the "Explanatory Notes" chapter.

Hydrocarbon Gases

Cores recovered from Site 1167 were monitored for hydrocarbon gases measured by the headspace method. All reliable analyses were at

background levels (4–10 parts per million by volume [ppmv]) for methane, and ethane was present in detectable amounts only in a few cores deeper than 350 mbsf.

Carbon and Elemental Analyses

Sixty-five sediment samples were analyzed for inorganic carbon (IC; calcium carbonate), and 27 selected (darker colored) samples from Site 1167 were analyzed for total carbon, OC (by difference), TN, and TS. The results are reported in Table T6. IC and OC contents are plotted against depth in Figure F27. Carbonate content is generally low (~0.1 wt% IC) with two samples having 0.4 wt% IC.

OC content averages ~0.4 wt% and shows no apparent trend with depth. Only two samples (at 279.03 and 409.04 mbsf) approach 1 wt% OC.

TN contents are generally <0.04 wt%, except for the two deepest samples analyzed (433.59 and 441.91 mbsf). These samples have carbon/nitrogen values (1.0 and 0.7) that are so low, it suggests that the slightly elevated TN contents are spurious measurements.

TS contents are uniformly low, with many samples having no detectable sulfur.

T6. Carbon, nitrogen, and sulfur analyses of sediments, p. 90.

F27. Weight percent inorganic carbon and organic carbon in sediments, p. 67.

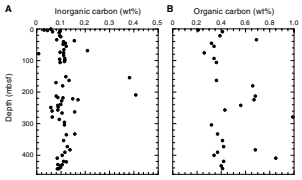

Organic Matter Characterization

Nine samples from Site 1167 were characterized by Rock-Eval pyrolysis (Table T7). Samples with >0.5 wt% OC were selected for analysis. Pyrolyzable hydrocarbons (S_2 yields) range from 0.09 to 0.21 mg of hydrocarbon/g of sediment. The pyrolyzable fraction of the OC is uniformly low (hydrogen index values of 17–38 mg of hydrocarbon/g of carbon). The elevated T_{max} values (451°–534°C) and the broad S_2 peak shapes in the pyrograms (not shown) indicate that all samples contain predominantly recycled and degraded thermally mature organic matter.

T7. Organic carbon and Rock-Eval pyrolysis on selected samples, p. 91.

PHYSICAL PROPERTIES

Multisensor Track

Measurements with the multisensor track (MST) were obtained at 4-cm intervals for gamma-ray attenuation (GRA) bulk density, *P*-wave velocity, and magnetic susceptibility. Natural gamma radiation (NGR) was measured at 12-cm intervals. No *P*-wave velocity data were recorded on XCB cores (i.e., below 39.7 mbsf). MST results in XCB cores were degraded in quality because of drilling disturbance associated with coring and incompletely filled core liners. This disturbance is illustrated by a comparison of GRA bulk densities with discrete density determinations (see "Moisture and Density Measurements," p. 26). In Figure F28, we present edited MST data from Hole 1167A measured on APC cores (0–40 mbsf). Measurements from deeper intervals may also be useful in discerning lithologic changes but need extensive postcruise editing. This is exemplified by apparent 20-cm-scale cyclic changes in GRA bulk densities, which are pervasive in the XCB-cored part of the hole, and which are the result of spiraling gouges produced by the core catcher on the outer surface of the sample. The MST measurements are available (see the "Related Leg Data" contents list).

F28. GRA bulk-density, PWL, MS, and NGR measurements from Hole 1167A, p. 68.

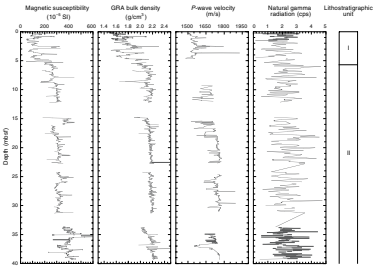

GRA bulk density, *P*-wave velocity, and magnetic susceptibility exhibit similar downhole patterns for the upper 40 mbsf at Site 1167. Throughout lithostratigraphic Unit I (0–5.72 mbsf), these parameters show a large variability (magnetic susceptibility: 90 × 10^{-5} to 310 × 10^{-5} SI, GRA bulk density: 1.55–2 g/cm³, *P*-wave velocity: 1500–1650 m/s), possibly reflecting latest Pleistocene and Holocene glacial–interglacial changes in hemipelagic sedimentation. The transition from Unit I to Unit II is characterized by an abrupt step to higher density (~2.2 g/cm³) and magnetic susceptibility (~300 × 10^{-5} SI) values. No *P*-wave data were recorded for this transition. Sediment at the top of lithostratigraphic Unit II (5.72–40 mbsf) displays relatively uniform physical properties with a slight trend to increasing values downhole, a response to gravitational sediment compaction. Offsets from a trend to higher magnetic susceptibilities (~400 × 10^{-5} SI) occur at 15–16 mbsf and below 35 mbsf. Farther downhole, the magnetic susceptibilities show a sawtooth-like trend that is also apparent in the discrete magnetic measurements (see **"Paleomagnetism,"** p. 19, for more details).

NGR measurements from Site 1167 vary between 1 and 3 cps (Fig. **F29**) throughout the hole. The 20-m moving average, however, shows some subtle changes. It is fairly constant for the upper 320 m, except for a slight increase at ~210 mbsf that may be a response to the clay beds found at this level (see **"Lithostratigraphy,"** p. 7). Clays normally contain more radioactive elements than sands. The LWD tool (see **"Downhole Measurements,"** p. 31), however, indicates a decrease in NGR at ~210 mbsf, a difference that may reflect either the inaccuracies in MST measurements over rather short intervals compared to the LWD tool or different instrumental sensitivities to the various parts of the gamma-ray spectrum. The changes observed at ~210 mbsf in many parameters prompted binning of the NGR spectra above and below 200 mbsf. No significant difference can be seen between these two spectra (Fig. **F29**). At ~320 mbsf, there is a slight decrease in the NGR values. There are no changes in other physical properties at this level, except for the offset in the ARM and IRM (see **"Paleomagnetism,"** p. 19).

F29. Bulk mineralogy from XRD, NGR, and binned natural gamma spectra vs. depth, p. 69.

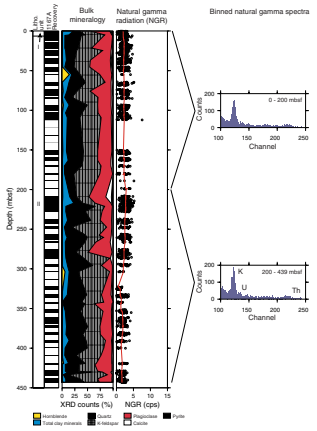

Moisture and Density Measurements

Gravimetric and volumetric determinations of moisture and density (MAD) were made for 138 samples from Hole 1167A (Cores 188-1167A-1H through 49X). One sample was taken, where possible, from each section of each core. Wet mass, dry mass, and dry volume were measured and used to calculate percentage water weight, porosity, dry density, bulk density, and grain density (see **"Physical Properties,"** p. 21, in the "Explanatory Notes" chapter; also see the **"Related Leg Data"** contents list for available raw data).

The grain densities measured at Site 1167 are shown in Figure **F30.** Eight determinations of grain density were made in lithostratigraphic Unit I (0–5.72 mbsf), giving an average value of 2.70 g/cm³ with a range of 2.65–2.74 g/cm³. Within Unit I, the measured values show no trend with depth.

A total of 130 determinations of grain density were made in lithostratigraphic Unit II (5.72–443.70 mbsf). From 5.72 to 210 mbsf, the mean value is 2.70 g/cm³, with a range of 2.67–2.74 g/cm³ (67 measurements). Over this interval, there is no trend in the values with depth. At ~210 mbsf, the grain density abruptly decreases, and from 210 to

F30. Grain density and porosity from discrete measurements, p. 71.

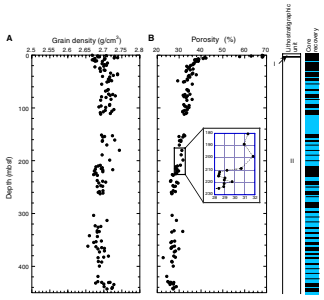

443.70 mbsf, the mean value is 2.69 g/cm³, with a range of 2.66–2.73 g/cm³ (63 measurements).

The porosities measured at Site 1167 are shown in Figure **F30.** Eight determinations of porosity were made in lithostratigraphic Unit I. Within the unit (0–5.72 mbsf), the porosity decreases sharply with depth, dropping from a value of 68.1% at 0.30 mbsf to 42.3% at 5.54 mbsf. The average value of porosity in Unit I is 59.7%. The decrease in porosity from the top to the bottom of Unit I is attributed to compaction under increasing effective overburden stresses.

A total of 67 determinations of porosity were made from the top of lithostratigraphic Unit II (5.72 mbsf) to 210 mbsf. Within this interval, the porosity decreases with depth, from 41.0% at 6.43 mbsf to ~31% at 210 mbsf. About half of this decrease occurs in the upper 10 m of the unit. At 210 mbsf, the porosity abruptly decreases; from 210 to 443.70 mbsf, the mean value is 27.6%, with a range of 22.7%–31.7% (57 measurements).

Other parameters that are derived from the measured data include bulk density, dry density, water content, and void ratio. Bulk-density and dry density values are presented in Figure **F31.** Eight determinations of bulk density were made in lithostratigraphic Unit I. Within the unit (0–5.72 mbsf), the bulk density increases sharply with depth, rising from a value of 1.55 g/cm³ at 0.30 mbsf to 2.01 g/cm³ at 5.54 mbsf. The average value of bulk density in Unit I is 1.70 g/cm³. The increase in bulk density from the top to the bottom of Unit I is attributed to compaction under increasing effective overburden stresses.

A total of 67 determinations of bulk density were made from the top of lithostratigraphic Unit II (5.72–210 mbsf). Within this interval, the bulk density increases with depth, from 2.00 g/cm³ at 6.43 mbsf to ~2.19 g/cm³ at 210 mbsf. About half of this increase occurs in the upper 10 m of the unit. At 210 mbsf, the bulk density abruptly increases to 2.21 g/cm³. From 210 to 443.70 mbsf, the mean value is 2.23 g/cm³, with a range of 2.16–2.31 g/cm³ (57 measurements). The bulk density gradually increases with depth, from ~2.21 g/cm³ at 210 mbsf to ~2.25 g/cm³ at 443.7 mbsf.

Water content (as a percentage of dry mass corrected for salt content) and void ratio are presented in Figure **F32.** These plots show trends similar to those observed in the porosity data.

The decrease in grain density and porosity—and hence in bulk density, dry density, water content, and void ratio—at 210 mbsf correlates with a sharp drop in magnetic susceptibility seen at about the same depth (see **"Paleomagnetism,"** p. 19). Analysis of the clasts found in the diamict of Unit II shows that above 210 mbsf more granite and other igneous clasts are present, whereas below 210 mbsf more sandstone clasts are present (see **"Lithostratigraphy,"** p. 7). This suggests that the physical property changes observed in the sediment at 210 mbsf are a result of a change of provenance of the diamict, and hence, differing ice-flow configurations.

As described previously in this section (see **"Multisensor Track,"** p. 25), bulk-density data were obtained from the GRA bulk densiometer in addition to the discrete MAD measurements. To compare the GRA bulk-density data to the discrete MAD measurements, the GRA data set was cleaned by removing the data points at the top of each core section as well as any data points <1.0 g/cm³. Figure **F33A** presents the cleaned GRA data, superimposed on the bulk densities computed from the discrete MAD measurements. The plot demonstrates that there is good

F31. Bulk density and dry density from discrete measurements, p. 72.

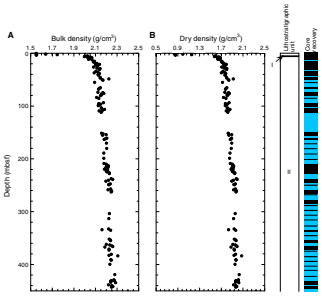

F32. Water content and void ratio from discrete measurements, p. 73.

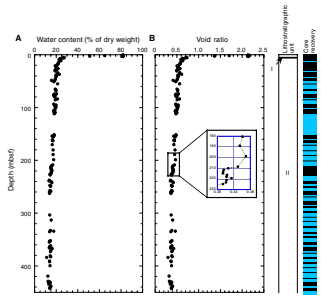

F33. GRA bulk-density data vs. bulk density from MAD measurements, p. 74.

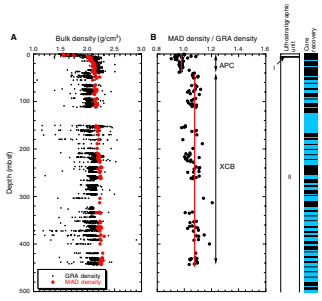

agreement between the two measurement methods to ~40 mbsf and that below this depth the discrete measurements are consistently higher than the GRA measurements. The ratio of the discrete bulk-density measurements to the GRA measurements for corresponding depths (Fig. F33B) is relatively constant and is equal to 0.975 for APC cores (0–39.7 mbsf) and 1.076 for XCB cores (39.7–443.7 mbsf). These ratios agree well with those determined at Site 1165 (see "Moisture and Density Measurements," p. 56, in the "Site 1165" chapter). This indicates that different calibration constants should be used for the GRA bulk densiometer depending on the coring method being employed or that GRA measurements on different core types using the same GRA bulk densiometer calibration should be scaled to correct the measurements.

Velocimetry

P-wave velocities on split cores were measured at a frequency of one measurement per recovered section. The velocity probes *P*-wave sensor (PWS1 and PWS2), which allow measurements in z- and y-directions in soft sediments, were used on Cores 188-1167A-1R through 3R. Below 24 mbsf, the sediments became too stiff to insert the probes and *P*-wave velocities were measured in the x-direction (through the core liner) by using probe PWS3. In some intervals blocks of consolidated sediment were cut out, and the *P*-wave velocity was measured in x-, y-, and z-directions by using PWS3. The laboratory velocity measurements presented here (Fig. F34) were not corrected to in situ temperature and pressure conditions. Velocity data are compiled in Table T8 (also see the "Related Leg Data" contents list).

From 2 to 60 mbsf (lithostratigraphic Unit 1 and the top of Unit 2), *P*-wave velocities at Site 1167 increase from 1503 to 1986 m/s, which results in a velocity gradient of 9.7 s^{-1} and is most likely related to sediment compaction. Below 60 mbsf, the homogeneous sediment composition in lithostratigraphic Unit II is reflected by a relatively uniform *P*-wave velocity, which increases slightly to values of ~2200 m/s close to the bottom of the hole (445 mbsf). The change in the velocity gradient at 60 mbsf correlates with a significant drop in magnetic susceptibility (see "Paleomagnetism," p. 19), which could indicate a general change in sediment composition. No corresponding change, however, is seen in the MAD parameters. The most prominent velocity feature in Unit II is a steplike increase in average velocity from 1986 to 2115 m/s below 181 mbsf, which correlates with a drop in porosity and a change to lower grain density. This feature is possibly caused by a higher quartz content below 181 mbsf, as indicated by XRD results.

Undrained Shear Strengths

A total of 27 automatic vane shear (AVS), 71 fall cone (FC), and 103 pocket penetrometer (PP) measurements were obtained, with results spanning the entire recovered interval (Table T9). Down to 50 mbsf, FC and AVS measurements were taken, whereas FC and PP measurements were made between 60 and 300 mbsf. Below 300 mbsf, the sediment strength was only within the range of PP measurements. The FC measurements gave higher shear strengths than either the AVS and the PP. AVS measurements may be too low because of the lack of confinement of the samples, allowing horizontal deformation and/or cracking of the sediment during vane rotation. The FC and PP gave similar shear strengths at Sites 1165 and 1166. The difference observed in Hole

F34. Discrete velocity measurements obtained with the PWS, p. 75.

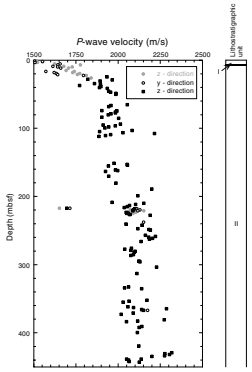

T8. Discrete *P*-wave measurements, p. 92.

T9. Measurements of undrained shear strength, p. 93.

1167A might therefore be a consequence of the sediment composition below 60 mbsf at this site.

The shear strengths (C_u) increase constantly with depth (Fig. F35), reaching ~600 kPa on sediments from the lower part of the hole. The high value of 1000 kPa at ~420 mbsf is a minimum value for a sample from the core catcher in Core 188-1167A-46X and may be from a carbonate cemented layer.

The ratio between shear strength and effective overburden stress (C_u/p'_0) is expected to be between 0.25 and 0.35 for a normally compacted sediment (Fig. F36, shaded region) of intermediate plasticity (Brooker and Ireland, 1965; Andresen et al., 1979). The normalized shear strengths show that the sediments at Site 1167 are normally consolidated in the upper 50 mbsf of the hole. Below the core break between ~50 and 60 mbsf, the normalized shear strength values fall below the expected region and remain so for the rest of the hole. This transition is at the same depth as transitions observed in velocimetry and magnetic susceptibility (see "Paleomagnetism," p. 19) and may therefore be a result of the composition of the sediments. High silt and sand contents and a predominance of kaolinite in the clay minerals (see "Lithostratigraphy," p. 7) contribute to low plasticities and may therefore be conducive to reducing the expected normalized shear strengths at this site. Alternatively, the cores may have been slightly disturbed by the drilling and coring process. However, the change from APC to XCB coring at ~40 mbsf (Fig. F36) does not seem to have influenced the shear strength in this hole.

The sediments at Site 1167 reveal a compaction history that is not influenced by loads greater than those of the present sediment overburden.

Thermal Conductivity

Thermal conductivity was measured using a full-space needle probe (see "Physical Properties," p. 21, in the "Explanatory Notes" chapter; also see the "Related Leg Data" contents list for available raw data). Where possible, thermal conductivity was measured twice per core on both APC and XCB cores, usually near the middle of the sections.

A total of 68 thermal conductivity measurements were made (Table T10; Fig. F37). The data show a rapidly increasing thermal conductivity profile through lithostratigraphic Unit I, starting at 1.071 W/(m·°C) at 0.75 mbsf and increasing to 1.395 W/(m·°C) at 3.75 mbsf. This rapid increase is attributed to a corresponding increase in dry density over the same depth interval (see "Moisture and Density Measurements," p. 26).

At the top of Unit II, the thermal conductivity continues to increase to 2.026 W/(m·°C) at 21.45 mbsf. Similar to Unit I, this increase corresponds to the increase in dry density over the interval 5.95–21.45 mbsf. From 21.45 to 66.55 mbsf, the thermal conductivity decreases to 1.294 W/(m·°C). There is no corresponding change in dry density, nor is there a change in the grain density that might indicate a change in mineralogy.

Below ~70 mbsf, the thermal conductivity abruptly increases to ~1.62 W/(m·°C) and increases slightly with depth to ~1.69 W/(m·°C) at 198.9 mbsf. This trend is interrupted by a pair of thermal conductivities of ~1.86 W/(m·°C) at 151 and 155 mbsf.

F35. Measurements of undrained shear strength using the AVS, FC, and PP, p. 76.

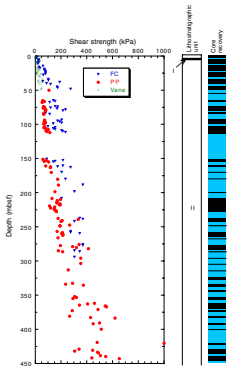

F36. Normalized undrained shear strength with respect to effective overburden pressure, p. 77.

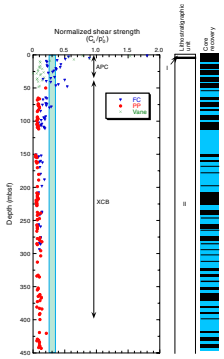

T10. Measurements of thermal conductivity, p. 94.

F37. Thermal conductivity measurements, p. 78.

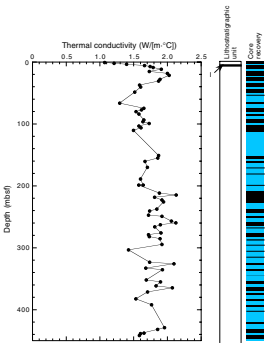

At 210 mbsf, the thermal conductivity increases abruptly to 1.89 W/(m·°C). This value is maintained to a depth of 295 mbsf. The abrupt increase at 210 mbsf corresponds to an abrupt decrease in the grain density (see "Moisture and Density Measurements," p. 26) and is therefore attributed to a change in the sediment mineralogy. This change of mineralogy is also indicated by an abrupt decrease in the magnetic susceptibility at 210 mbsf, associated with a downhole change from coarser (above 120 mbsf) to finer magnetite grains at this depth (see "Paleomagnetism," p. 19). Below 295 mbsf to 443.7 mbsf, the thermal conductivity decreases slightly to an average value of 1.77 W/[m·°C]) over the length of the interval.

Summary

There are two major changes observed in the physical properties at Site 1167. The first is at 5.9 mbsf at the transition between lithostratigraphic Units I and II and is associated with an abrupt increase in magnetic susceptibility and a change to a lower gradient in density. An increase in the *P*-wave velocity also appears at this depth, but the PWL data for the transition was not obtained on the MST. The other change is at 210 mbsf, where a downhole decrease in grain density and porosity and an increase in bulk density are found. The change at 5.9 mbsf most likely is due to the combined effect of gravitational compaction and the increasing content of sand down through Core 188-1167A-1H (see "Lithostratigraphy," p. 7) and into the diamicts of Core 188-1167A-2H. The change of physical properties at 210 mbsf indicates a change in mineralogy as seen in the downhole shift to lower grain density. The bulk mineralogy (Fig. F29) suggests that there is a downward increase in quartz and a reduction in the plagioclase contents at this level. These changes imply that the sediment source area shifted, likely in response to reconfiguration of the glacier drainage on the Antarctic continent.

IN SITU TEMPERATURES

At Site 1167, because of a rapid downward increase in induration of the sediments, only one Adara temperature tool measurement from Core 188-1167A-5H (39.7 mbsf) was made. The seafloor temperature (T_{SF}) and stabilized sediment temperature were determined using the TFIT software package (Table T11; Fig. F38). From these data, a geothermal gradient of 17.1°C/km was estimated.

The heat flow and downhole temperatures were estimated according to the methodology described in "In Situ Temperatures," p. 62, in the "Site 1165" chapter. Using a measured thermal conductivity of 1.59 W/(m·°C) (see "Physical Properties," p. 25), the heat flow was determined to be 27.2 mW/m². The estimated temperature at total depth (441.7 mbsf) was determined to be 7.1°C (Table T11; Fig. F39). The geothermal gradient and heat flow values (17.1°C/km and 27.2 mW/m², respectively) (Table T11) are significantly less than those determined for Site 1165 (53.4°C/km and 51.4 mW/m², respectively) (see "In Situ Temperatures," p. 62, in the "Site 1165" chapter).

This difference in thermal conditions at Sites 1167 and 1165 may be due to differing thermal conductivities and sedimentation rates. At Site 1167, the thermal conductivity is 1.6 W/(m·°C) over the upper 100 mbsf (see "Physical Properties," p. 25); however, over a similar depth interval at Site 1165, the mean measured thermal conductivity was sig-

T11. Measured and estimated temperatures, geothermal gradients, and heat-flow estimates, p. 95.

F38. Measured temperature vs. time from deployment of the Adara temperature tool for Core 188-1167A-4H, p. 79.

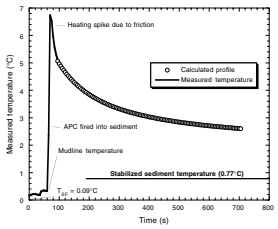

F39. Measured and estimated temperature vs. depth profile, p. 80.

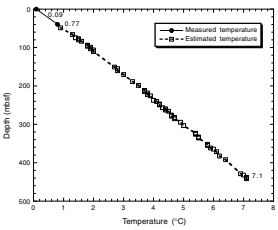

nificantly lower, at 0.90 W/(m·°C) (see "Physical Properties," p. 54, in the "Site 1165" chapter). In general, the thermal conductivities were higher throughout the sediment section at Site 1167. This higher thermal conductivity at Site 1167 allows for a greater rate of heat loss from the sediments. Also, sedimentation rates are higher at Site 1167 (up to ~400 m/m.y.) (see "Sedimentation Rates" p. 19, in "Biostratigraphy and Sedimentation Rates") than at Site 1165 (15 m/m.y. in the uppermost Miocene to Pleistocene section) (see "Biostratigraphy and Sedimentation Rates," p. 21, in the "Site 1165" chapter). The high sedimentation rate at Site 1167 may have significantly reduced the thermal profile of the sediments compared to that of Site 1165.

The depth to the base of the gas hydrate stability zone (GHSZ) was determined using the Ocean Drilling Program Pollution Prevention and Safety Panel hydrate stability equation, which was modified for seawater (Pollution Prevention and Safety Program, 1992). As only a small variation in the downhole thermal gradients was noted (Table T11), only the initial measured thermal gradient of 17.1°C was used to estimate the base of the GHSZ at 1190 mbsf.

DOWNHOLE MEASUREMENTS

Operations

Downhole measurements were made after completion of APC/XCB coring in Hole 1167A and while drilling Hole 1167B. During coring, operational problems were experienced with the drill pipe sticking and the lockable flapper valve jamming with sediment. Hole conditioning involving a wiper trip and circulation of 195 barrels of sepiolite mud was therefore undertaken prior to logging. Despite this precaution, however, similar problems hampered wireline operations in Hole 1167A.

The triple combo tool, which measures resistivity, density, porosity, and natural gamma, was the only tool string run in Hole 1167A (Fig. F40; Table T12). While exiting the pipe during the initial run into the hole, the triple combo got stuck with only 10 m of the tool string protruding out of the base of the pipe. It was likely that the lockable flapper valve had not latched open properly when the go-devil was pumped downhole. The problem was resolved by rigging up the circulator and increasing the pump pressure until the tool string eventually came free. After these initial difficulties, the triple combo tool string was lowered to 151 mbsf, where its passage downhole was halted by an obstruction. A conglomerate interval was observed in the cores at this depth, and the drillers had noted sticking just below this depth while pulling pipe for both the wiper trip and while waiting for an iceberg to pass.

The hole was logged from 151 mbsf up to the base of pipe at 85 mbsf, covering an interval of 66 m, without extending the HLDS caliper arm. The depth to the seafloor was determined to be 1649 mbrf from the decrease in gamma-ray values at the sediment/water interface (driller's mudline depth = 1651.3 mbrf) (Table T12).

High tension was recorded at the head of the tool when the tool string entered the pipe, even with continued pumping. Because of time constraints, poor hole conditions, problems encountered with the lockable flapper valve, and the high probability of our encountering further difficulties, we decided to switch to LWD.

F40. Logging summary diagram, p. 81.

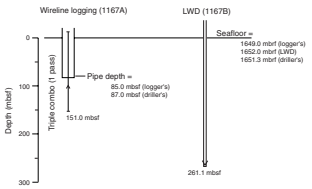

T12. Logging operations summary, p. 96.

Logging While Drilling/ Measurement While Drilling

LWD operations were carried out in Hole 1167B, offset by 50 m from Hole 1167A. The aims of LWD/MWD at this hole were twofold: to record spectral gamma and resistivity logs with the compensated dual resistivity (CDR) LWD tool and to record weight on bit and other drilling parameters for the engineering experiment on the efficacy of the passive heave compensation system. The spudding of Hole 1167B was delayed for 4 hr by a storm; spudding with LWD tools required low heave because the tools were narrower and hence weaker than the drill collars above them. Low pump rates were used for the top 17 m of the hole, so looser sediment was not washed away to leave a wide hole that would have degraded resistivity and natural gamma readings. However, measurement-while-drilling (MWD) communications required a higher pump rate of 70 spm (350 gal/min), so below 17 mbsf, the pump rate was increased and the MWD tool began communication. The data transmission rate was 3 bits/s, and the frequency of the mud pulse was 12 Hz; no problems were experienced with MWD data transmission. The hole was drilled to 261.1 mbsf at an average rate of 22 m/hr.

For the engineering experiment, data were recorded under a range of operating conditions from low weight on bit in softer formations to 25 KlbF (1000 lb force) in harder formations in the deeper parts of the hole. The amplitude of the heave varied considerably during the course of drilling.

Total gamma-ray emission and resistivity data from the CDR were downloaded from the tool when it came back to the surface. The data were then processed by the Anadrill engineer to move the data from evenly spaced time intervals to a depth scale. Correlation with the overlapping interval of wireline logs was mostly good (Fig. F41). Differences can be attributed to washouts in the wireline-logged hole that caused intervals of anomalously low natural gamma, resistivity, density, and porosity logs. LWD measurements are made only minutes after the hole is drilled, so the borehole is likely to be in good condition for logging. Although the total natural gamma data from the CDR were good, the logs derived from the natural gamma spectrum (potassium, thorium, and uranium) required further processing.

F41. Gamma-ray, resistivity, density, and porosity logs, p. 82.

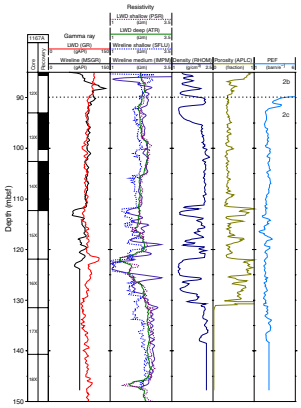

Logging Units

Unit 1 (0–8 mbsf)

Unit 1 is a clay-rich unit, corresponding to lithostratigraphic Unit I. It is characterized by slightly higher gamma-ray values and lower resistivity values relative to the underlying unit. Resistivity values are low at the surface because the sediments are soft and less lithified; however, a relatively rapid increase in resistivity with depth is observed as a result of compaction.

Unit 2 (8–257 mbsf)

A general compaction trend of increasing resistivity values is observed with depth. Clay-rich beds can be detected as drops in the resistivity values (Fig. F42). The gamma-ray log highlights the presence of a more radioactive interval at 62–90 mbsf, coincident with a red-colored interval seen at 65–84 mbsf. The lower radioactivity levels observed be-

F42. Gamma-ray and resistivity logs and core susceptibility, p. 83.

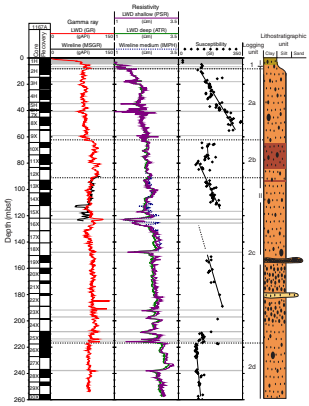

tween 90 and 120 mbsf and from 215 to 255 mbsf may correspond to a decrease in the proportion of granitic clasts or a change from a clay-rich to a sandier matrix.

Subunit 2a (8–62 mbsf)

This subunit is characterized by relatively low gamma-ray values and increasing resistivity with depth. There are thin intervals with low resistivity and low gamma-ray values at 18, 35, and 41 mbsf. A clay bed was observed in Core 188-1167A-5H, and since clay beds generally have a lower resistivity than diamict, we are inclined to interpret the resistivity lows as clay beds within the diamict. However, clay layers might not be expected to have the observed lower gamma-ray values because they contain radioactive potassium and thorium. On the other hand, it is quite likely that K-feldspars and heavy minerals contribute significantly to the natural gamma signal at this site, so that an increase in clay minerals would have a minor effect on the logs. Possible alternative lithologies for the low-resistivity intervals are clay with microfossils, silty or sandy clay, or perhaps gravels.

Subunit 2b (62–90 mbsf)

This subunit has higher gamma-ray values than the subunits above and below; it contains no major drops in resistivity. Red-colored beds are observed in the core from this interval.

Subunit 2c (90–216 mbsf)

This subunit is similar to Subunit 2a, apart from having generally higher resistivities attributed to compaction with depth. It contains several drops in resistivity; those at 213 and 215 mbsf were observed in Core 188-1167A-25X as clay beds. In contrast to Subunit 2a, these resistivity lows are accompanied by natural gamma highs (Fig. **F42**). A major interval of resistivity lows (116–127 mbsf) is found in a zone of zero core recovery. Conglomerate and sand beds were observed in Cores 188-1167A-19X and 22X respectively; they are tentatively correlated with small positive peaks in the resistivity log at 153 and 181 mbsf. However, the conglomerate bed might also be the cause of the large low in resistivity values at 148 mbsf if the material between the clasts is poorly compacted (which is conceivable since the conglomerate is clast supported).

Subunit 2d (216–255 mbsf)

This subunit is defined by a drop in the gamma-ray values relative to Subunit 2c, above. This is likely to be related to the decrease in granitic clasts and the increase in sandstone clasts observed in the cores around this depth; granites are typically more radioactive than sandstones. Resistivities in the upper part of Subunit 2d are higher than in Subunit 2c; there is one drop in resistivity at 235 mbsf.

Resistivity Lows, Clay Beds, and the Trends in Magnetic Susceptibility

We interpret the thin intervals of low-resistivity values as clay beds, given the known low resistivity of clay compared to diamict and the absence of other major lithologies from the cores in the logged interval. The position of the clay beds appears to be related to the "sawtooth" trends observed in the core magnetic susceptibility record (Fig. **F42**). Clay beds are found at the step in susceptibility values at 116–127 mbsf

and 190–126 mbsf, but the relationship is not so clear cut in the upper 100 m of the hole.

Temperature Log

The Lamont-Doherty Earth Observatory temperature-acceleration-pressure (TAP) tool recorded the temperature of the fluid in Hole 1067A as the triple combo tool string was run (Fig. F43). The measurements underestimate the formation temperature, as the fluid temperature does not have time to equilibrate to the formation temperature. A temperature of 4.5°C was recorded at 151 mbsf. The downgoing and upgoing curves have an offset, owing to the borehole still reequilibrating during acquisition.

F43. Downhole temperatures from the TAP tool, p. 84.

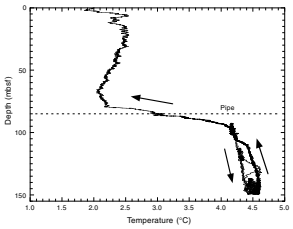

REFERENCES

Andresen, A., Berre, T., Kleven, A., and Lunne, T., 1979. Procedures used to obtain soil parameters for foundation engineering in the North Sea. *Norw. Geotech. Inst. Publ.,* 129:1–18.

Anson, G.L., and Kodama, K.P., 1987. Compaction-induced shallowing of the post-depositional remanent magnetization in a synthetic sediment. *Geophys. J. R. Astron. Soc.,* 88:673–692.

Arason, P., and Levi, S., 1990. Compaction and inclination shallowing in deep-sea sediments from the Pacific Ocean. *J. Geophys. Res.,* 95:4501–4510.

Barker, P.F., Camerlenghi, A., Acton, G.D., et al., 1999. *Proc. ODP, Init. Repts*. [CD-ROM], 178: College Station, TX (Ocean Drilling Program).

Berggren, W.A., 1992. Neogene planktonic foraminifer magnetobiostratigraphy of the southern Kerguelen Plateau (Sites 747, 748, and 751). *In* Wise, S.W., Jr., Schlich, R., et al., *Proc. ODP, Sci. Results,* 120 (Pt. 2): College Station, TX (Ocean Drilling Program), 631–647.

Berggren, W.A., Kent, D.V., Swisher, C.C., III, and Aubry, M.-P., 1995. A revised Cenozoic geochronology and chronostratigraphy. *In* Berggren, W.A., Kent, D.V., Aubry, M.-P., and Hardenbol, J. (Eds.), *Geochronology, Time Scales and Global Stratigraphic Correlation*. Spec. Publ.—Soc. Econ. Paleontol. Mineral. (Soc. Sediment. Geol.), 54:129–212.

Boulton, G. S., 1990. Sedimentary and sea level changes during glacial cycles and their control on glaciomarine facies architecture. *In* Dowdeswell, J.A., and Scourse, J.D. (Eds.), *Glacimarine Environments: Processes and Sediments*. Geol. Soc. Spec. Publ. London, 53:15–52.]

Bouma, A.H., 1962. *Sedimentology of Some Flysch Deposits: A Graphic Approach to Facies Interpretation:* Amsterdam (Elsevier).

Brooker, E.W., and Ireland, H.O., 1965. Earth pressures at rest related to stress history. *Can. Geotech. J.,* 2:1–15.

Domack, E., O'Brien, P.E., Harris, P.T., Taylor, F., Quilty, P.G., DeSantis, L., and Raker, B., 1998. Late Quaternary sedimentary facies in Prydz Bay, East Antarctica and their relationship to glacial advance onto the continental shelf. *Antarct. Sci.,*10:227–235.

Dunlop, D.J., 1979. One the use of Zijderveld vector diagrams in multicomponent paleomagnetic studies. *Phys. Earth Planet. Inter.,* 20:12–24.

Ehrmann, W.E., and Fütterer, D.K., 1994. Clay mineral assemblages in the Cenozoic Antarctic Ocean. *Terra Antart.,* 1:475–476.

Findlay, C.S., 1998. Living and fossil calcareous nannoplankton from the Australian sector of the Southern Ocean: implications for paleoceanography [Dissert.]. Univ. of Tasmania, Hobart.

Forsberg, C.F., Solheim, A., Elverhøi, A., Jansen, E., Channell, J.E.T., and Andersen, E.S., 1999. The depositional environment of the western Svalbard margin during the late Pliocene and the Pleistocene: sedimentary facies changes at Site 986. *In* Raymo, M.E., Jansen, E., Blum, P., and Herbert, T.D. (Eds.), *Proc. ODP, Sci. Results,* 162: College Station, TX (Ocean Drilling Program), 233–246.

Jacobs, J.A., 1994. *Reversals of the Earth's Magnetic Field* (2nd ed.): Cambridge (Cambridge Univ. Press).

Larter, R.D., and Cunningham, A.P., 1993. The depositional pattern and distribution of glacial-interglacial sequences on the Antarctic Peninsula Pacific Margin. *Mar. Geol.,* 109:203–219.

Lazarus, D., 1992. Antarctic Neogene radiolarians from the Kerguelen Plateau, Legs 119 and 120. *In* Wise, S.W., Jr., Schlich, R., et al., *Proc. ODP, Sci. Results,* 120: College Station, TX (Ocean Drilling Program), 785–809.

Lowrie, W., 1990. Identification of ferromagnetic minerals in a rock by coercivity and unblocking temperature properties. *Geophys. Res. Lett.,* 17:159–162.

Mizukoshi, I., Sunouchi, H., Saki, T., Sato, S., and Tanahashi, M., 1986. Preliminary report of geological geophysical surveys off Amery Ice Shelf, East Antarctica. *Mem. Nat. Inst. Polar Res. Spec. Iss. Jpn.,* 43:48–61.

O'Brien, P.E., De Santis, L., Harris, P.T., Domack, E., and Quilty, P.G., 1999. Ice shelf grounding zone features of western Prydz Bay, Antarctica: sedimentary processes from seismic and sidescan images. *Antarct. Sci.,*11:78–91.

O'Brien, P.E., and Harris, P.T., 1996. Patterns of glacial erosion and deposition in Prydz Bay and the past behaviour of the Lambert Glacier. *Pap. Proc. R. Soc. Tasmania,*130:79–86.

Pollution Prevention and Safety Panel, 1992. Ocean Drilling Program guidelines for pollution prevention and safety. *JOIDES J.,* 18:1–24.

Quilty, P.G., 1985. Distribution of foraminiferids in sediments of Prydz Bay, Antarctica. *Spec. Publ. S. Aust. Dep. Mines Energy,* 5:329–340.

Quilty, P.G., Truswell, E.M., O'Brien, P.E., and Taylor, F., 1999. Paleocene-Eocene biostratigraphy and palaeoenvironment of East Antarctica: new data from Mac. Robertson Shelf and western Prydz Bay. *AGSO J. Aust. Geol Geophys.,* 17:133–143.

Roberts, A.P., Wilson, G.S., Florindo, F., Sagnotti, L., Verosub, K.L., and Harwood, D.M., 1998. Magnetostratigraphy of lower Miocene strata from the CRP-1 core, McMurdo Sound, Ross Sea, Antarctica. *Terra Antart.,* 5:703–713.

Samtleben, C., 1980. Die Evolution der Coccolithophoriden-Gattung *Gephyrocapsa* nach Befunden im Atlantik. *Palaontol. Z.,* 54:91–127.

Thompson, R., and Oldfield, F., 1986. *Environmental Magnetism:* London (Allen and Unwin).

Tingey, R.J., 1991. The regional geology of Archean and Proterozoic rocks in Antarctica. *In* Tingey, R.J. (Ed.), *The Geology of Antarctica:* Oxford (Clarendon Press), 1–58.

Verosub, K.L., and Roberts, A.P., 1995. Environmental magnetism: past, present, and future. *J. Geophys. Res.,* 100:2175–2192.

Villa, G., and Wise, S.W., Jr., 1998. Quaternary calcareous nannofossils from the Antarctic region. *Terra Antart.,* 5:479–484.

Weeks, R.J., Roberts, A.P., Verosub, K.L., Okada, M., and Dubuisson, G.J., 1995. Magnetostratigraphy of upper Cenozoic sediments from Leg 145, North Pacific Ocean. *In* Rea, D.K., Basov, I.A., Scholl, D.W., and Allan, J.F. (Eds.), *Proc. ODP, Sci. Results,* 145: College Station, TX (Ocean Drilling Program), 491–521.

Wei, W., and Thierstein, H.R., 1991. Upper Cretaceous and Cenozoic calcareous nannofossils of the Kerguelen Plateau (southern Indian Ocean) and Prydz Bay (East Antarctica). *In* Barron, J., Larsen, B., et al., *Proc. ODP, Sci. Results,* 119: College Station, TX (Ocean Drilling Program), 467–494.

Wei, W., and Wise, S.W., Jr., 1992. Oligocene-Pleistocene calcareous nannofossils from Southern Ocean Sites 747, 748, and 751. *In* Wise, S.W., Jr., Schlich, R., et al., *Proc. ODP, Sci. Results,* 120: College Station, TX (Ocean Drilling Program), 509–521.

Wilson, G.S., Florindo, F., Sagnotti, L., Verosub, K.L., and Roberts, A.P., in press. Magnetostratigraphy of Oligocene-Miocene glaciomarine strata from the CRP-2/2A core, McMurdo Sound, Ross Sea, Antarctica. *Terra Antart.*

Wilson, G.S., Roberts, A.P., Verosub, K.L., Florindo, F., and Sagnotti, L., 1998. Magnetobiostratigraphic chronology of the Eocene-Oligocene transition in the CIROS-1 core, Victoria Land margin, Antarctica: implications for Antarctic glacial history. *Geol. Soc. Am. Bull.,* 110:35–47.

APPENDIX

Accessory Components

The following comments are based on analysis of residues that were prepared for foraminferal study. Residues are generally large and are dominated by angular terrigenous material to a greater degree than at Sites 1165 and 1166. Residues are commonly coarse sand, and although poorly sorted, seldom show signs of bimodal size distribution; thus they are consistent (within the sample) with a single source. Detrital pyrite and traces of black coal, probably from the Permian Amery Group in the Prince Charles Mountains, are present in virtually all samples. Table AT1 summarizes our observations.

AT1. Summary of accessory components, p. 97.

The absence of sponge spicules, except in the upper section, seems anomalous in light of their abundance in Prydz Bay sediments of similar age. Shell material abundance is also less than expected. No bone or teeth were observed. Echinoid remains are present in all slope faunas yet are rare in transported continental shelf faunas. Ostracods are rare, and no pattern can be detected in their presence. In Sample 188-1167A-25X-CC, 22–23 cm, ostracods are represented by rinds of the less soluble parts of the valves, which indicates that their absence may in part be caused by dissolution. Bivalve shell fragments are present sporadically but are small and not adequate for identification purposes.

The characteristics of sand grains in the sand beds changes downhole. The shallower samples contain very immature sands with high amounts of garnet and other diverse heavy minerals. By Sample 188-1167A-25X-CC, the content of heavy minerals has decreased markedly, and residues represent very clean, white sand. Although both shallow and deeper residues contain clasts of sandstone in the coarse fraction, these clasts are dominant below Core 188-1167A-25X. Above this core, sandstone clasts are subordinate, whereas clasts with lithologies typical of the Precambrian basement of the Lambert Graben margin are predominant. This change over time may reflect an early source of mature, well-washed, well-sorted material carried initially by water, followed by the modern interval of glacially transported, less mature detritus with less opportunity for weathering and sorting to remove the heavy minerals. The change could be from a clean sandstone source (to account for the large fragments of clean sandstone in the coarse fraction) to one more dependent on the Precambrian shield of East Antarctica, or there could have been a change in the dominance of the source.

Below Core 188-1167A-25X, other variations also occur, such as a reduction in the diversity of accessories, which is evident from Table AT1, and consistent with the change in sand type referred to above. The incidence of faunas barren of foraminifers is very obvious below that depth.

Figure F1. Location of Site 1167 on the axis of the Prydz Channel Fan. Contours are in meters below sea level. Seismic line is AGSO line 149/0901.

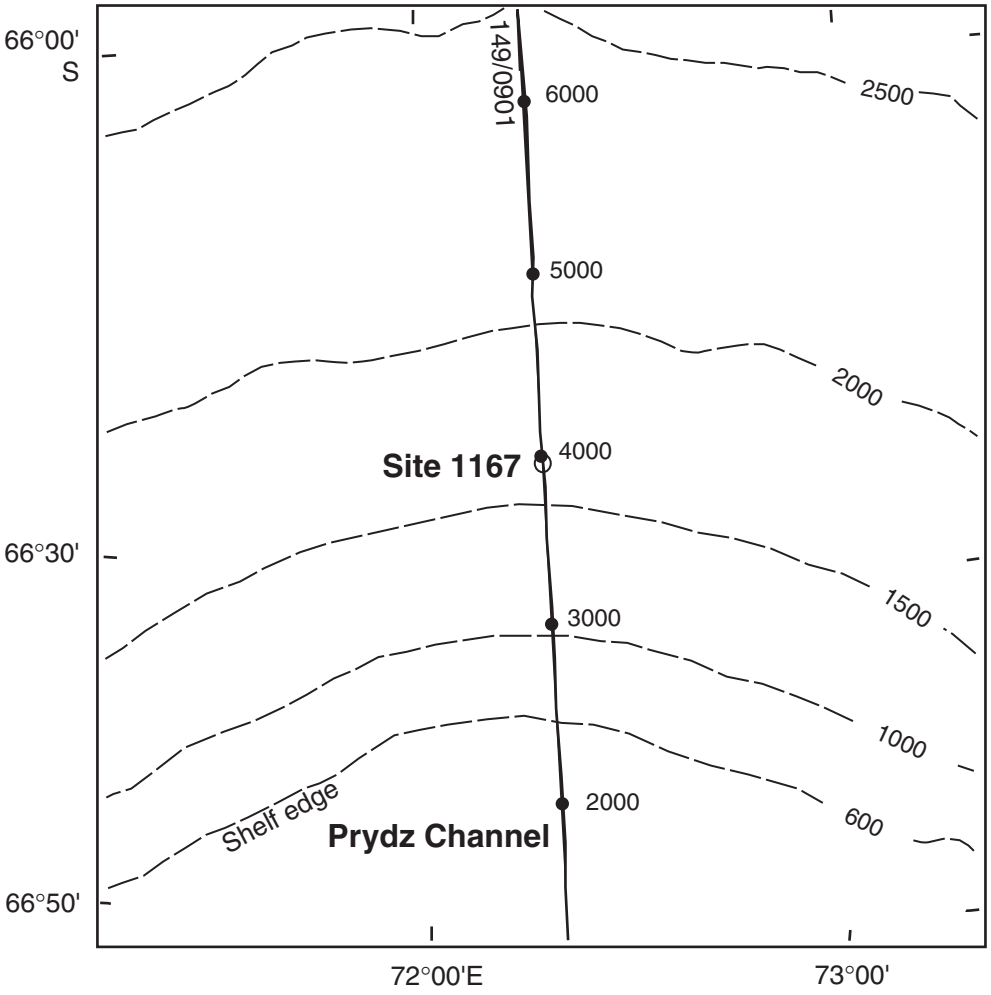

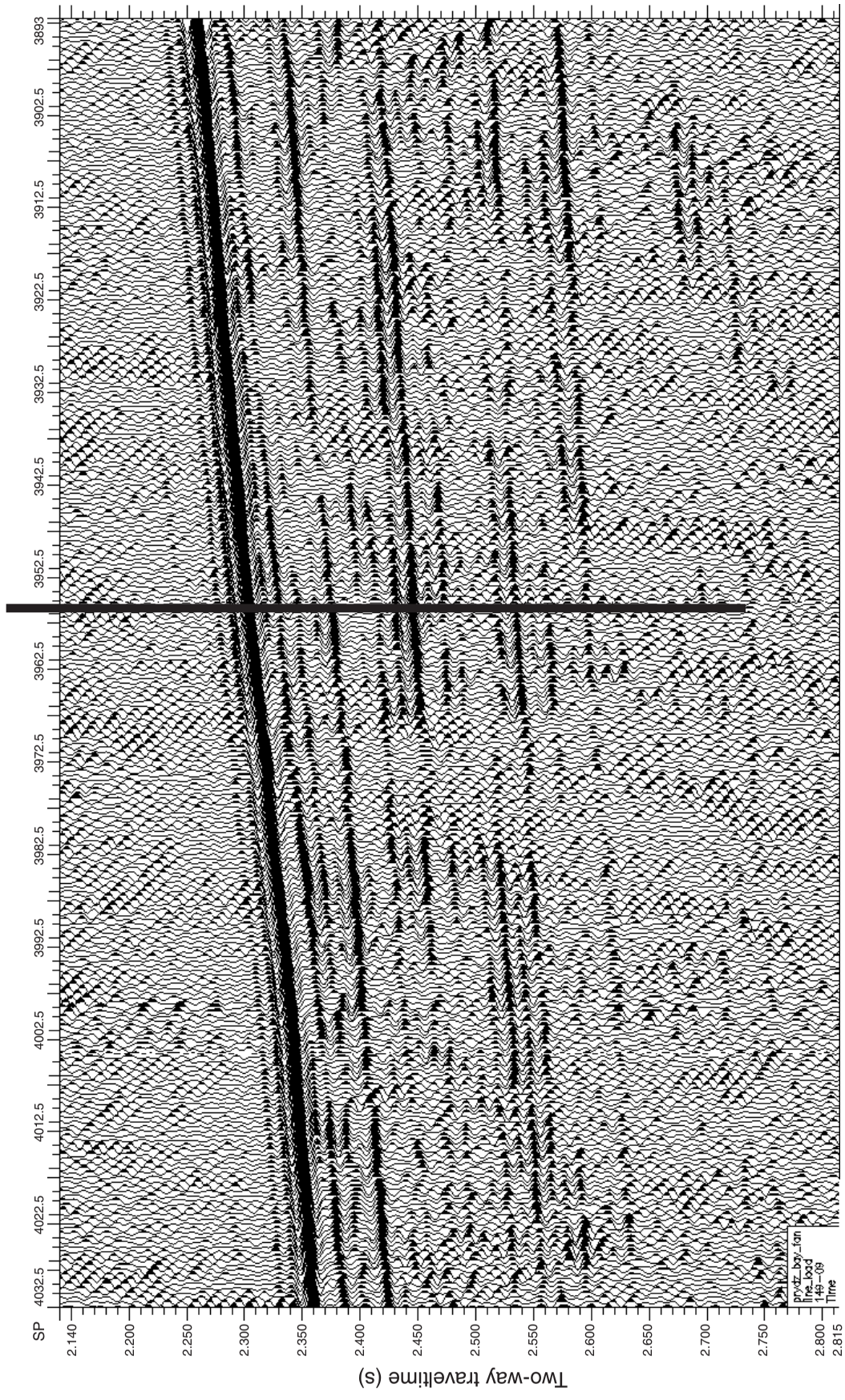

Figure F2. Part of seismic line AGSO 149/0901 through Site 1167. SP = shotpoint.

Figure F3. Site 1167 lithostratigraphic units and facies.

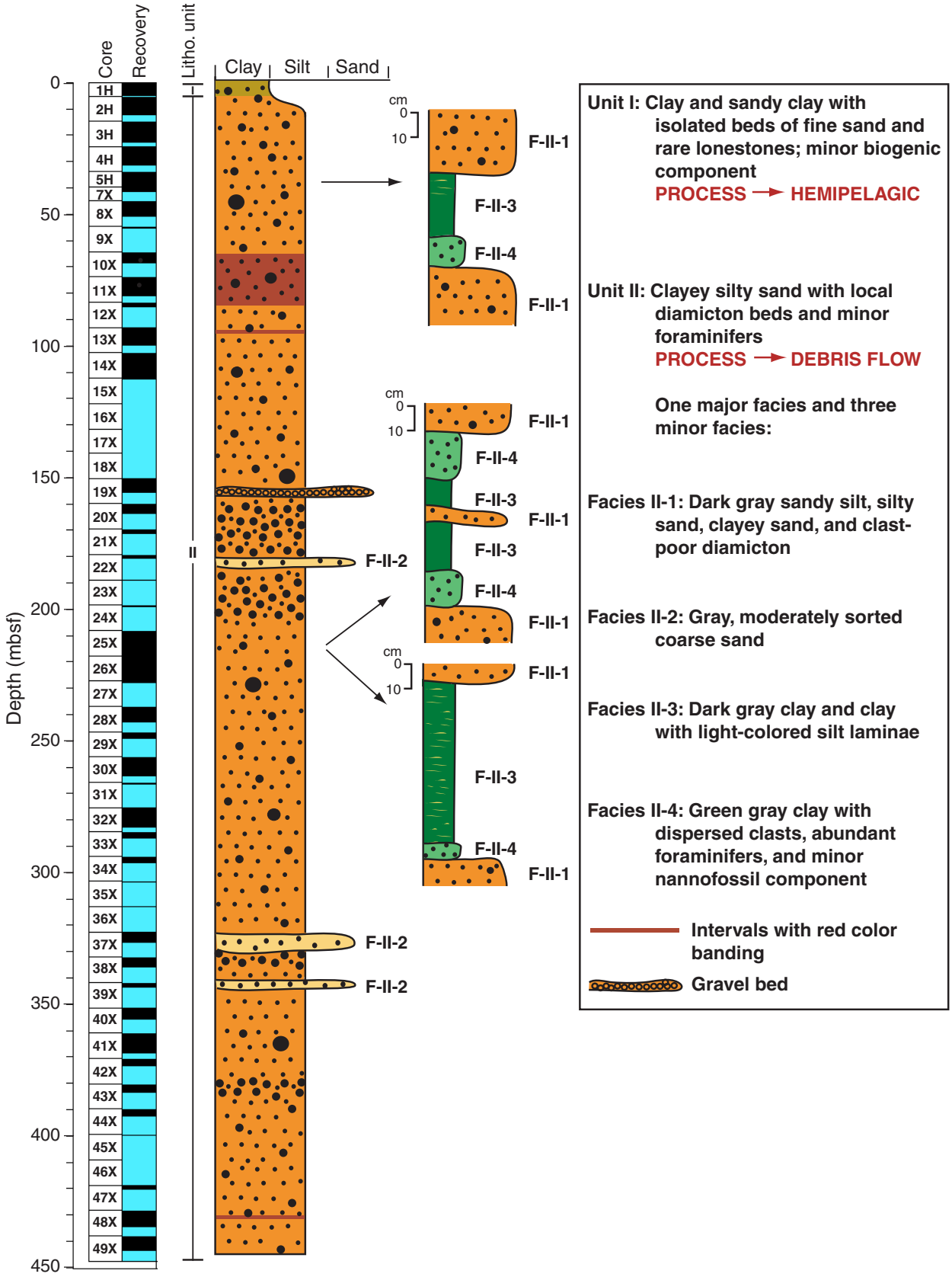

Figure F4. Composite stratigraphic section for Site 1167 showing core recovery, a simplified summary of lithology, lithologic unit boundaries, and age. Lithologic symbols are explained in Figure **F3,** p. 42, in the "Explanatory Notes" chapter. Also shown are lonestone distribution and average size, minerals identified by XRD, and color reflectance. XRD shows the percentage of most abundant minerals. See Figure **F12,** p. 41, in the "Leg Summary" chapter for lithology and mineral legends. This graph was plotted using the methods developed by Forsberg et al. (1999). The thin line in the color reflectance shows the percent reflectance downhole (L*). The thick line is a 200-point moving average. (**Figure shown on next page.**)

Figure F4 (continued). (Caption shown on previous page.)

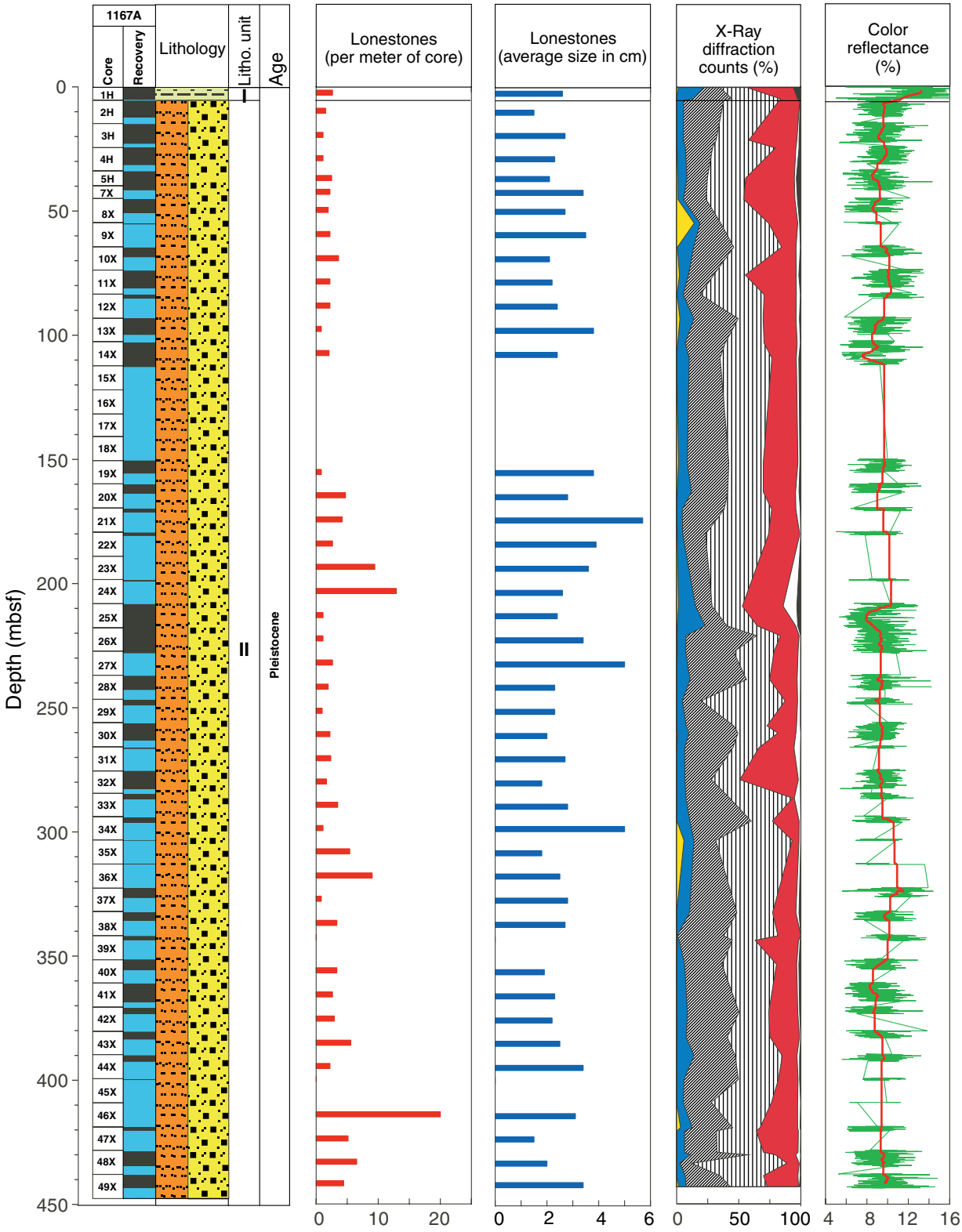

Figure F5. Clay and sandy clay typical of Unit I (interval 188-1167A-1H-2, 88–109 cm). Note the normal graded sand bed at 92–106 cm.

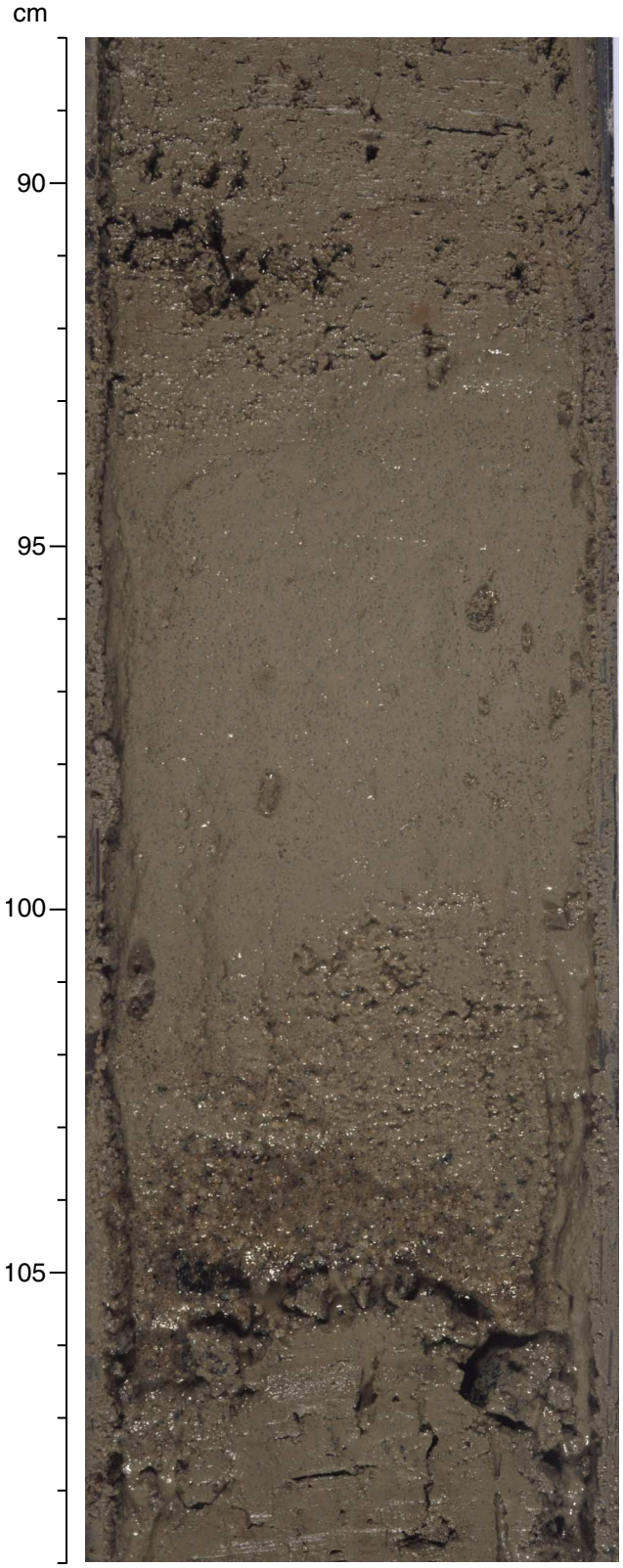

Figure F6. Silty sand with dispersed clasts typical of Facies II-1 (interval 188-1167A-5H-4, 45–65 cm).

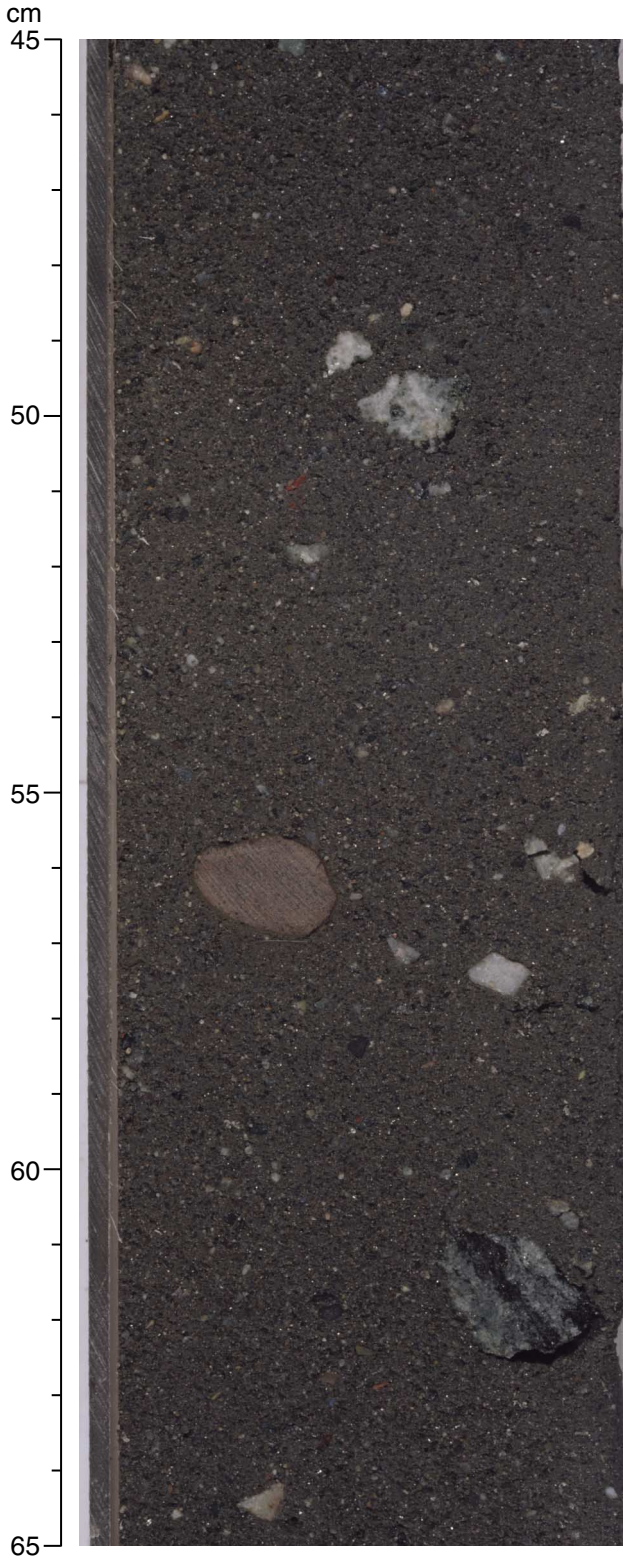

Figure F7. Lonestone lithologies and distribution in Hole 1167A.

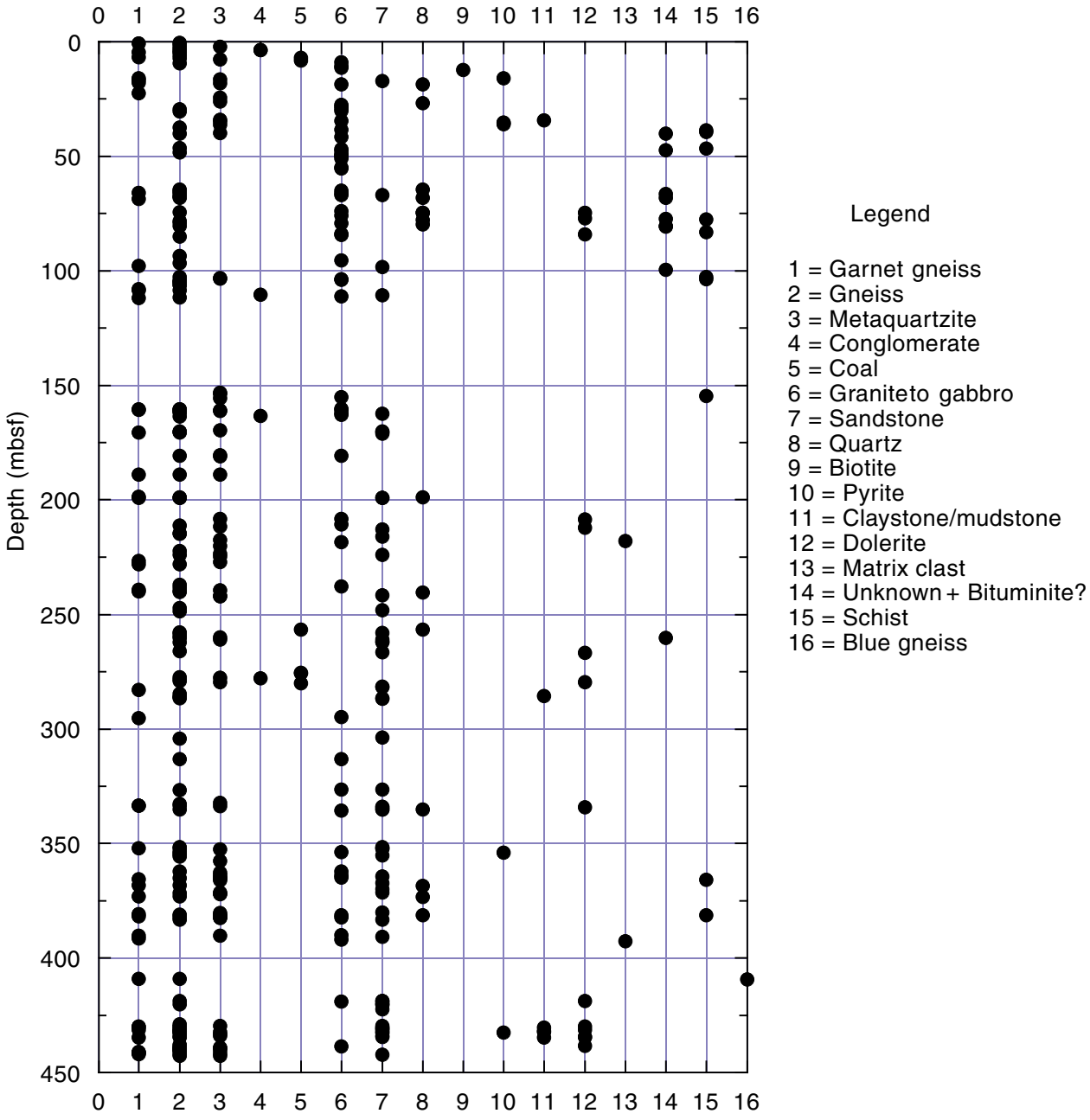

Figure F8. Distribution and frequency of sandstone vs. granite/igneous lonestones in Hole 1167A.

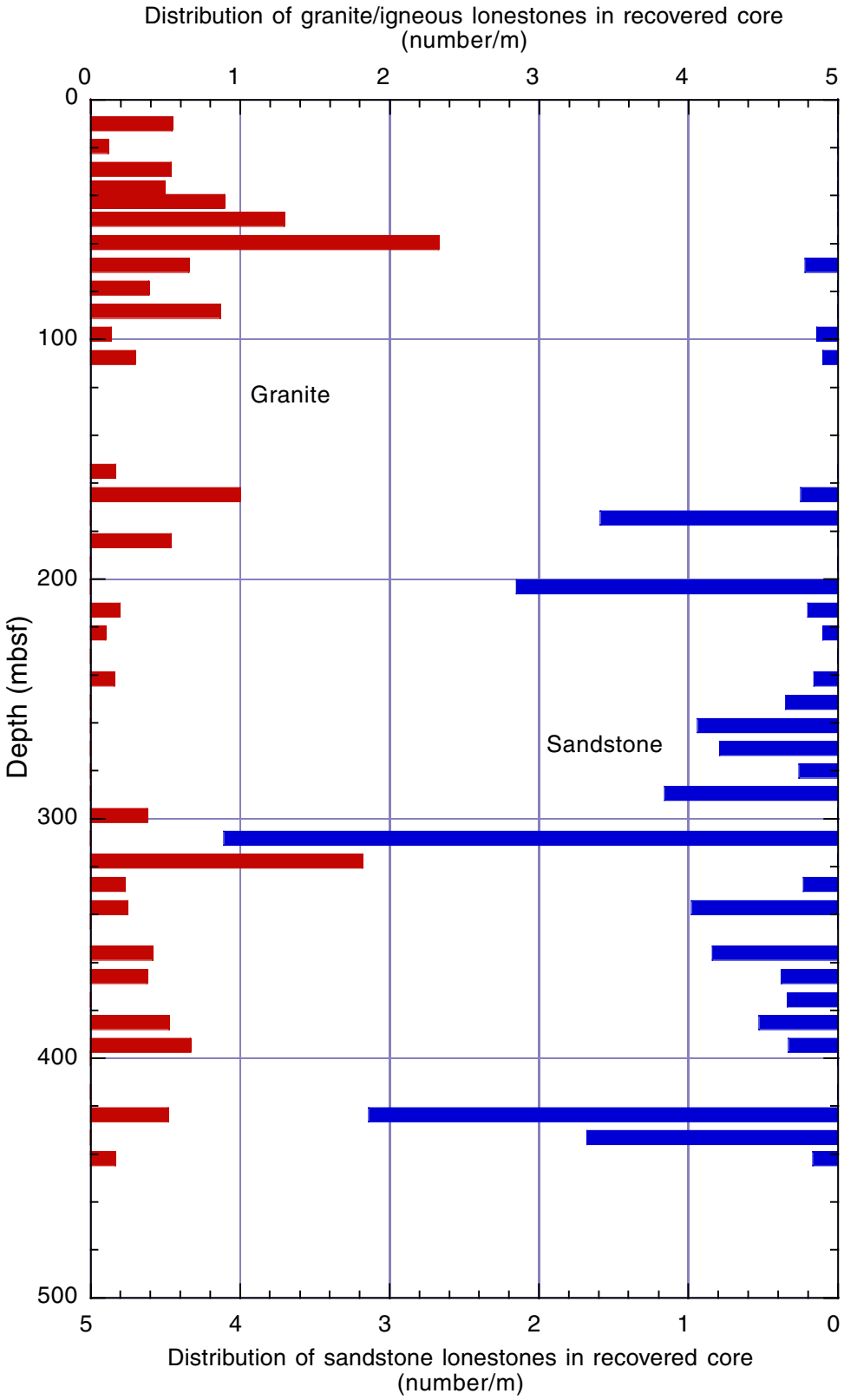

Figure F9. Gravel bed from Facies II-1 (interval 188-1167A-19X-2, 50–80 cm).

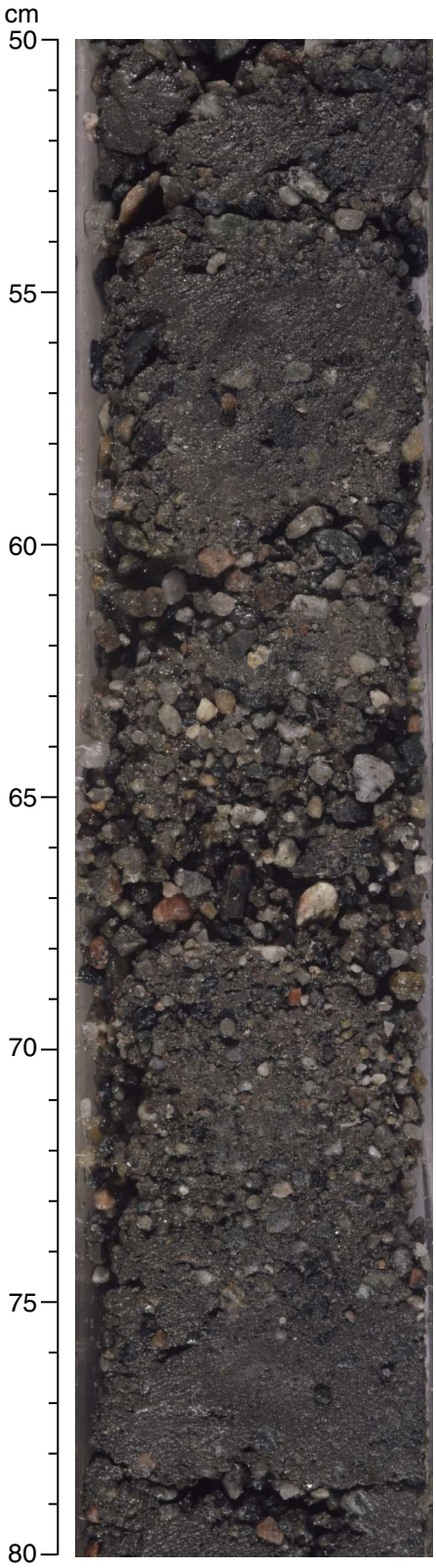

Figure F10. Example of dark gray and dark reddish gray color banding (interval 188-1167A-10X-2, 22–42 cm).

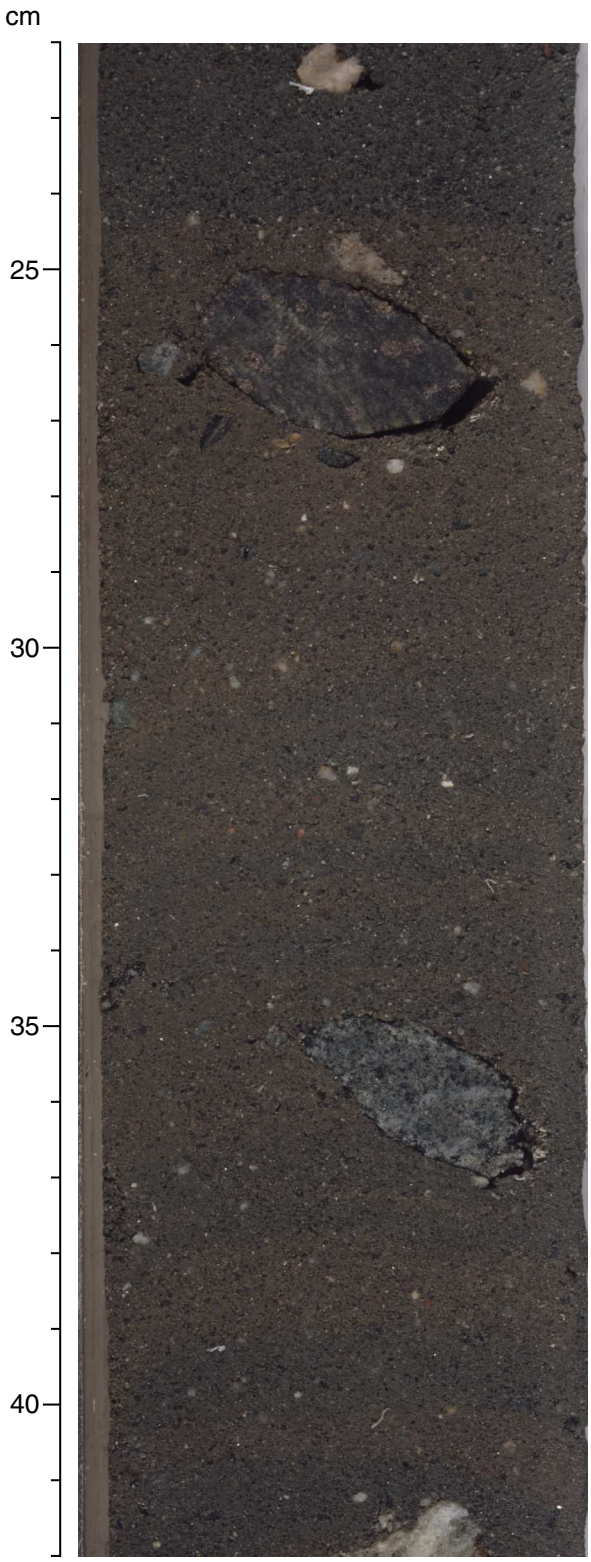

Figure F11. Facies II-2 coarse sand with dispersed mud clasts (interval 188-1167A-37X-3, 36–56 cm).

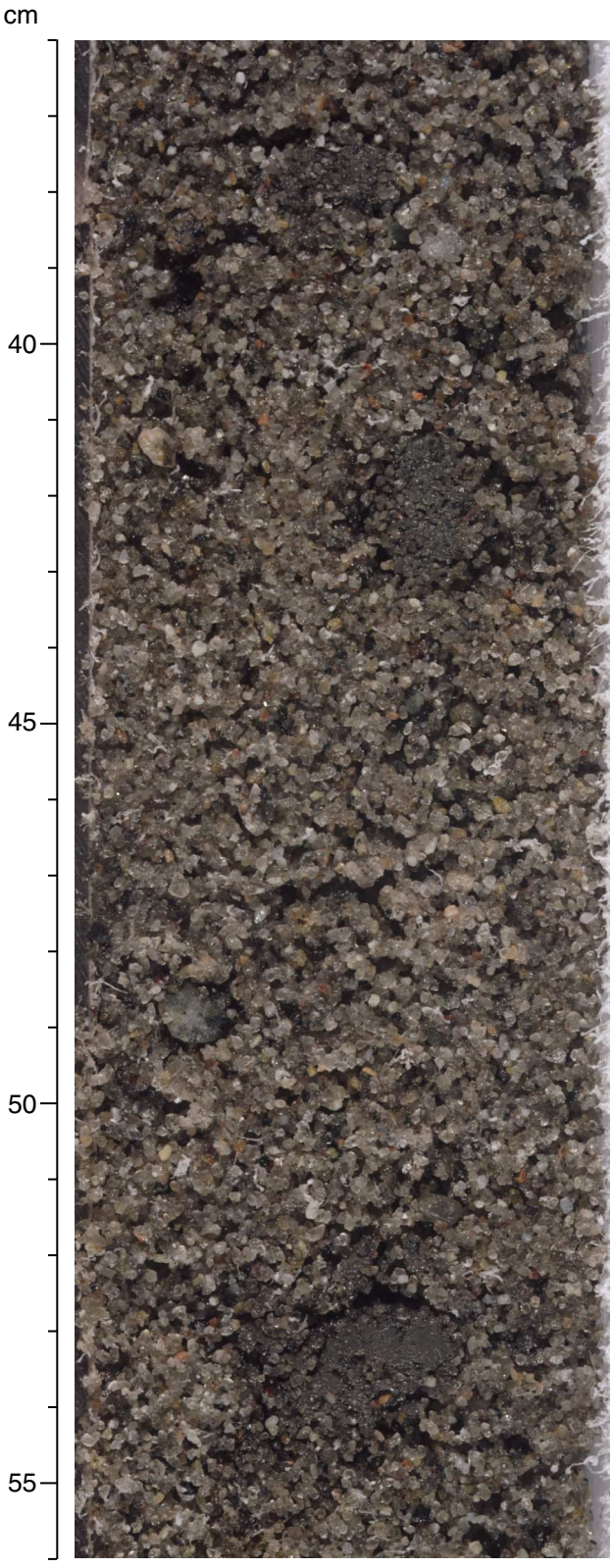

Figure F12. Facies II-3 clay with silt laminae (interval 188-1167A-25X-7, 0–25 cm). Note the cross-bedding of clays.

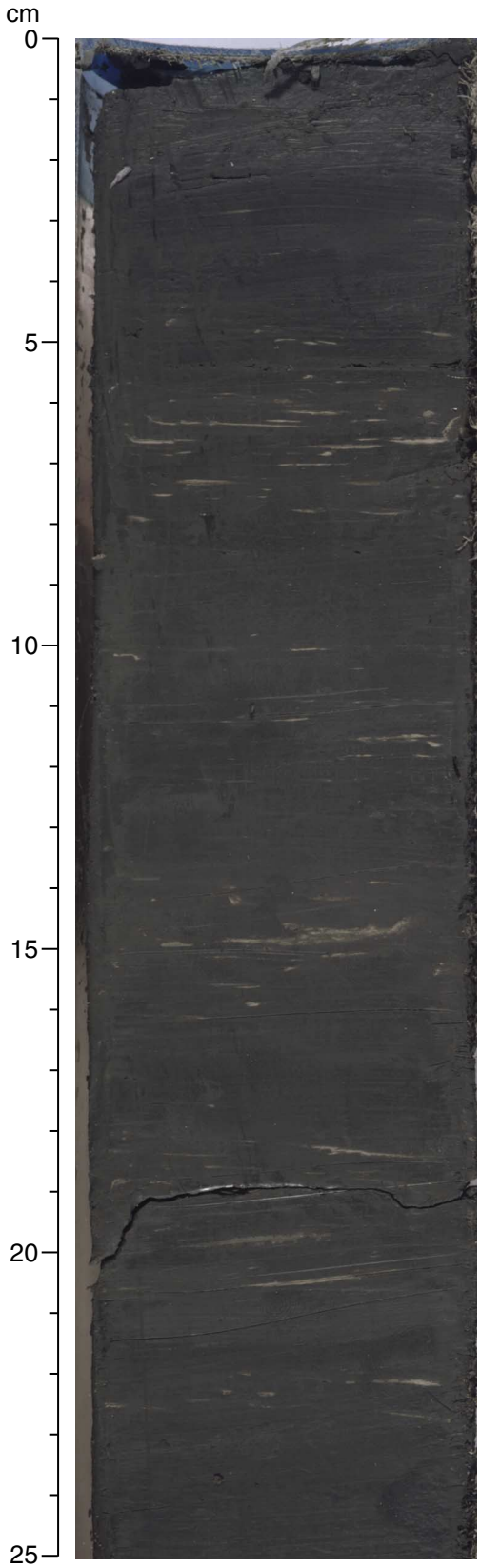

Figure F13. Sharp contacts at the top of Facies II-3 clay (interval 188-1167A-25X-6, 125–136 cm).

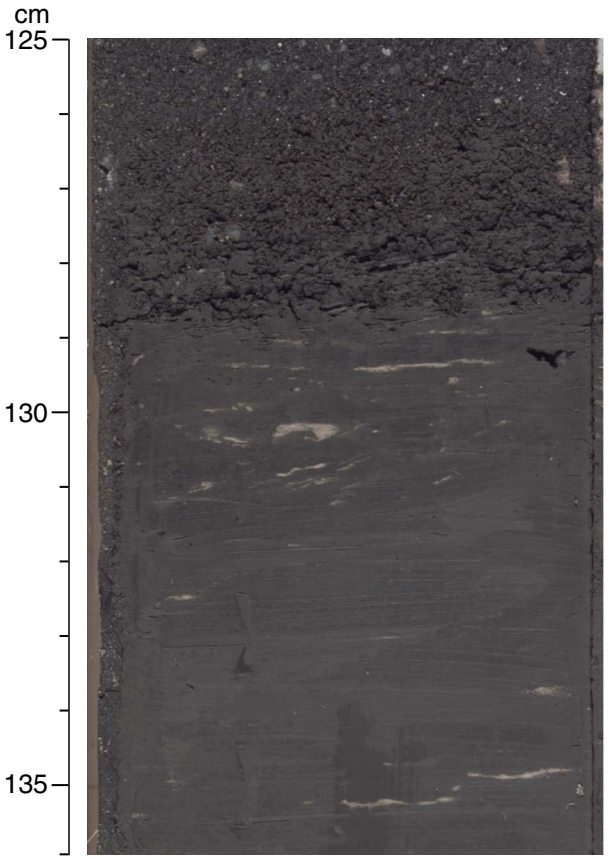

Figure F14. Sharp contact at the top and gradational contact at the base of Facies II-4 clay (interval 188-1167A-5H-3, 25–50 cm).

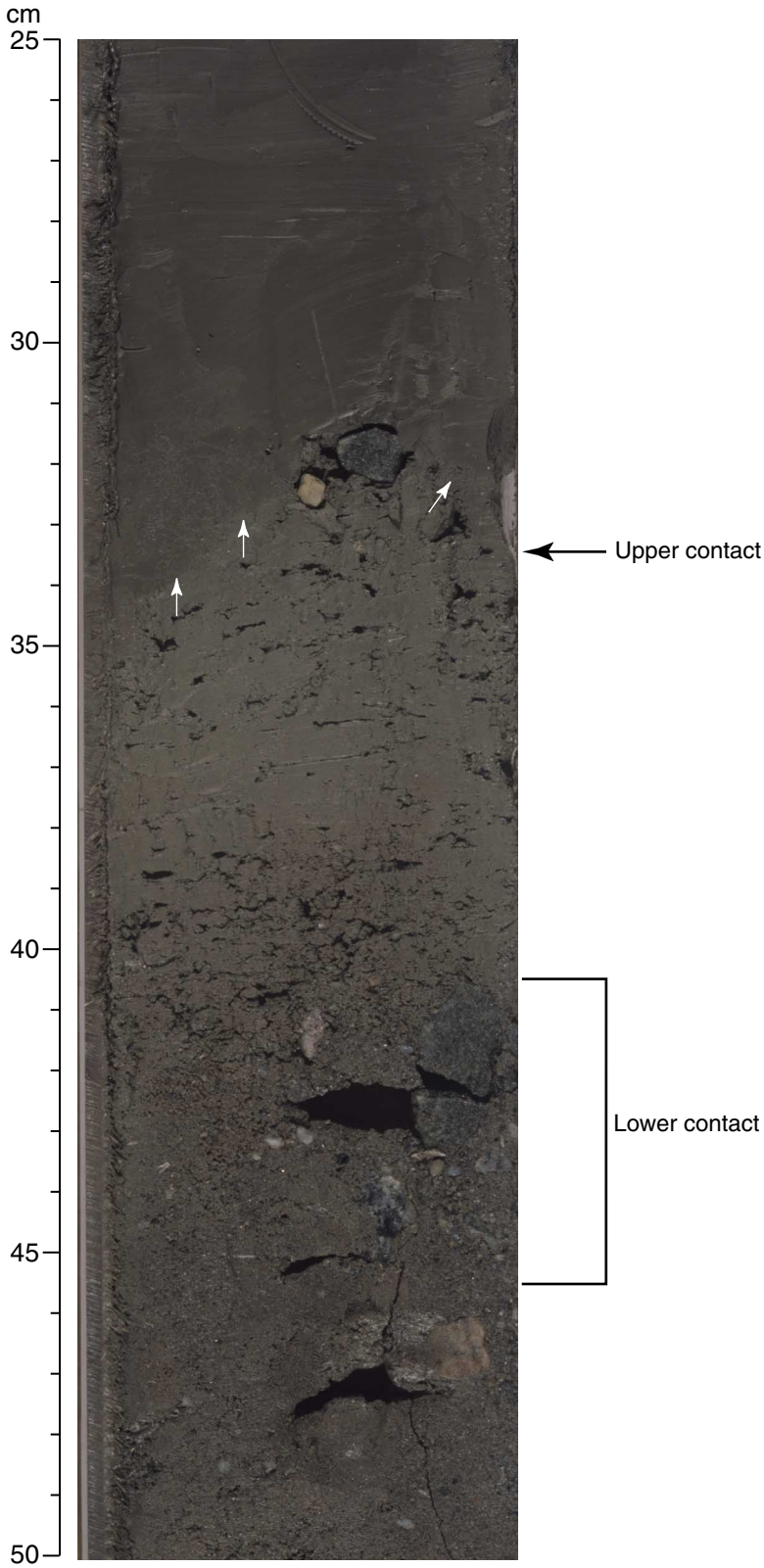

Figure F15. Typical succession of coarse- and fine-grained facies found in Core 188-1167A-5H (interval 188-1167A-5H-3, 7–50 cm) (also found in Core 188-1167A-25X).

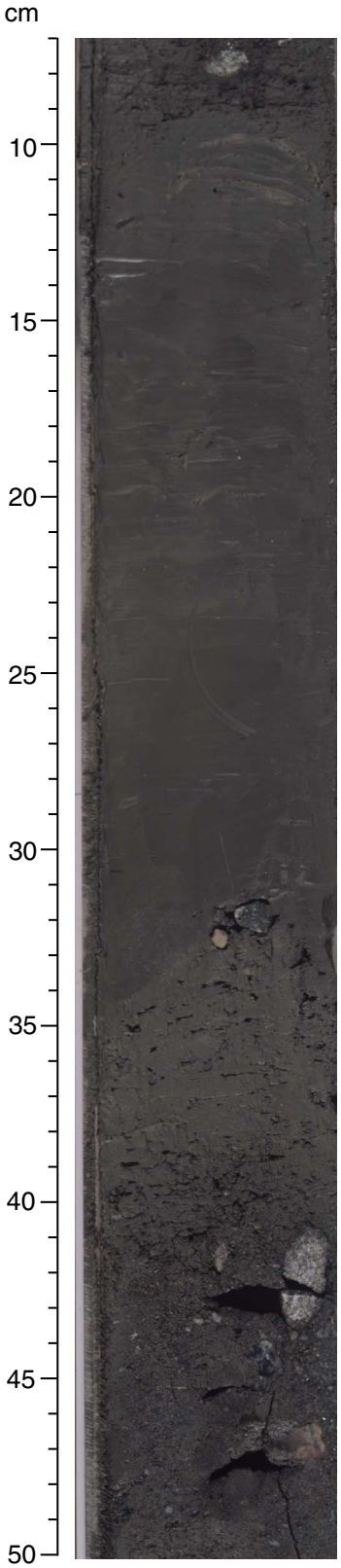

Figure F16. Percentages of sand, silt, and clay from Site 1167 smear slides.

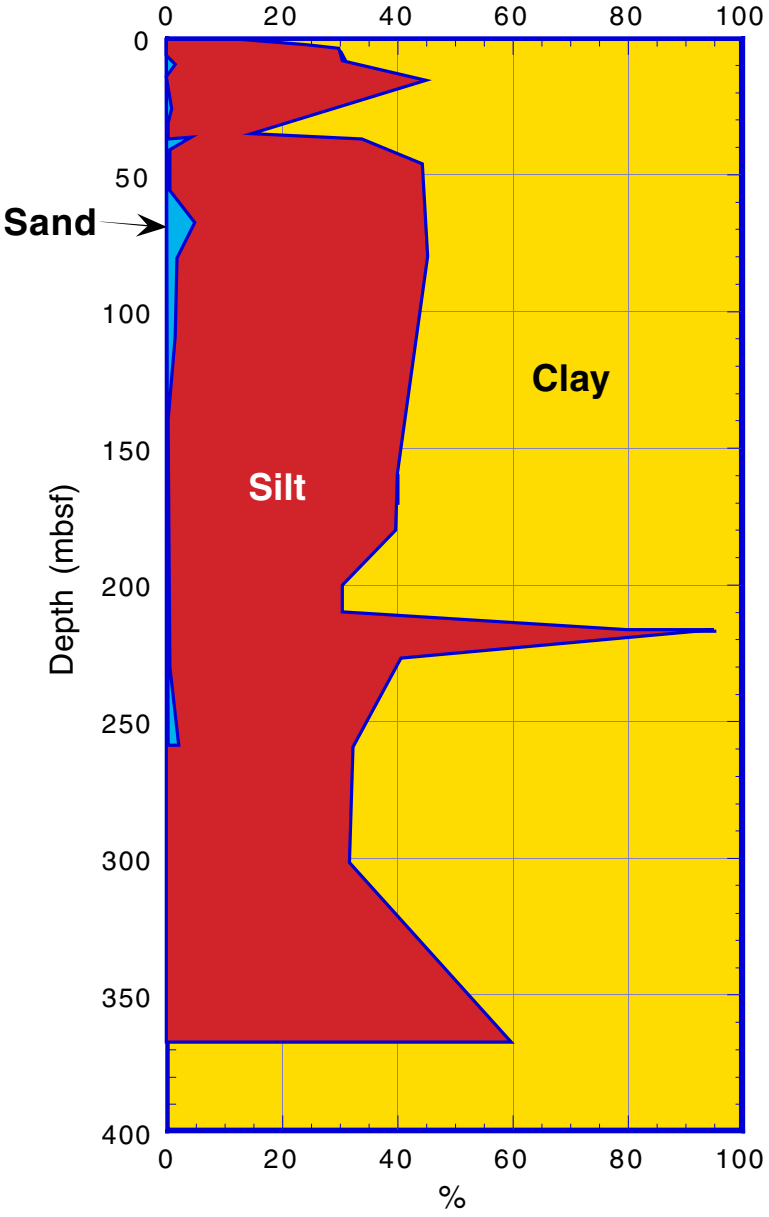

Figure F17. X-ray diffractograms of clay-sized fractions of sediment from Samples 188-1167A-1H-4, 45–46 cm, and 5X-3, 12–13 cm.

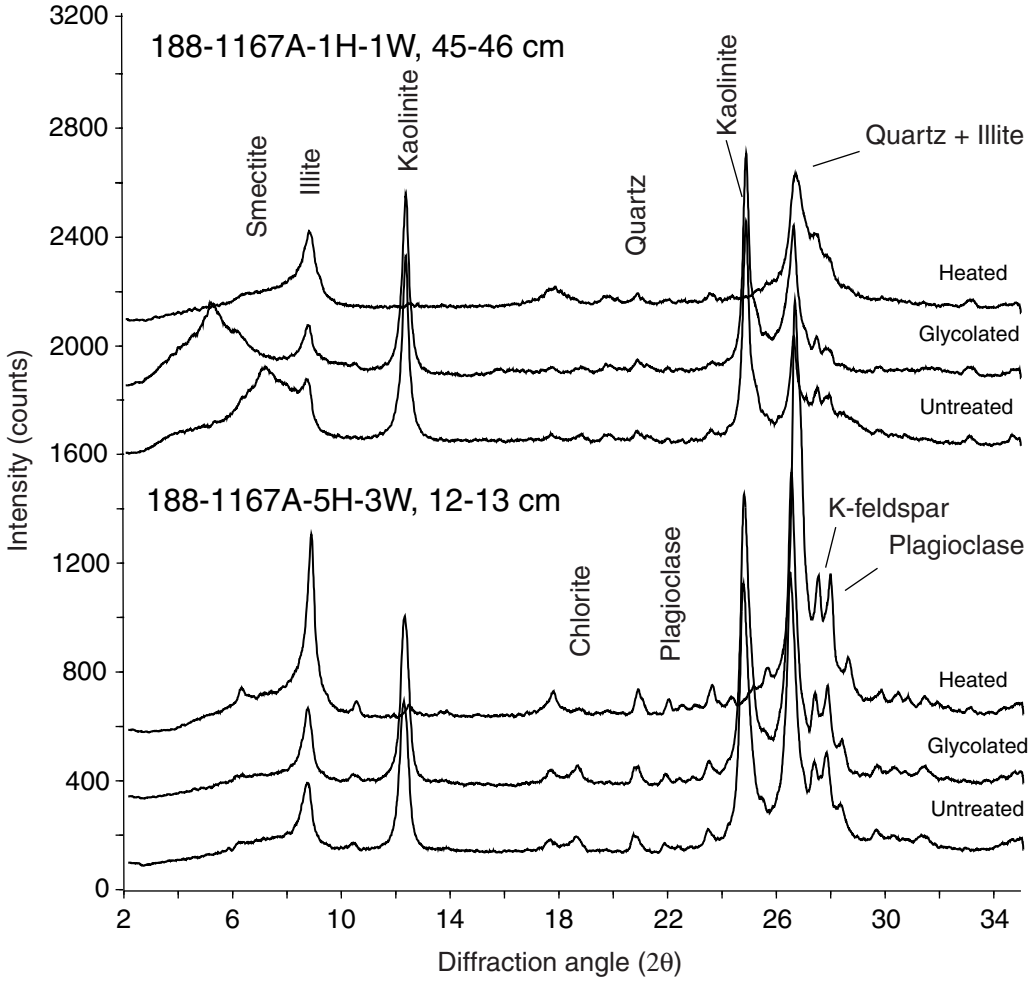

Figure F18. X-ray diffractograms of clay-sized fractions of sediment from Samples 188-1167A-25X-1, 126–127 cm, and 25X-7, 17–18 cm.

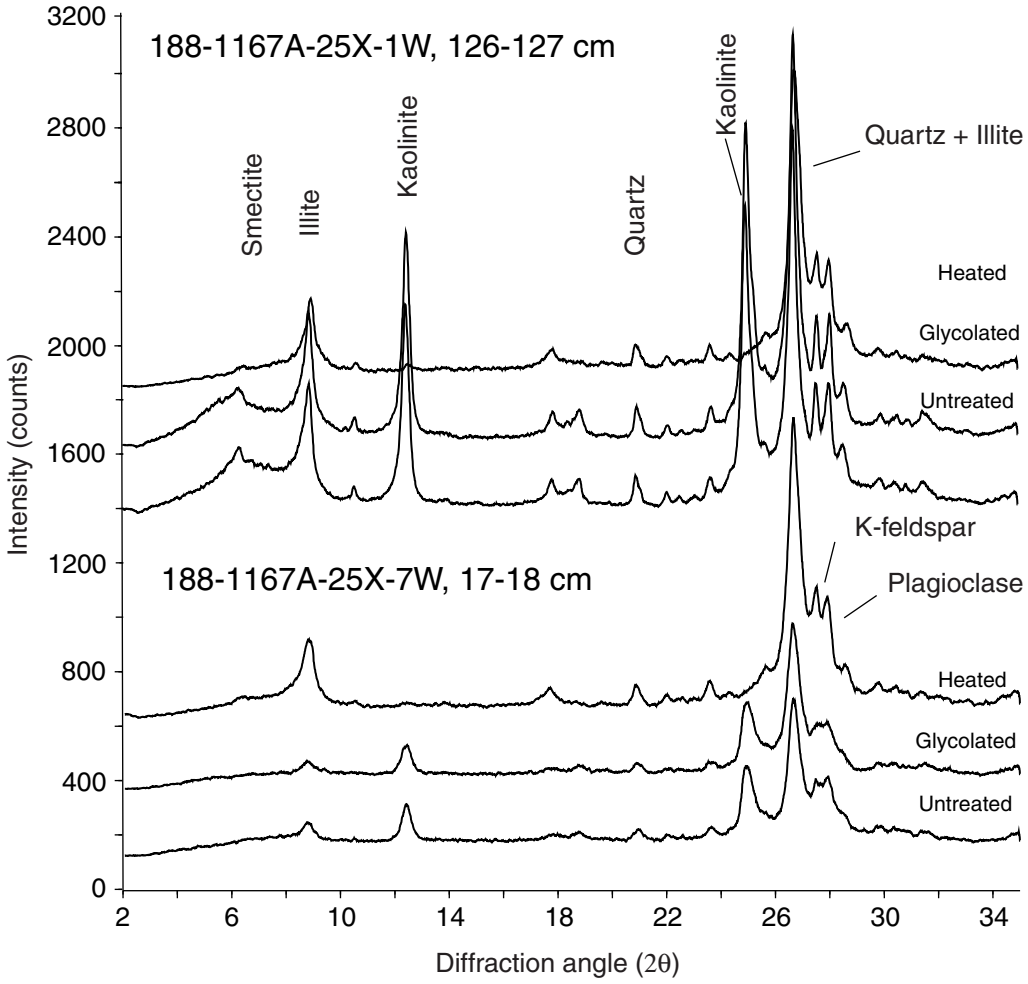

Figure F19. X-ray diffractograms of clay-sized fractions of sediment from Samples 188-1167A-10X-1, 31–32 cm; 14X-1, 68–69 cm; and 48X-1, 83–84 cm.

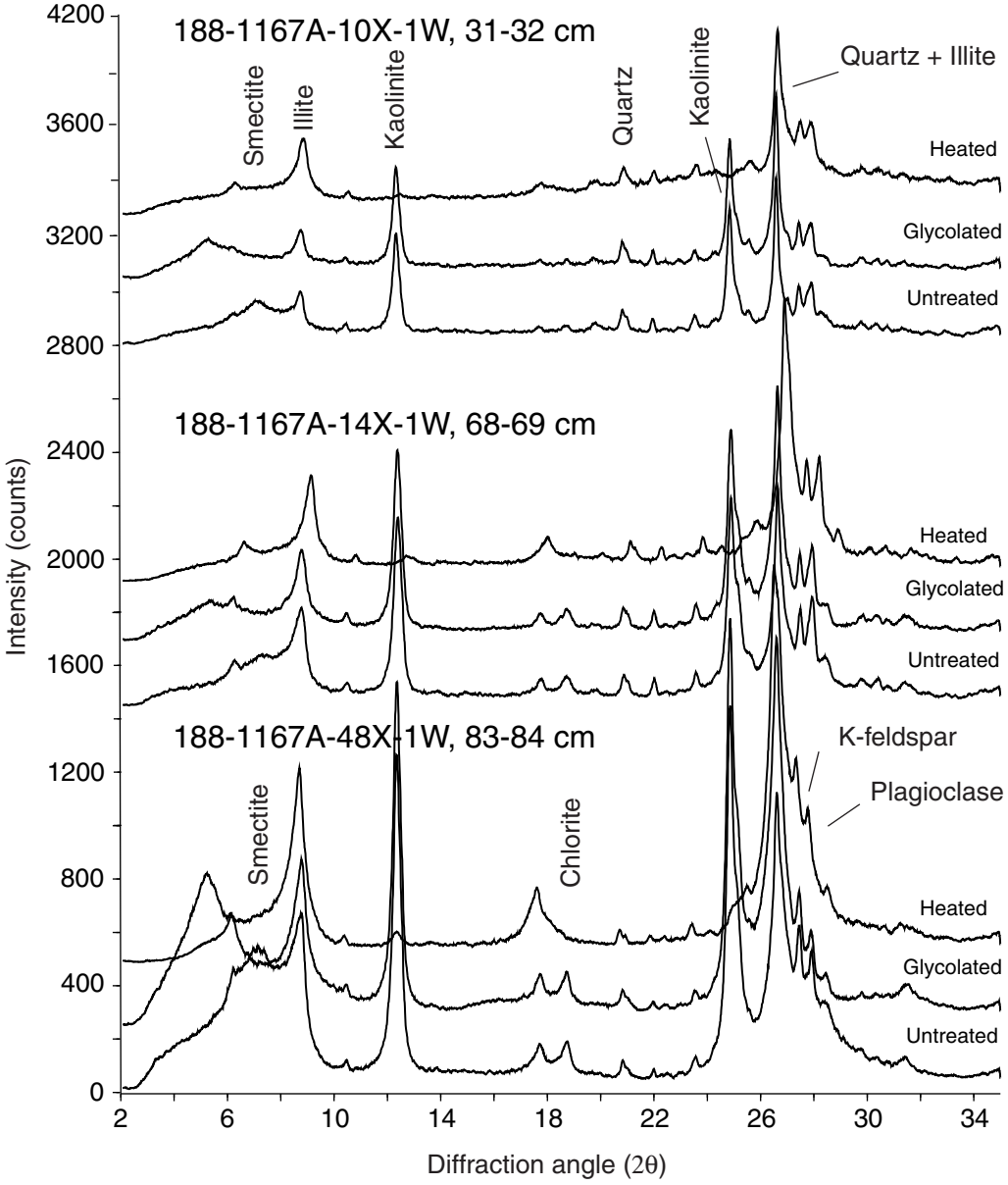

Figure F20. Graphical summary of core recovery, lithostratigraphic units, magnetostratigraphy, and biostratigraphic zones for Hole 1167A.

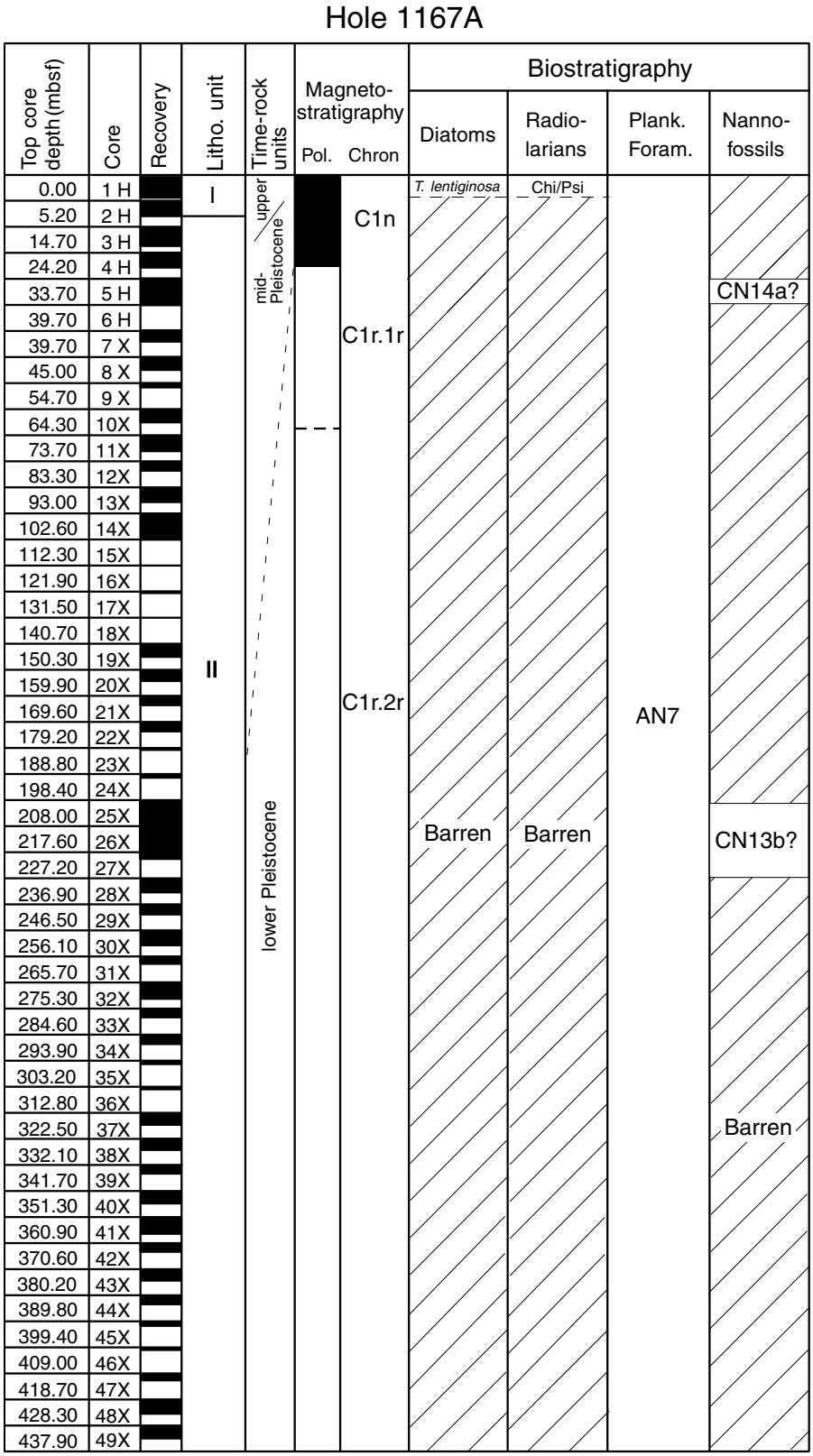

Figure F21. Downcore variation of concentration-dependent parameters (k, ARM, and IRM) at Site 1167. The horizontal solid lines indicate the boundaries between intervals with differing magnetic properties. ARM = anhysteretic remanent magnetization; IRM = isothermal remanent magnetization.

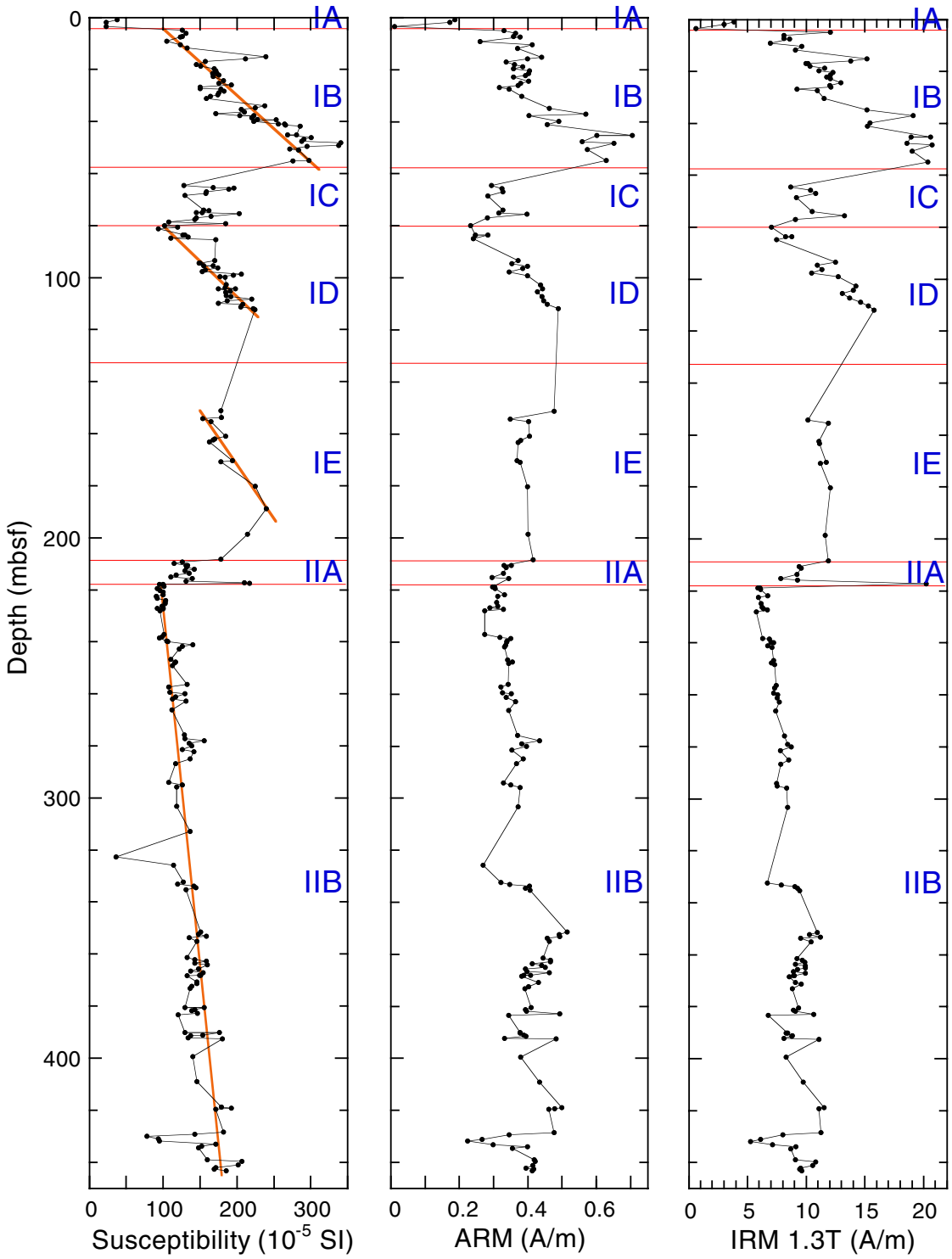

Figure F22. Plot of isothermal remanent magnetization (IRM) acquisition of 10 representative samples. Saturation of IRM is reached in fields of 0.2–0.3 T.

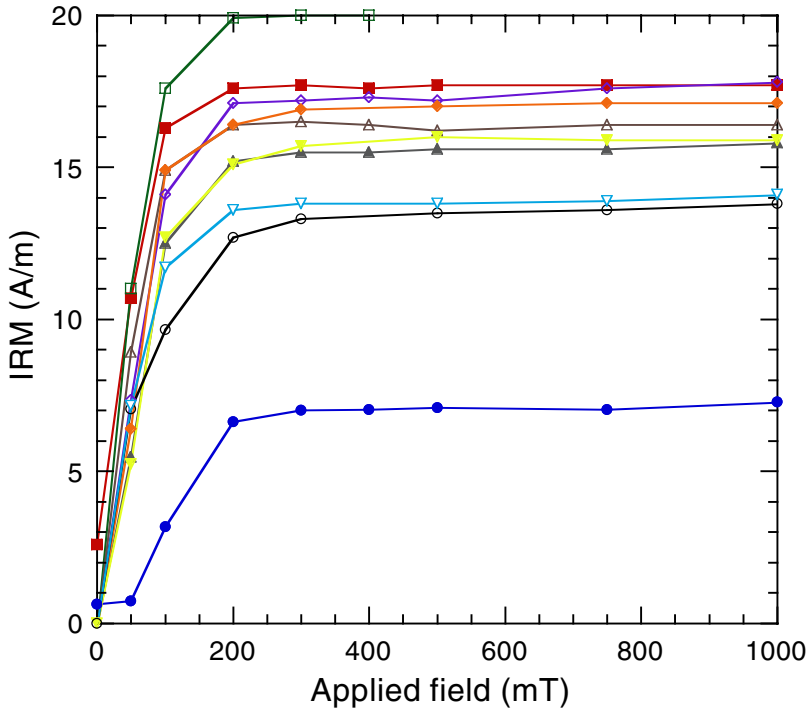

Figure F23. Downcore variation of ARM/IRM. The major boundary at ~217 mbsf is consistent with a shift from relatively coarse-grained magnetite (above) to relatively fine-grained magnetite (below). ARM = anhysteretic remanent magnetization; IRM = isothermal remanent magnetization.

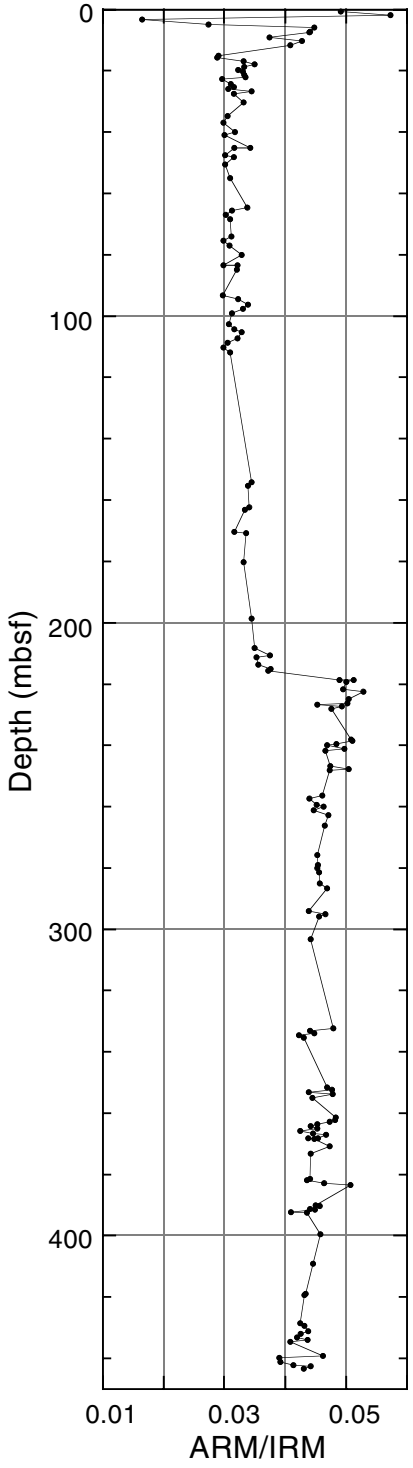

Figure F24. Vector component diagrams (with normalized intensity decay plots) of demagnetization (AF) behavior of four samples from Hole 1167A. Open symbols = projections onto the vertical plane; solid symbols = projections onto the horizontal plane. Numbers denote demagnetization levels in milliteslas and in degrees Celsius. Dashed lines = linear regression fits that indicate the characteristic remanence component for each sample. The stereoplots are equal-area projections, with open symbols indicating upper hemisphere projections and solid symbols indicating lower hemisphere projections. The core is not azimuthally oriented; therefore, the declination values are not meaningful. NRM = natural remanent magnetization. (**Figure shown on next page.**)

Figure F24 (continued). (Caption shown on previous page.)

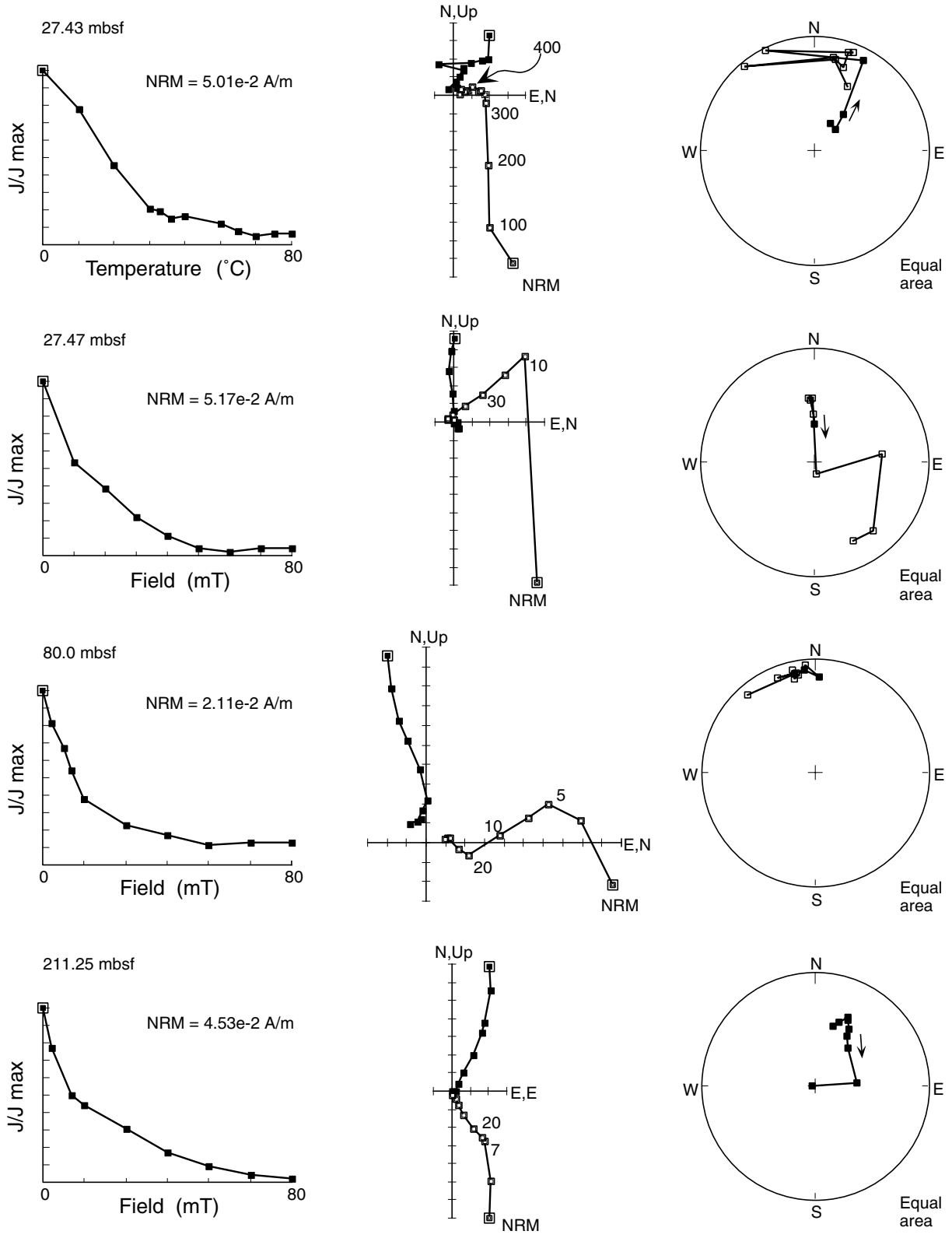

Figure F25. Magnetostratigraphic record from Hole 1167A. Plot of NRM intensity and inclination after demagnetization at 30 mT. The inclinations obtained from split cores (solid circles) are compared with inclinations from stepwise-demagnetized discrete samples (solid squares). Inclinations for discrete samples were determined by linear regression fits to multiple demagnetization steps. Polarity is shown on the log to the right. Black = normal polarity intervals; white = reversed polarity intervals. The depths of the two nannofossil assemblages are also indicated.

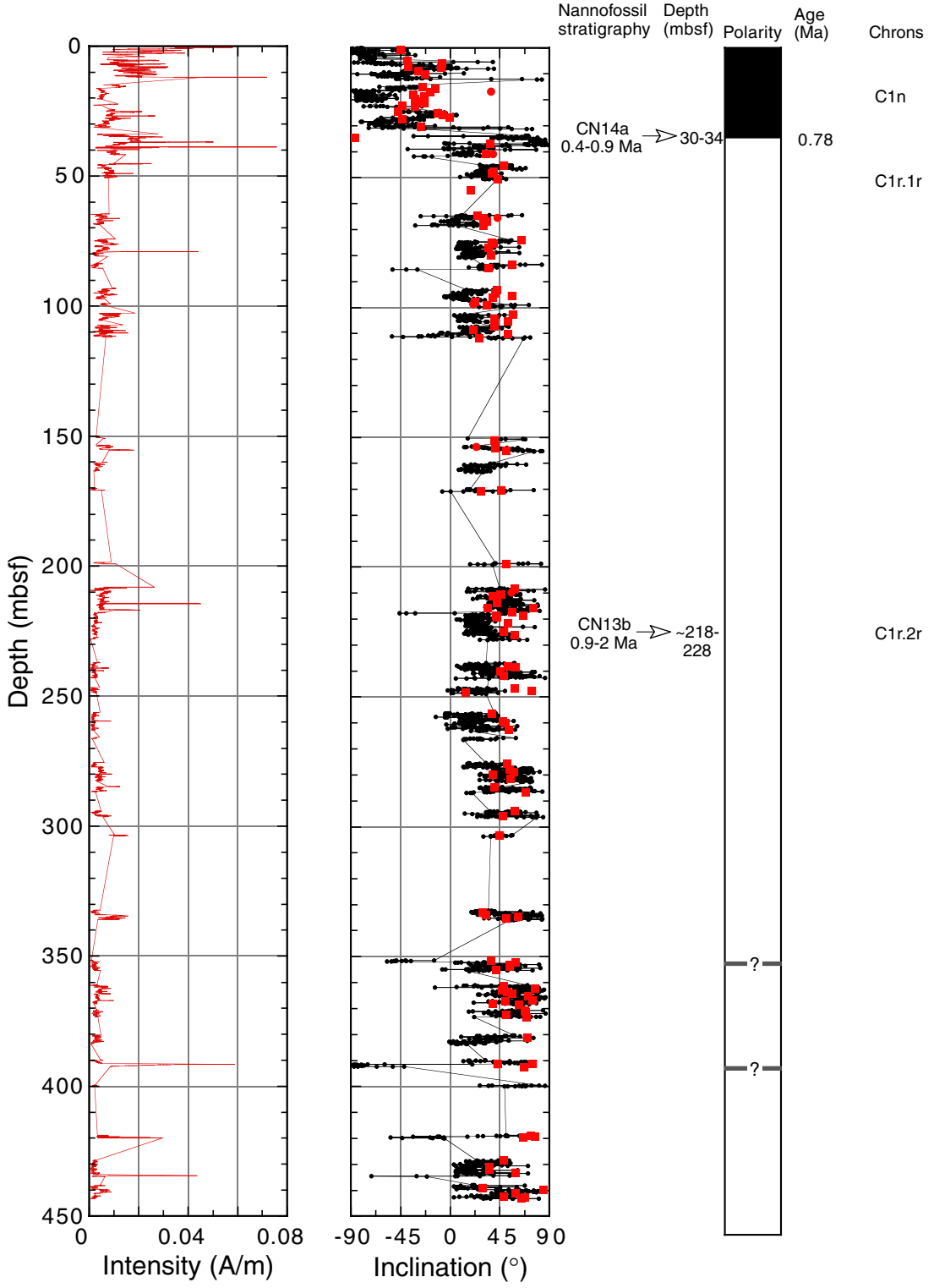

Figure F26. Interstitial water chemistry profiles vs. depth for salinity, chlorinity, pH, alkalinity, ammonium, phosphate, calcium (solid circles), magnesium (open circles), strontium, potassium, lithium, sodium, silica, manganese, and sulfate at Site 1167. Data are reported in Table T5, p. 89. (Continued on next page.)

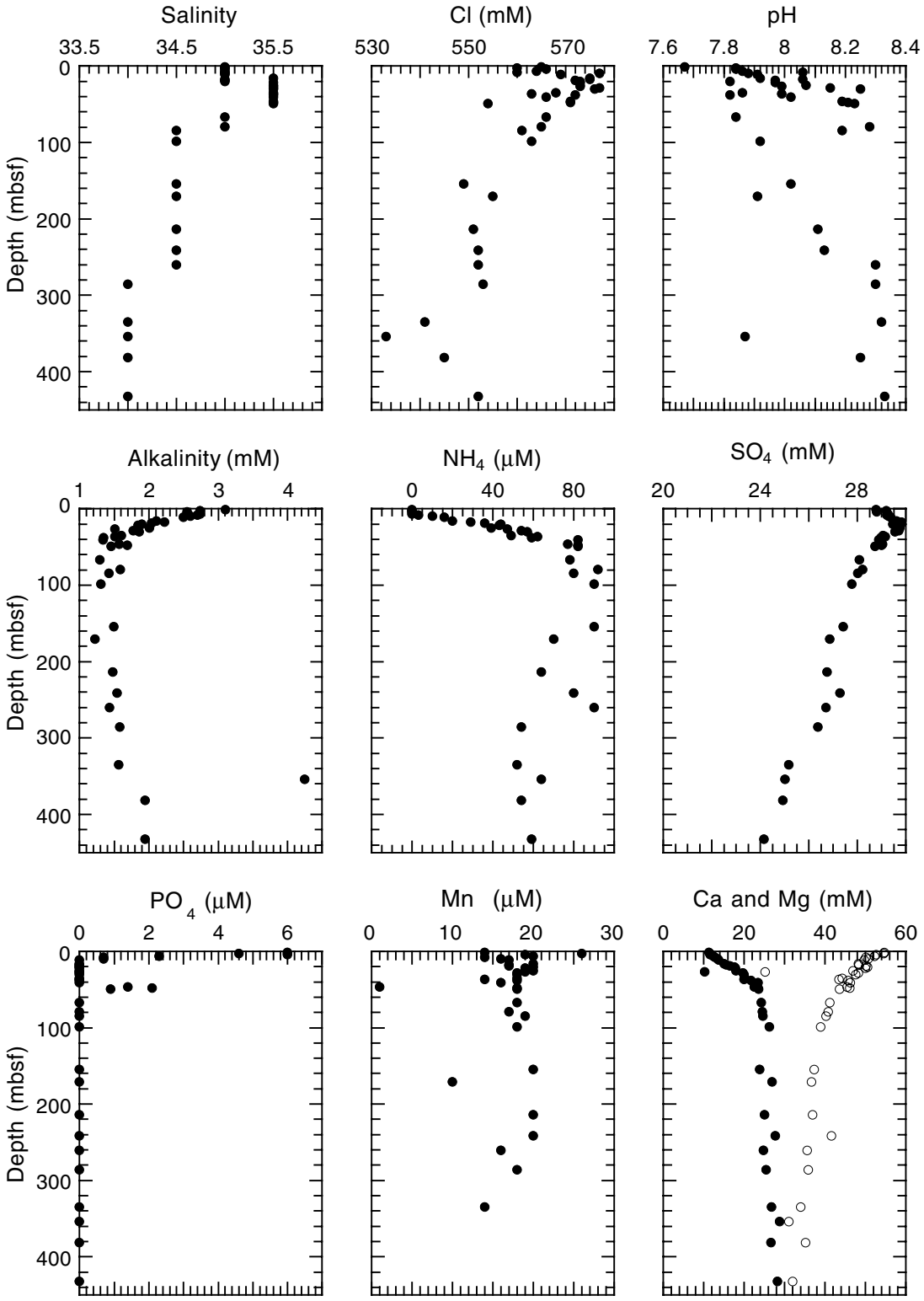

Figure F26 (continued).

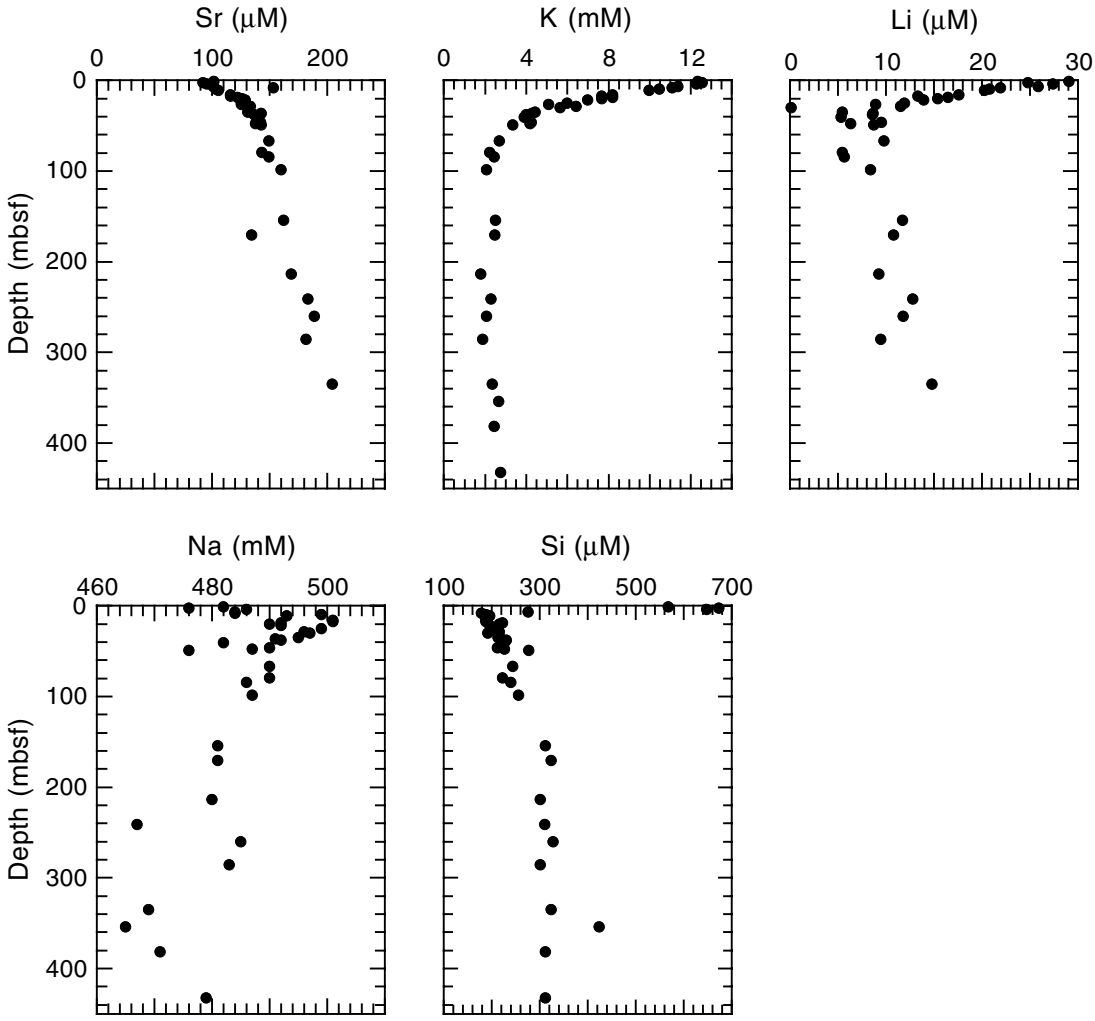

Figure F27. Weight percent of (**A**) inorganic carbon (calcium carbonate) and (**B**) organic carbon in sediments, Hole 1167A.

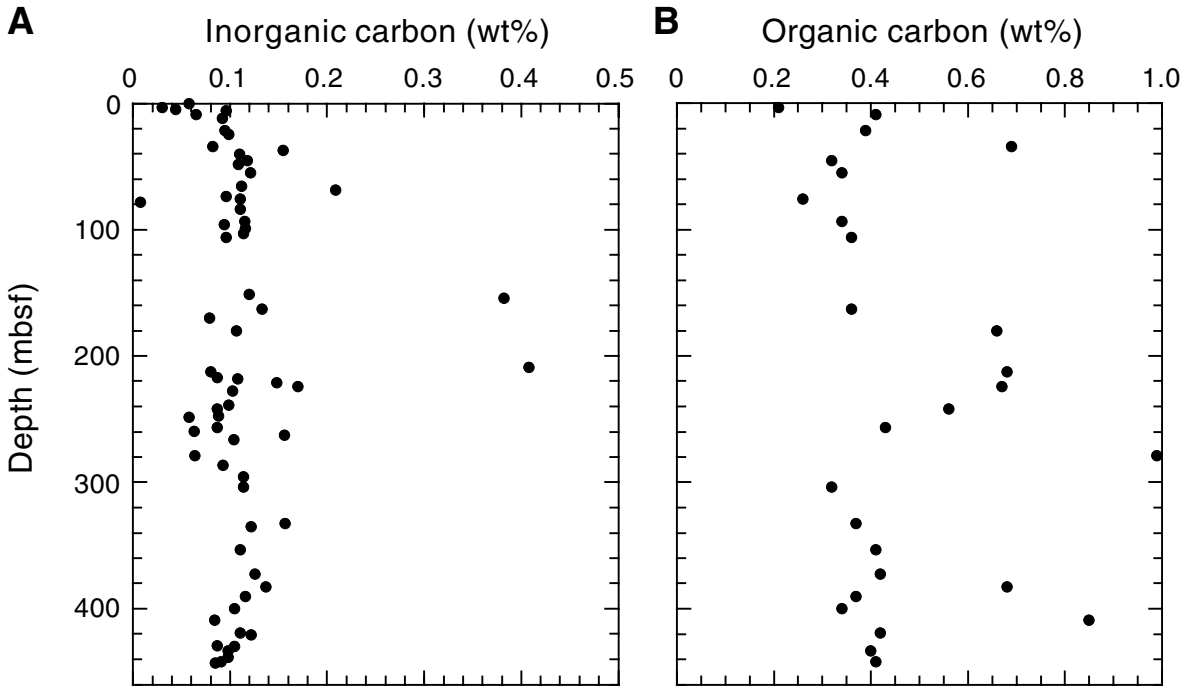

Figure F28. GRA bulk density, *P*-wave velocity, magnetic susceptibility, and NGR measured with the MST on APC cores from Hole 1167A. The column on the right shows lithostratigraphic units.

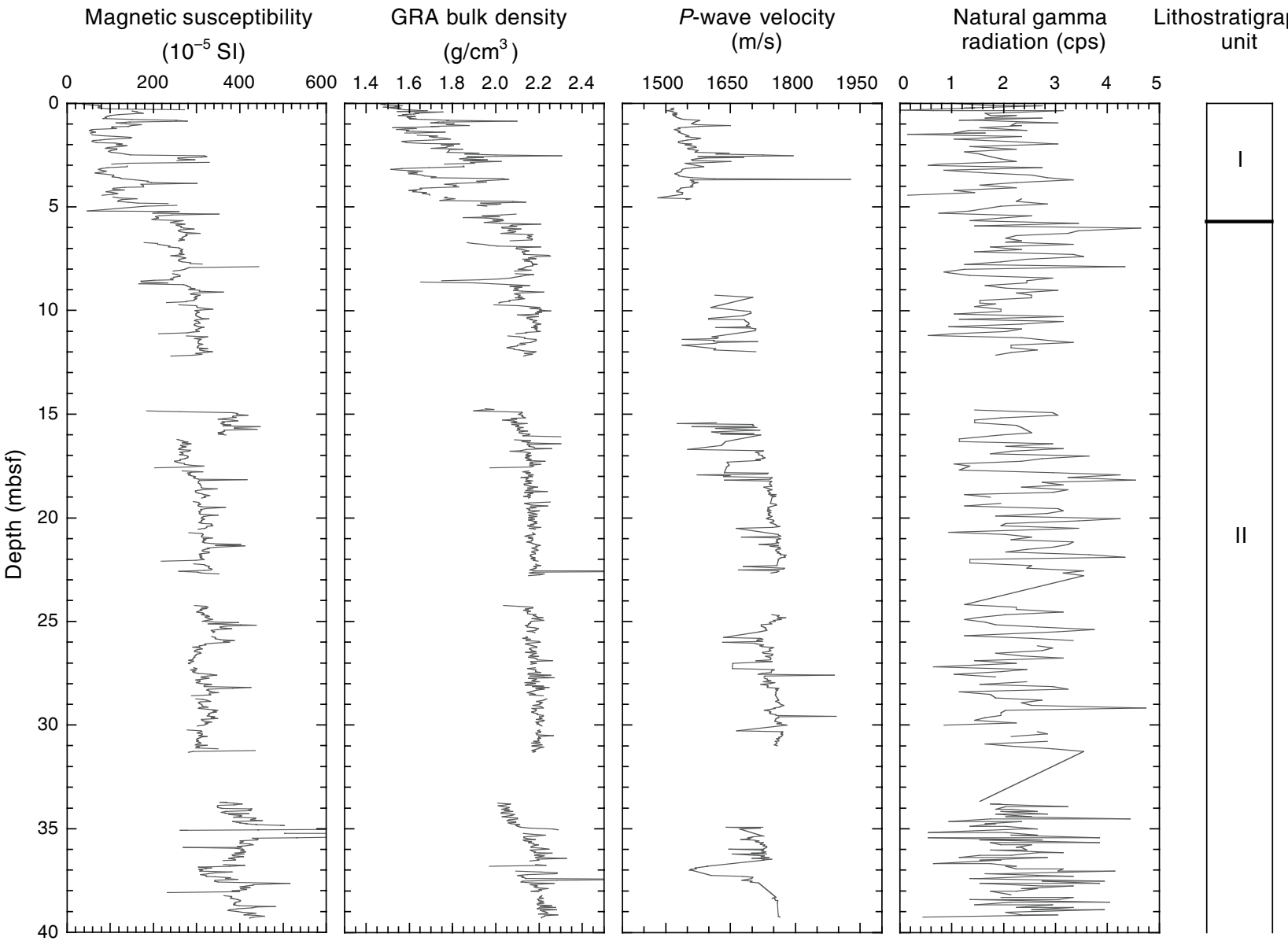

Figure F29. Plots showing bulk mineralogy from X-ray diffraction (XRD), NGR, and binned natural gamma spectra vs. depth at Site 1167. Core recovery and lithostratigraphic units are shown on the left. The line through the NGR data is a 20-m moving average. The binned NGR spectra show channels 100 through 248 (1.16–2.99 MeV) from the MST natural gamma detector. The characteristic peak positions of gamma radiation associated with potassium (K), uranium (U), and thorium (Th) are shown on the lowermost spectrum. (**Figure shown on next page.**)

Figure F29 (continued). (Caption shown on previous page.)

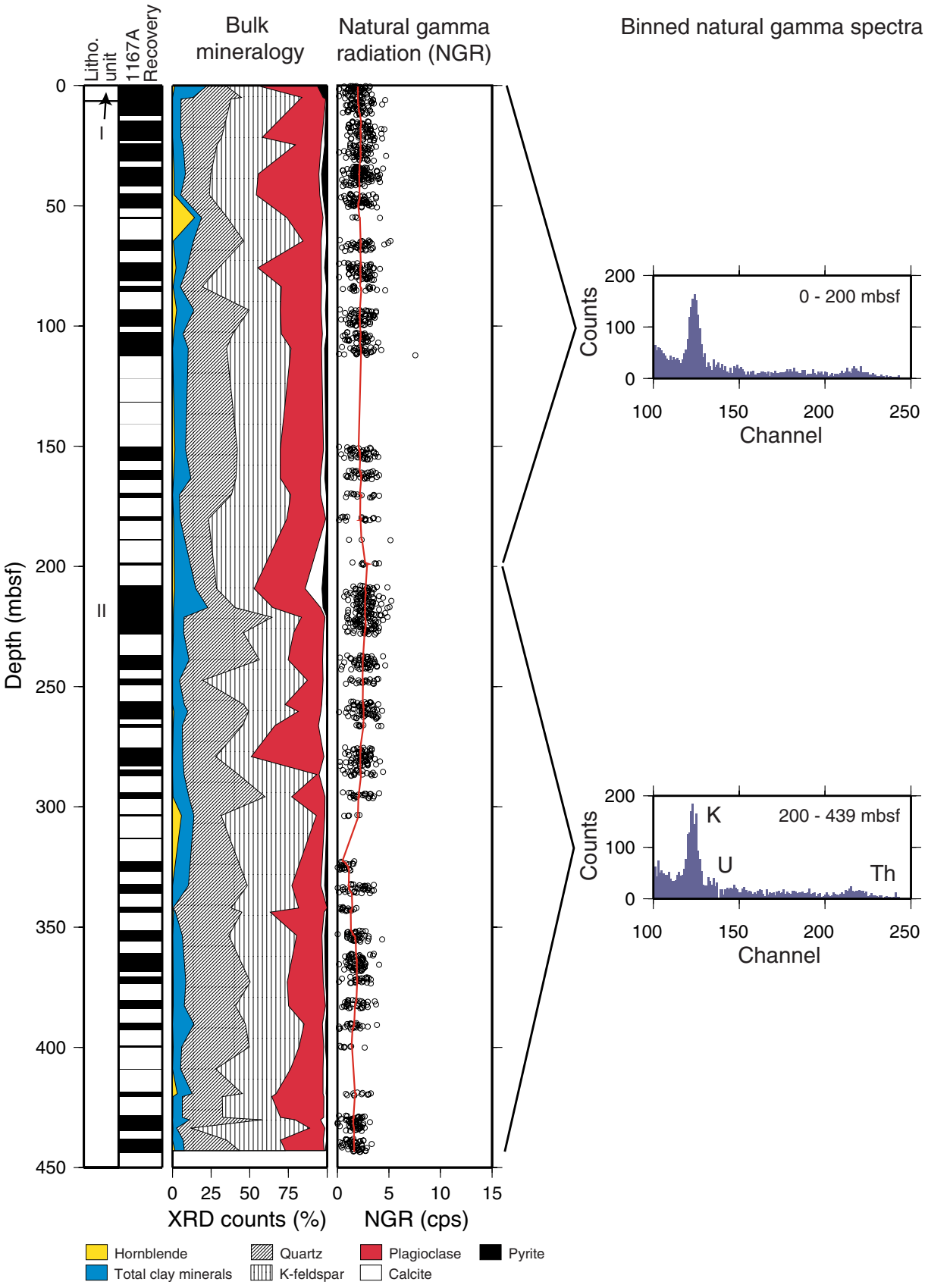

Figure F30. (A) Grain density and (B) porosity from discrete measurements. The inset detail of the data points around 210 mbsf shows the distinct decrease of porosity seen at that depth. The columns on the right show lithostratigraphic units and core recovery.

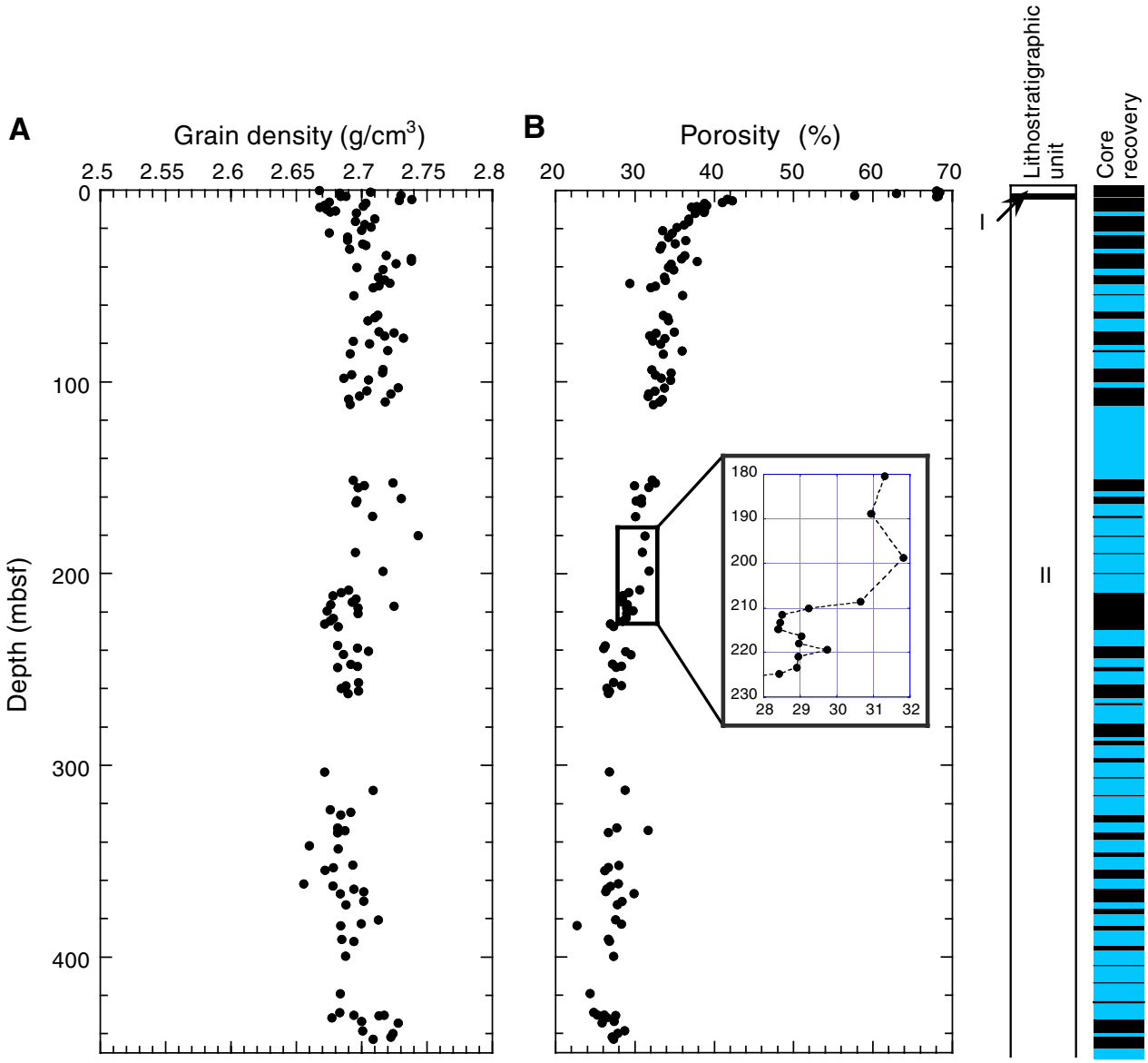

Figure F31. (**A**) Bulk density and (**B**) dry density from discrete measurements. Columns on the right show lithostratigraphic units and core recovery.

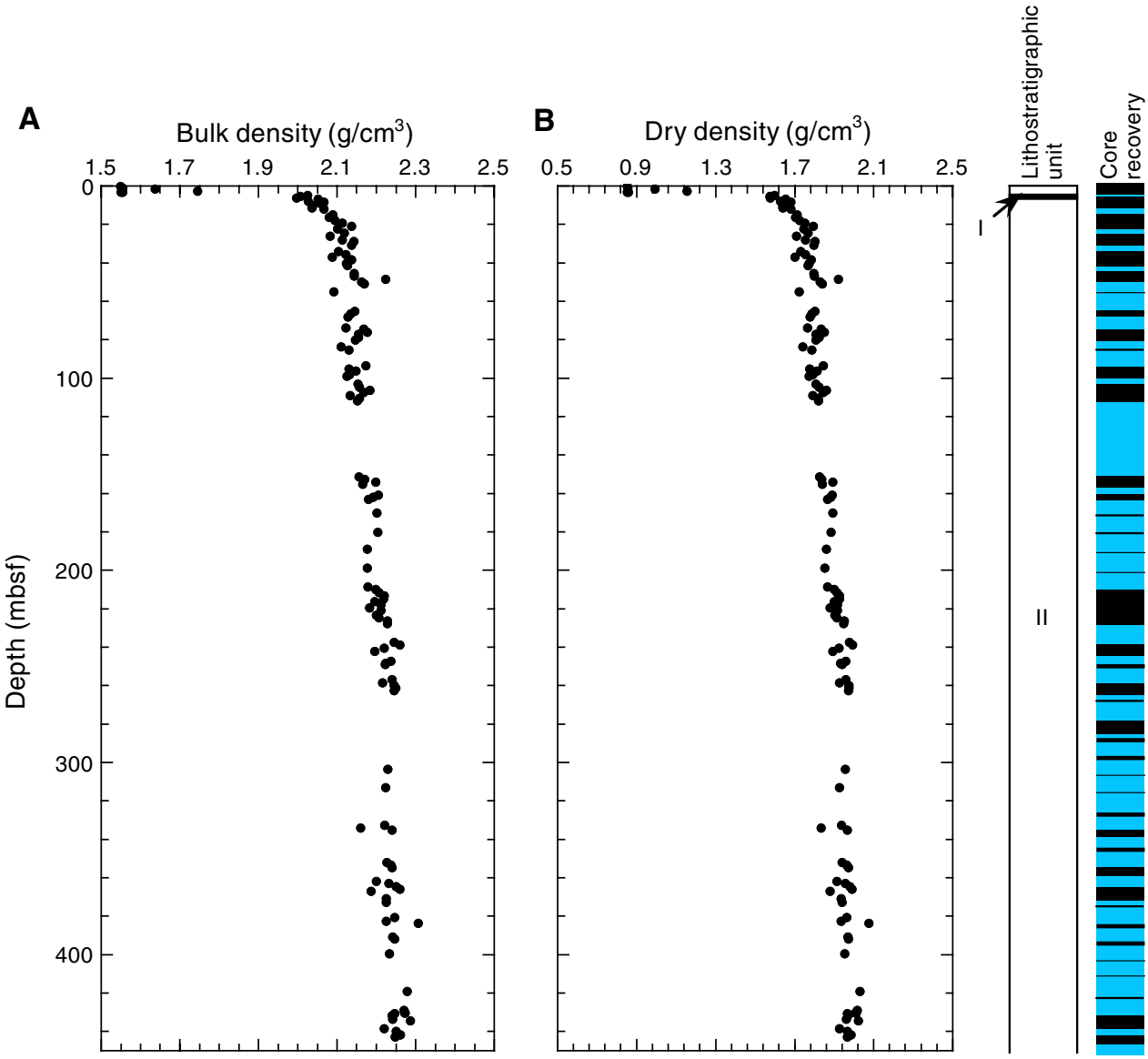

Figure F32. (**A**) Water content and (**B**) void ratio from discrete measurements. The inset detail of the data points around 210 mbsf shows the distinct decrease of void ratio seen at that depth. Columns on right show lithostratigraphic units and core recovery.

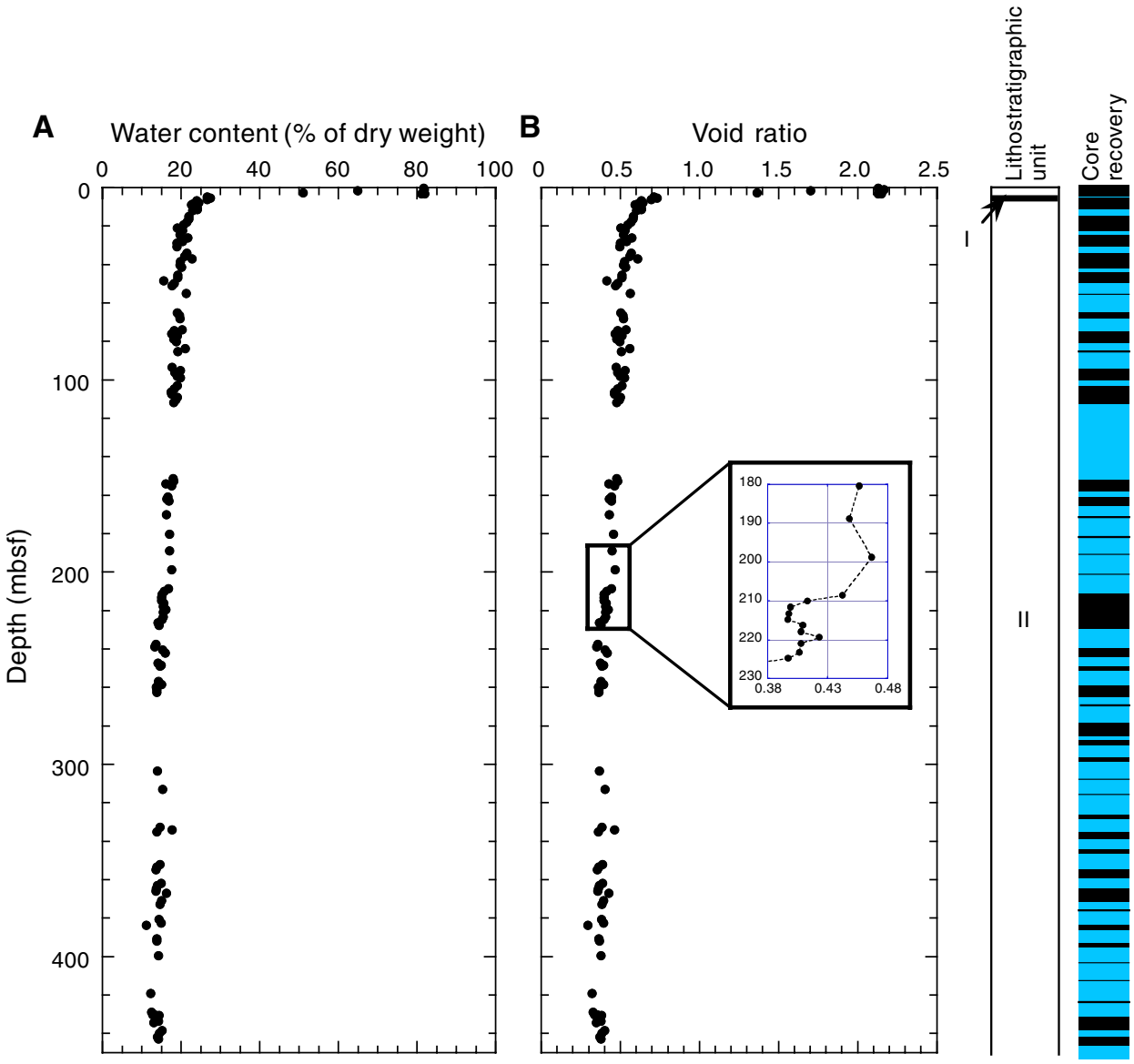

Figure F33. A. Comparison of gamma-ray attenuation (GRA) bulk-density data with bulk density from moisture and density (MAD) measurements. **B.** Ratio of MAD measurement of bulk density to bulk density from GRA measurements. The columns on the right show lithostratigraphic units and core recovery. APC = advanced hydraulic piston corer; XCB = extended core barrel.

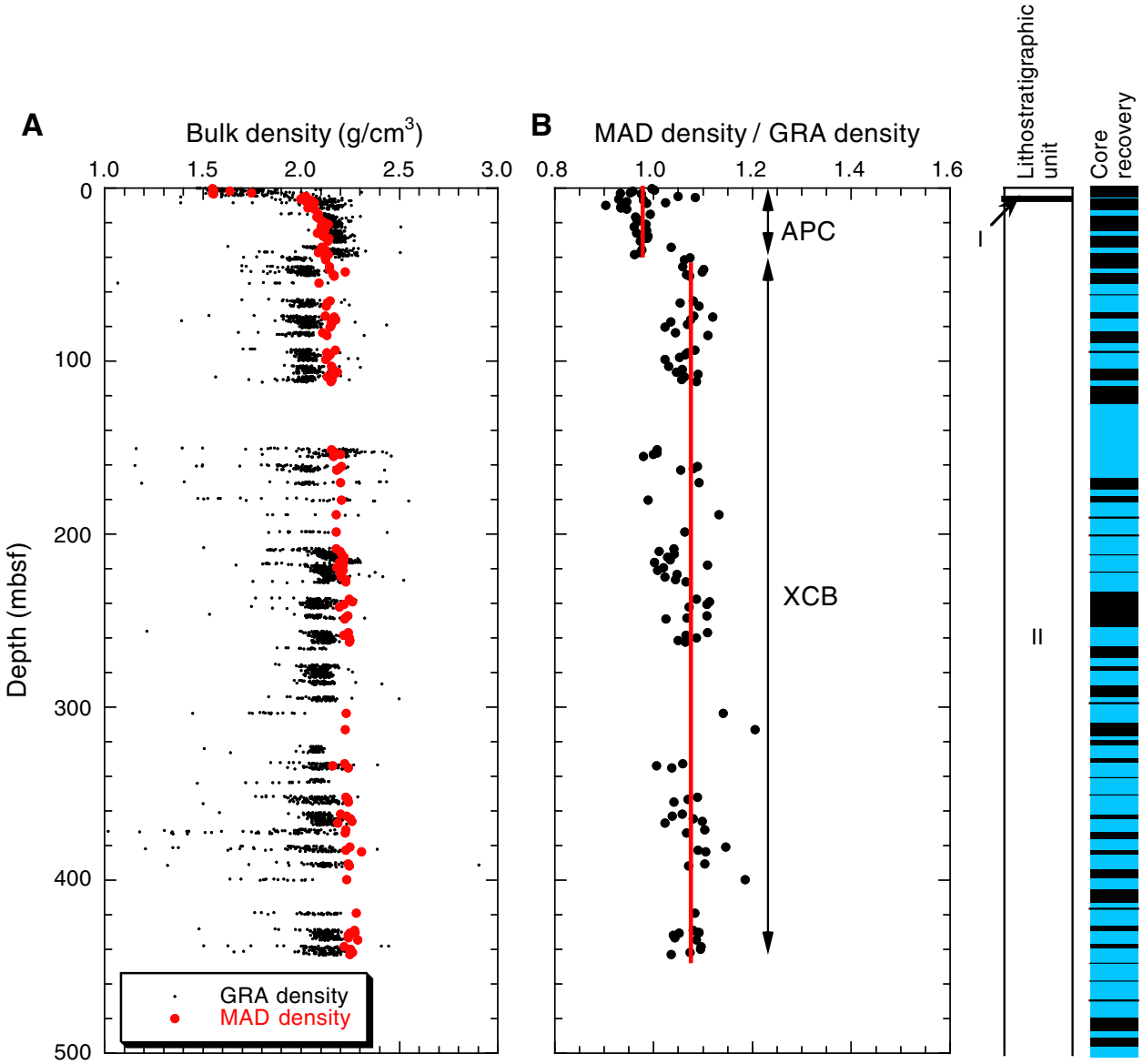

Figure F34. Discrete velocity measurements obtained with the PWS at Site 1167. The column on the right shows lithostratigraphic units.

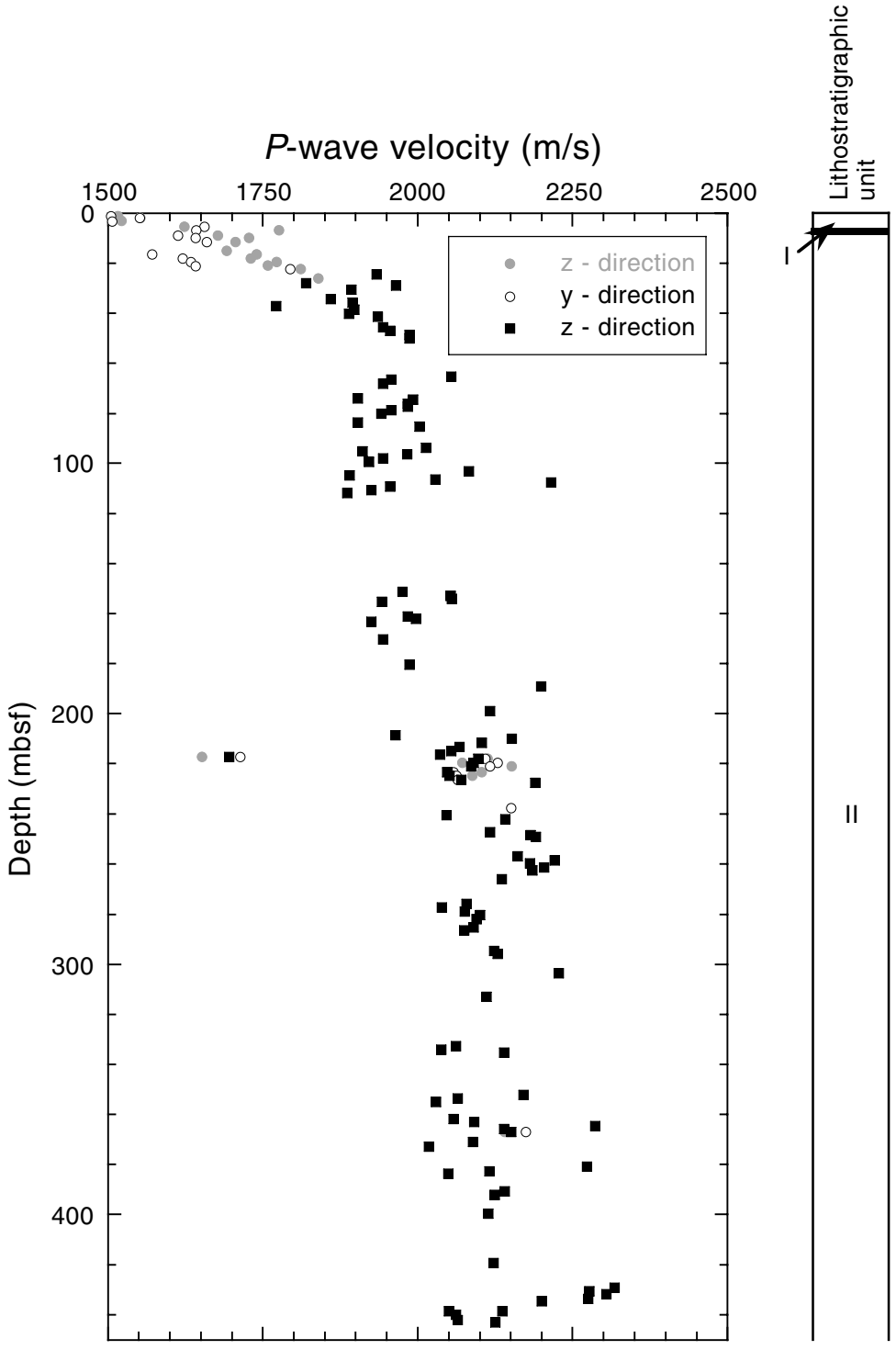

Figure F35. Measurements of undrained shear strength from Site 1167, using the AVS, FC, and PP. The columns to the right show lithostratigraphic units and core recovery. FC = fall cone; PP = pocket penetrometer; and AVS = automatic vane sheer.

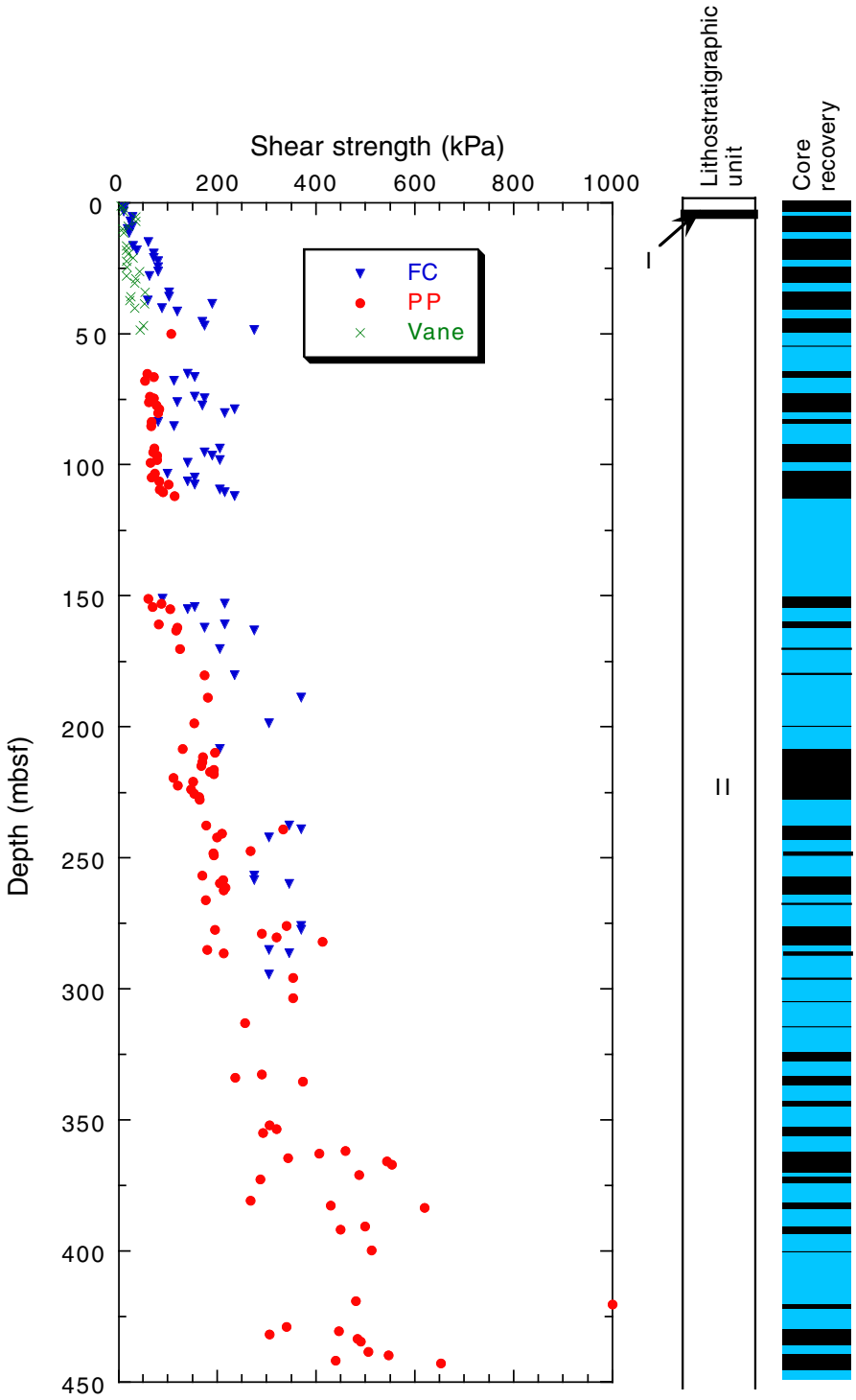

Figure F36. Normalized undrained shear strength with respect to effective overburden pressure. The shaded area shows the expected range for sediments of intermediate plasticity. The regions where advanced hydraulic piston corer (APC) and extended core barrel (XCB) coring was used is indicated. The columns to the right show lithostratigraphic units and core recovery. FC = fall cone; PP = pocket penetrometer.

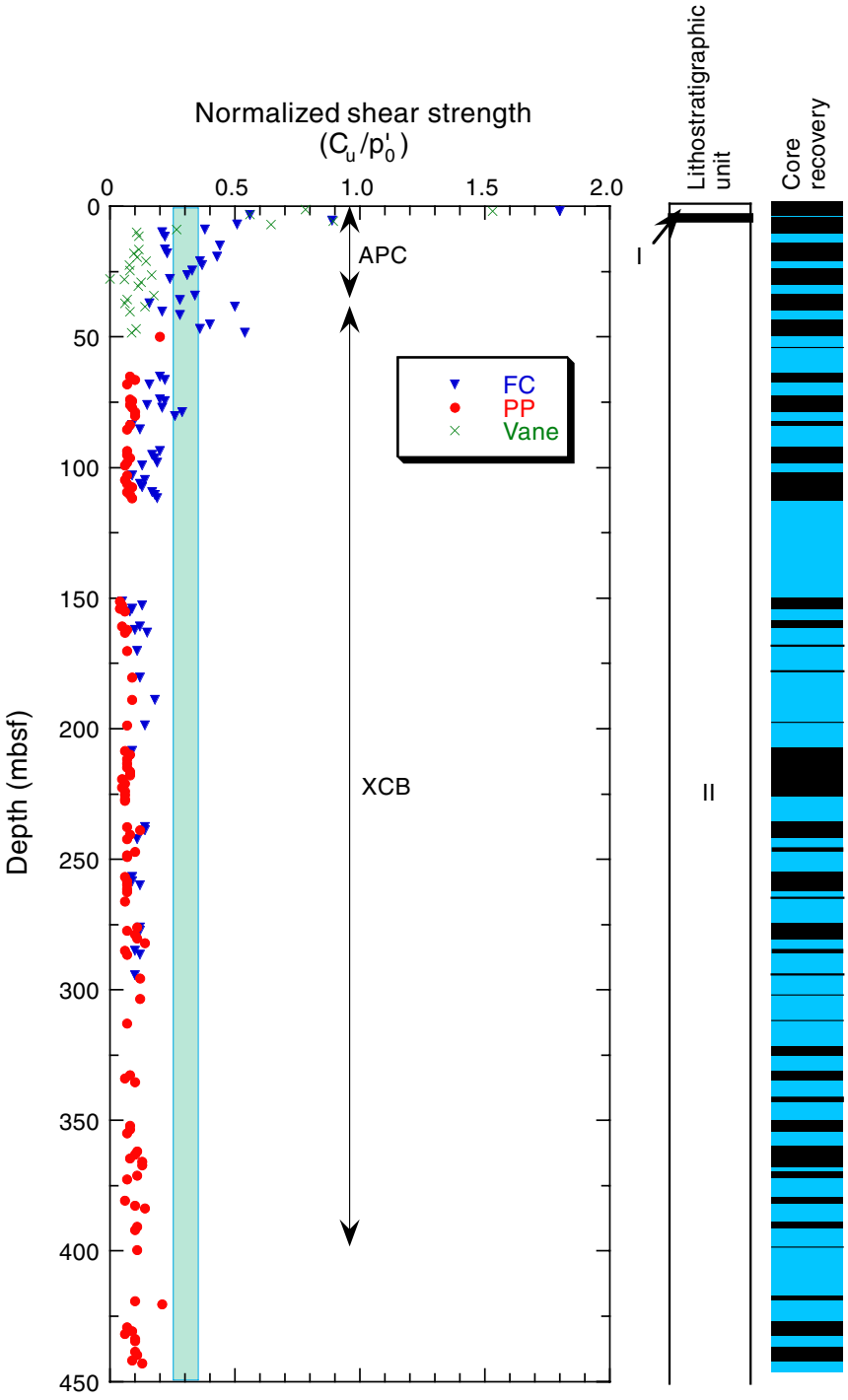

Figure F37. Thermal conductivity measurements from Site 1167. The columns on the right show lithostratigraphic units and core recovery.

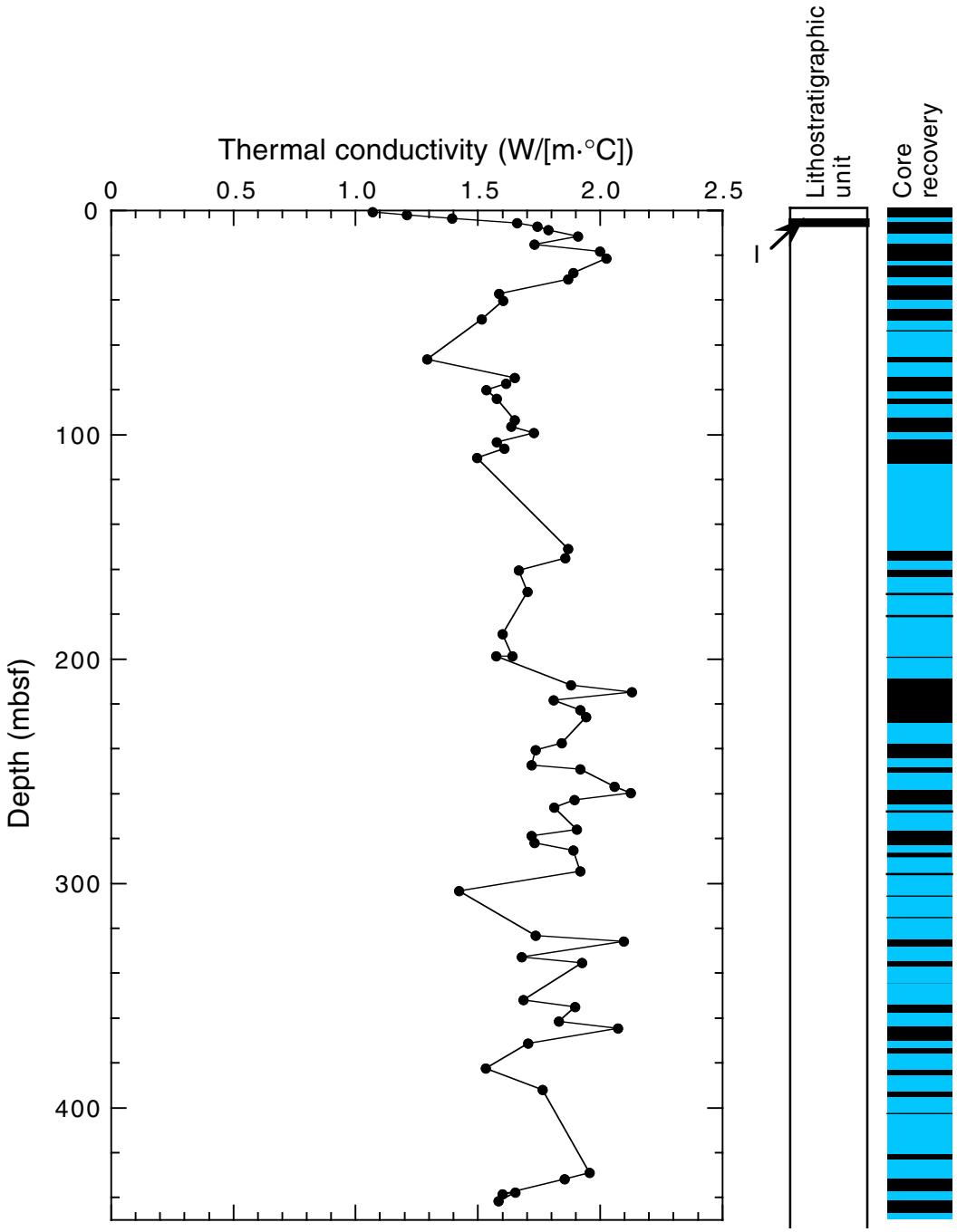

Figure F38. Measured temperature vs. time from deployment of the Adara temperature tool for Core 188-1167A-4H (39.7 mbsf). T_{SF} = seafloor temperature; APC = advanced hydraulic piston corer.

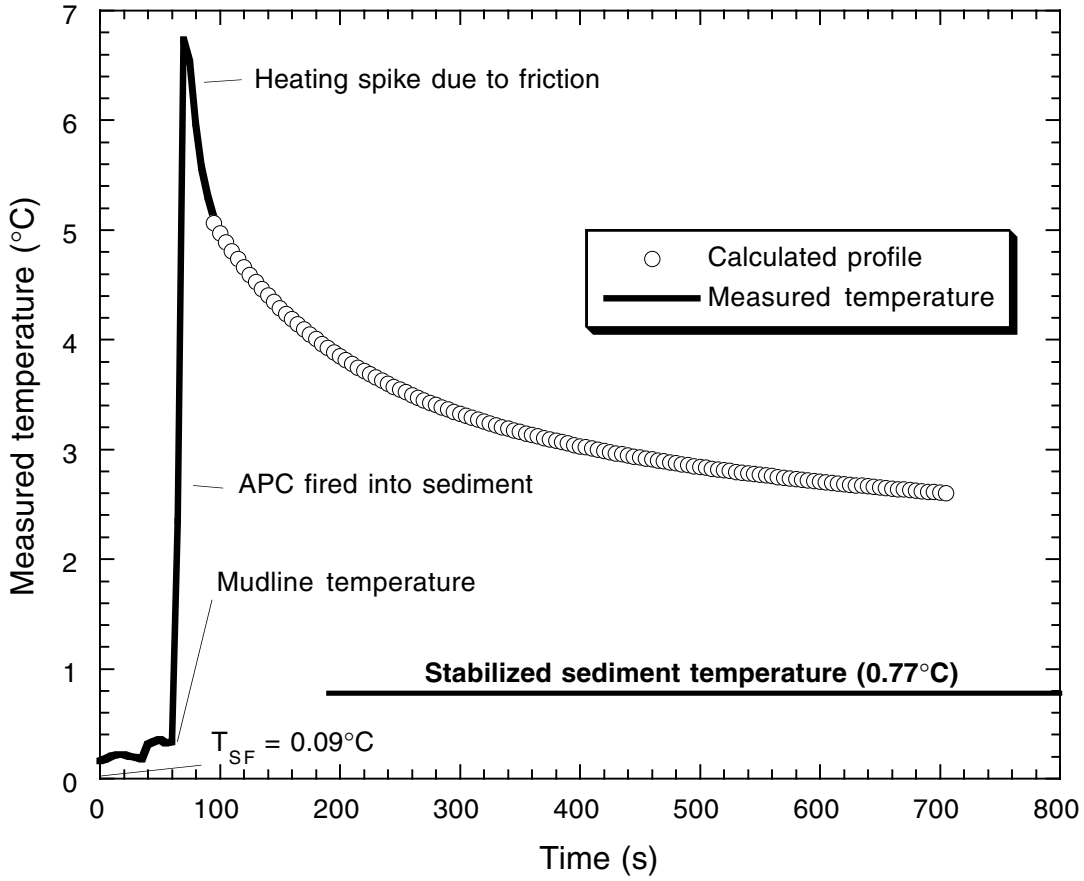

Figure F39. Measured and estimated temperature vs. depth profile for Site 1167.

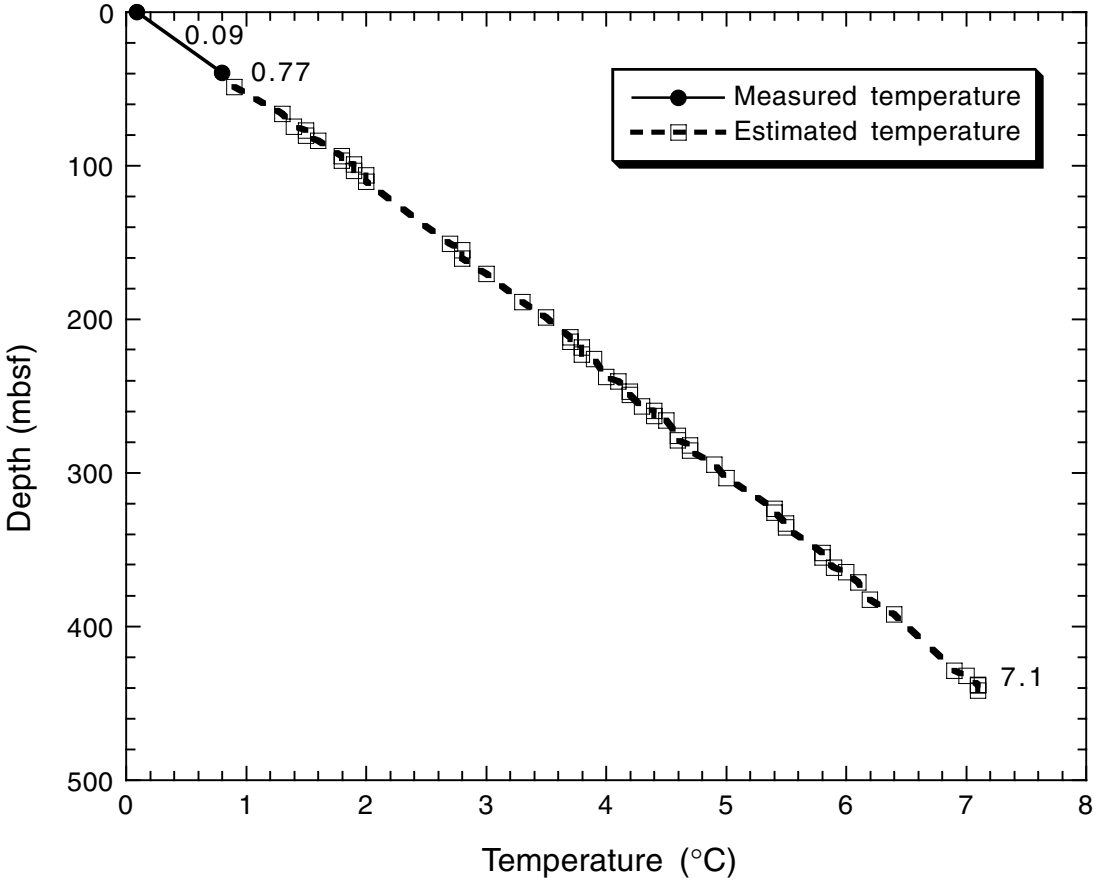

Figure F40. Logging summary diagram showing log, pipe, and seafloor depths.

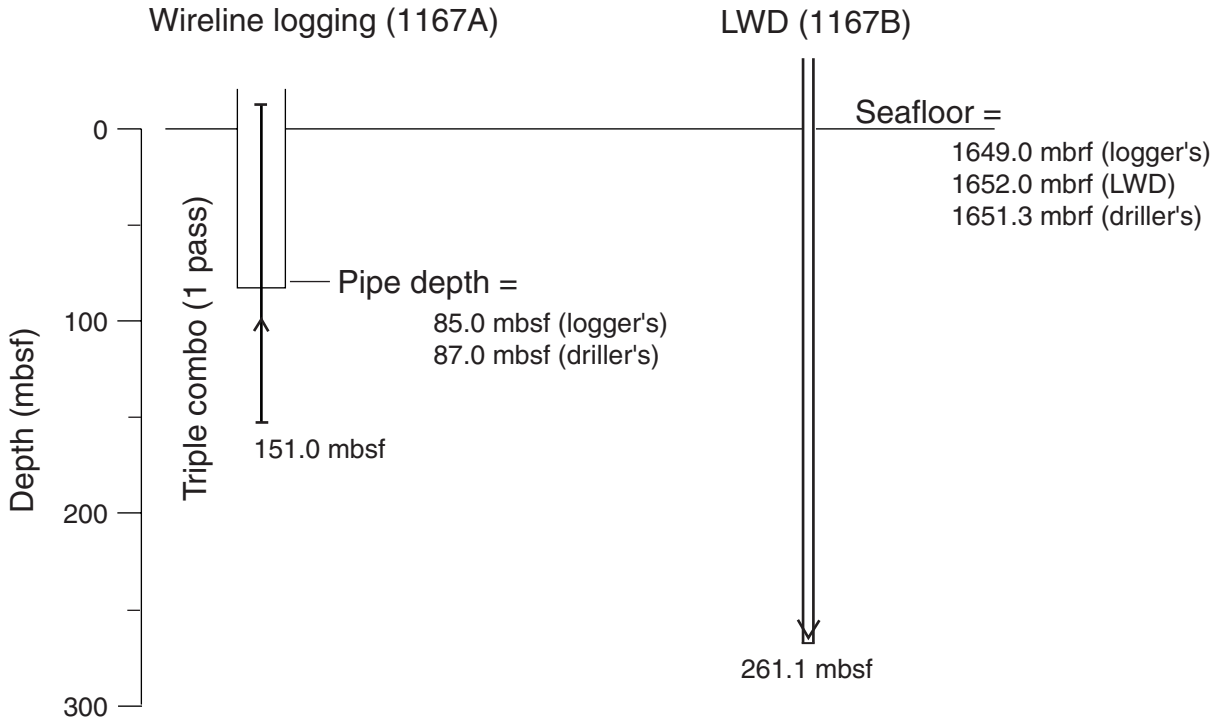

Figure F41. Gamma-ray, resistivity, density, and porosity logs from the triple combo wireline tools and gamma ray and resistivity from the CDR LWD tool over the 85- to 150-mbsf interval that was covered by both wireline logging and LWD.

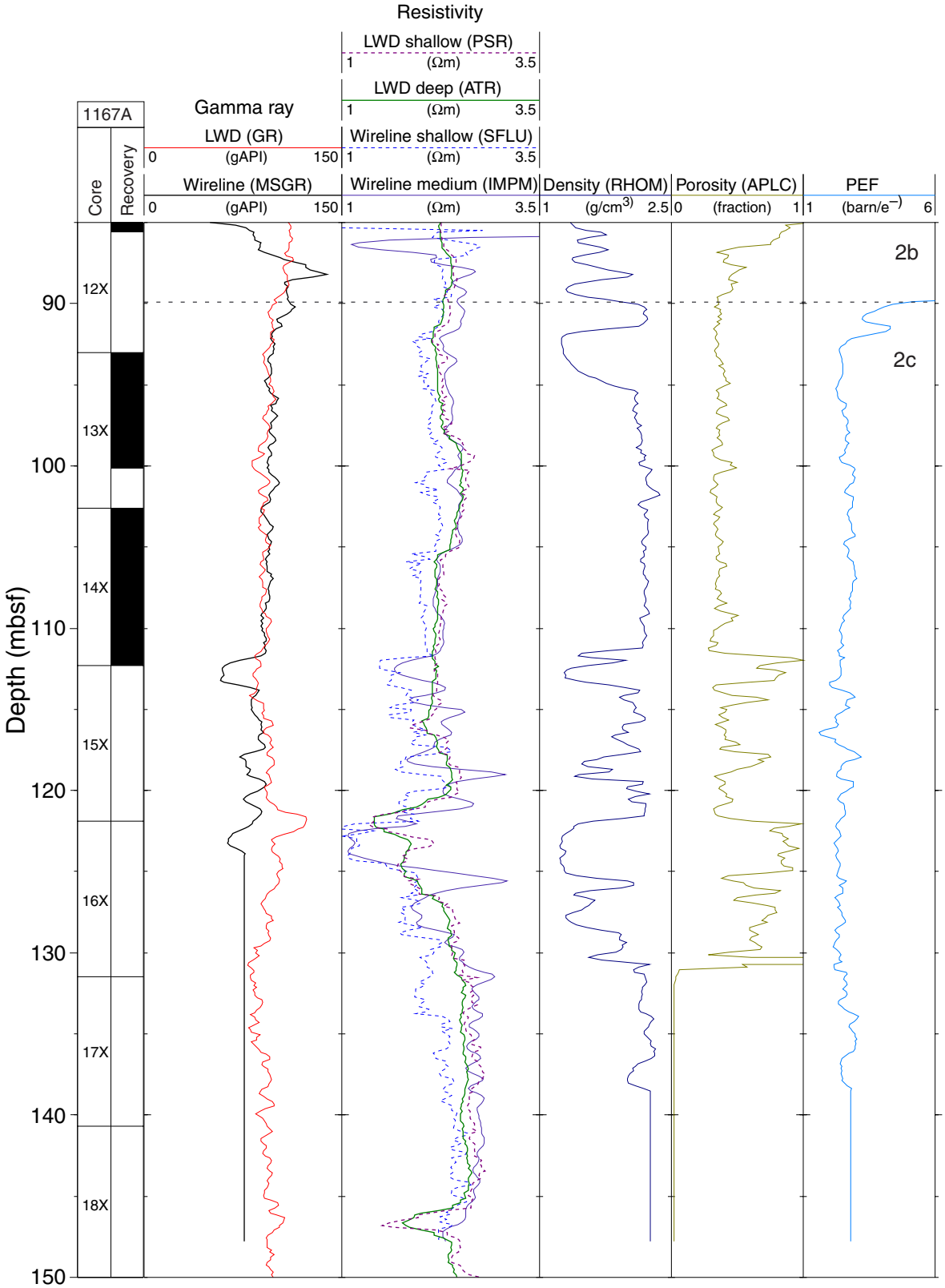

Figure F42. Gamma-ray and resistivity logs and susceptibility measured on core samples. Thin shaded intervals = intervals of low resistivity interpreted as clays.

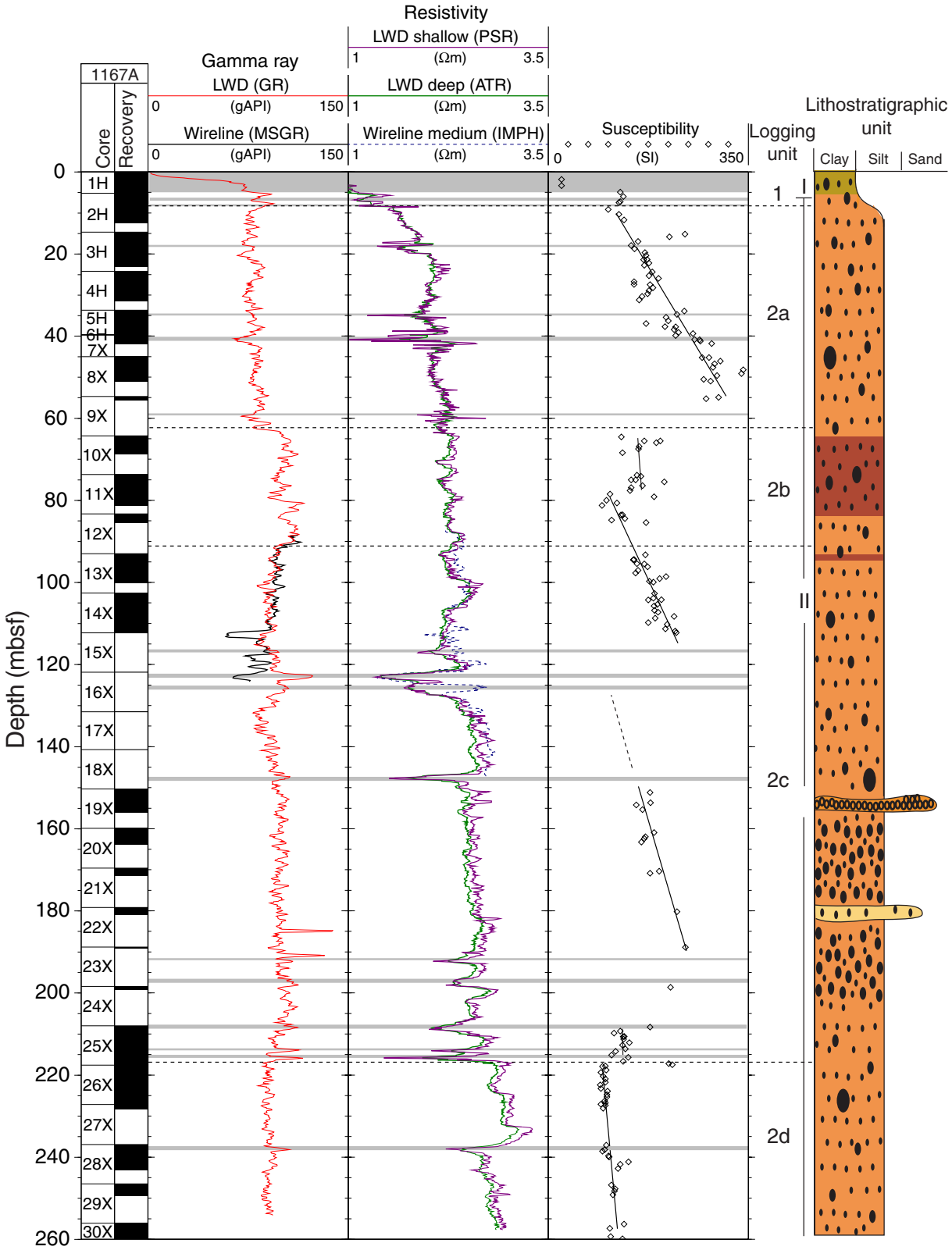

Figure F43. Downhole temperatures from the TAP tool (see **"Temperature Log,"** p. 34, in "Downhole Measurements."

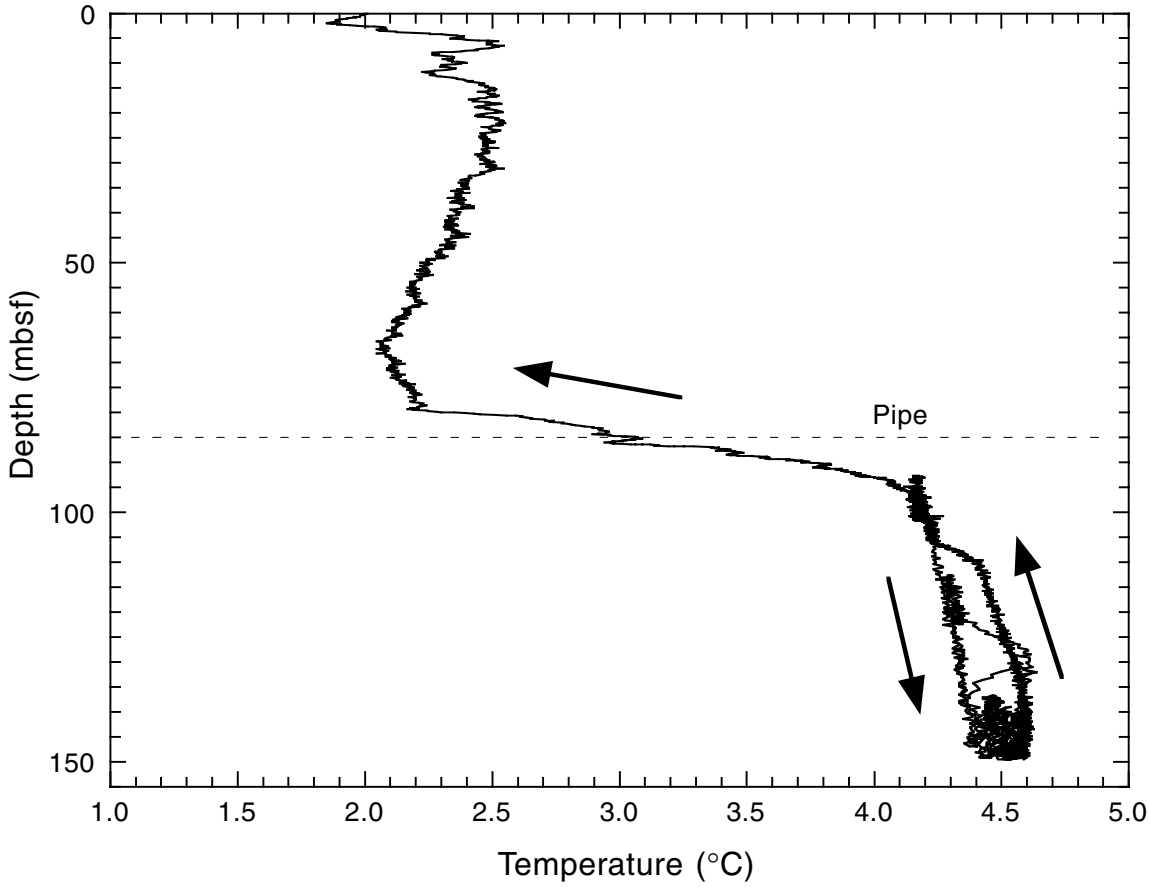

Table T1. Coring summary, Site 1167.

Core	Date (Feb 2000)	Ship local time	Depth (mbsf) Top	Depth (mbsf) Bottom	Length (m) Cored	Length (m) Recovered	Recovery (%)
188-1167A-							
1H	23	0945	0.0	5.2	5.2	5.17	99.4
2H	23	1035	5.2	14.7	9.5	7.30	76.8
3H	23	1155	14.7	24.2	9.5	8.43	88.7
4H	23	1240	24.2	33.7	9.5	7.36	77.5
5H	23	1345	33.7	39.7	6.0	6.02	100.3
6H	23	1445	39.7	39.7	0.0	0.00	0.0
7X	23	1535	39.7	45.0	5.3	2.21	41.7
8X	23	1625	45.0	54.7	9.7	6.14	63.3
9X	23	1740	54.7	64.3	9.6	0.86	9.0
10X	23	1820	64.3	73.7	9.4	4.55	48.4
11X	23	1910	73.7	83.3	9.6	7.65	79.7
12X	23	2000	83.3	93.0	9.7	2.30	23.7
13X	23	2045	93.0	102.6	9.6	7.19	74.9
14X	23	2140	102.6	112.3	9.7	9.94	102.5
15X	23	2235	112.3	121.9	9.6	0.00	0.0
16X	23	2330	121.9	131.5	9.6	0.00	0.0
17X	24	0025	131.5	140.7	9.2	0.10	1.1
18X	24	0120	140.7	150.3	9.6	0.00	0.0
19X	24	0320	150.3	159.9	9.6	5.74	59.8
20X	24	0455	159.9	169.6	9.7	4.00	41.2
21X	24	0730	169.6	179.2	9.6	1.89	19.7
22X	24	1420	179.2	188.8	9.6	1.85	19.3
23X	24	1600	188.8	198.4	9.6	0.42	4.4
24X	24	1725	198.4	208.0	9.6	0.93	9.7
25X	24	1850	208.0	217.6	9.6	9.97	103.9
26X	24	2020	217.6	227.2	9.6	9.85	102.6
27X	24	2135	227.2	236.9	9.7	1.12	11.5
28X	24	2310	236.9	246.5	9.6	6.20	64.6
29X	25	0725	246.5	256.1	9.6	2.87	29.9
30X	25	0845	256.1	265.7	9.6	7.43	77.4
31X	25	1020	265.7	275.3	9.6	1.26	13.1
32X	25	1135	275.3	284.6	9.3	7.82	84.1
33X	25	1310	284.6	293.9	9.3	2.58	27.7
34X	25	1435	293.9	303.2	9.3	2.63	28.3
35X	26	0655	303.2	312.8	9.6	0.73	7.6
36X	26	0850	312.8	322.5	9.7	0.55	5.7
37X	26	1035	322.5	332.1	9.6	4.28	44.6
38X	26	1225	332.1	341.7	9.6	4.08	42.5
39X	26	1355	341.7	351.3	9.6	2.26	23.5
40X	26	1550	351.3	360.9	9.6	4.74	49.4
41X	26	1725	360.9	370.6	9.7	7.80	80.4
42X	26	2020	370.6	380.2	9.6	2.98	31.0
43X	26	2240	380.2	389.8	9.6	3.74	39.0
44X	27	0100	389.8	399.4	9.6	2.99	31.1
45X	27	0305	399.4	409.0	9.6	0.83	8.6
46X	27	0515	409.0	418.7	9.7	0.30	3.1
47X	27	0755	418.7	428.3	9.6	1.91	19.9
48X	27	1000	428.3	437.9	9.6	6.56	68.3
49X	27	1240	437.9	447.5	9.6	5.80	60.4
				Totals:	447.5	191.33	42.7

Table T2. Expanded coring summary, Site 1167.

Core	Date (Feb 2000)	Ship local time	Core depth (mbsf) Top	Core depth (mbsf) Bottom	Length (m) Cored	Length (m) Recovered	Recovery (%)	Section	Length (m) Liner	Length (m) Curated	Section depth (mbsf) Top	Section depth (mbsf) Bottom	Catwalk samples	Comment
Position: 66.40018°S, 17.28419°E														
Water depth (mbrf; APC calculation): 1651.3														
188-1167A-														
1H	23	0945	0.0	5.2	5.2	5.17	99.4							
								1	1.50	1.50	0.00	1.50	IW	
								2	1.50	1.50	1.50	3.00	IW	
								3	1.50	1.50	3.00	4.50	IW, HS	
								4	0.52	0.52	4.50	5.02		
								CC (NS)	0.15	0.15	5.02	5.17	PAL	All to PAL
									5.17	5.17				
2H	23	1035	5.2	14.7	9.5	7.30	76.8							
								1	1.50	1.50	5.20	6.70	IW	
								2	1.50	1.50	6.70	8.20	IW	
								3	1.50	1.50	8.20	9.70	IW	
								4	1.50	1.50	9.70	11.20	IW, HS	
								5	1.01	1.01	11.20	12.21		
								CC (w/5)	0.29	0.29	12.21	12.50	PAL	
									7.30	7.30				
3H	23	1155	14.7	24.2	9.5	8.43	88.7							
								1	1.50	1.50	14.70	16.20	IW	
								2	1.50	1.50	16.20	17.70	IW	
								3	1.50	1.50	17.70	19.20	IW	
								4	1.50	1.50	19.20	20.70	IW	
								5	1.50	1.50	20.70	22.20	HS, HSTL, IW	
								6	0.64	0.64	22.20	22.84		
								CC (w/6)	0.29	0.29	22.84	23.13	PAL	
									8.43	8.43				
4H	23	1240	24.2	33.7	9.5	7.36	77.5							
								1	1.50	1.50	24.20	25.70	IW	
								2	1.50	1.50	25.70	27.20	IW	
								3	1.50	1.50	27.20	28.70	IW	
								4	1.50	1.50	28.70	30.20	IW	
								5	1.17	1.17	30.20	31.37	HS	
								CC (w/5)	0.19	0.19	31.37	31.56	PAL	
									7.36	7.36				
5H	23	1345	33.7	39.7	6.0	6.02	100.3							
								1	1.50	1.50	33.70	35.20	IW	
								2	1.50	1.50	35.20	36.70	IW	
								3	1.50	1.50	36.70	38.20	IW, PAL	
								4	1.15	1.15	38.20	39.35	HS	

Notes: CC = core catcher (number in parentheses indicates which section the core catcher is stored with). NS = all of the core catcher was used for paleontology sample, IW = interstitial water sample, HS = headspace sample, HSTL = headspace sample for shore-based investigation, PAL = paleontology sample, CARL = whole-round samples for geotechnical experiments. Only a portion of this table appears here. The complete table is available in **ASCII format.**

Table T3. List of lonestone and dispersed granules, Site 1167.

Core	Section	Depth (cm)	Depth (mbsf)	Lithology	Angularity	Size (cm)	General shape	Comments
188-1167A-								
1H	1	42	0.42	Quartzite/gneiss?	Subangular	1.5	Ovoid	Fe stained/gneissic banding
1H	1	48	0.48	Quartzite/gneiss?	Subrounded	1.5	Ovoid	Fe stained/gneissic banding
1H	1	86	0.86	Garnet gneiss	Subangular	3	Pyramidal	Weathered?
1H	1	96	0.96	Pyroxene gneiss	Subangular	2	Pyramidal	Weathered?
1H	1	102	1.02	Pyroxene gneiss	Angular	3	Flat tabular	
1H	2	55	2.05	Granitic gneiss	Angular	2	Triangular	
1H	2	71	2.21	Metasediment	Subangular	3	Flat tabular	Bedded, mica-schist and quartzite
1H	2	134	2.84	Quartzite/gneiss	Subangular	2	Ovoid	Fe stained/gneissic banding
1H	3	63	3.63	Pebble conglomerate	Subrounded	2	Ovoid	Weathered/Fe stained
1H	3	64	3.64	Granite gneiss	Subangular	3.5	Pyramidal	
1H	3	64	3.65	Pebble conglomerate	Subrounded	1.5	Ovoid	Weathered/Fe stained
1H	4	22	4.72	Pyroxene gneiss	Subangular	4	Blocky	
1H	4	30	4.80	Garnet gneiss	Subangular	5	Blocky	
1H	4	30	4.81	Quartzite/gneiss	Subangular	2	Flat tabular	
2H	1	94	6.14	Gneiss	Subangular	1.5	Ovoid	
2H	2	23	6.93	Garnet gneiss	Subangular	1.5	Ovoid	
2H	2	26	6.96	Coal clast	Subrounded	0.5	Blocky	
2H	2	62	7.32	Quartzite/gneiss	Subangular	4	Blocky	Gneissic banding
2H	2	114	7.84	Metasediment/schist	Subrounded	2	Flat tabular	
2H	3	7	8.27	Coaly clast	Subrounded	0.5		
2H	3	90	9.10	Granite	Subangular	2	Blocky	
2H	3	92	9.12	Granite	Subangular	1.5	Blocky	
2H	3	144	9.64	Green quartzite?	Subrounded	1.5	Ovoid	
2H	4	104	10.74	Granite	Subangular	2	Blocky	
2H	5	26	11.46	Granite	Subangular	1	Blocky	
2H	CC	17	12.38	Biotite clast	Subrounded	0.5	Flat ovoid	
3H	1	133	16.03	Pyrite clast		1	Flattened burrow?	Pseudomorph after a burrow?
3H	1	140	16.10	Garnet gneiss	Subangular	4	Flat tabular	
3H	2	25	16.45	Green quartzite	Angular	4	Blocky	Metasandstone/thin section
3H	2	50	16.70	2 × garnet gneiss	Subangular	2	Blocky	
3H	2	107	17.27	Sandstone	Subangular	3	Ovoid	White/well cemented/quartzite?
3H	3	40	18.10	Garnet gneiss	Subangular	1	Blocky	
3H	3	45	18.15	Dark green quartzite?	Subangular	3	Flat tabular	Possible banding/thin section
3H	3	103	18.73	Granite	Subangular	1.5	Ovoid	
3H	3	104	18.74	Quartz clast	Subangular	1	Blocky	
3H	6	40	22.60	Garnet gneiss	Subangular	6	Blocky	
4H	1	26	24.46	Dark green quartzite?	Angular	2	Platy	Metamorphic
4H	2	52	26.22	Quartzite?	Subrounded	2	Ovoid	Metamorphic?
4H	2	120	26.90	Quartz	Rounded	2	Spherical	
4H	3	52	27.72	Diorite	Rounded	3	Elongate	
4H	3	99	28.19	Granite	Angular	3	Square	
4H	4	50	29.20	Tonalite?	Subangular	3	Triangular	Igneous?
4H	4	98	29.68	Gneiss	Rounded	2	~Spherical	
4H	5	1	30.21	Granite	Subangular	2	Platy	
4H	5	31	30.51	Metamorphic?	Angular	2	Platy	Schist?
5H	1	42	34.12	Quartzite?	Subrounded	1	Ovoid	
5H	1	81	34.51	Claystone	Rounded	2	Ovoid	
5H	1	90	34.60	Red granite	Subangular	1	Spherical	
5H	1	95	34.65	Granite	Subangular	1	Spherical	
5H	1	132	35.02	Quartzite?	Subrounded	1	Ovoid	
5H	2	10	35.30	Pyrite clast	Subangular	1	Ovoid	
5H	2	17	35.37	Pyrite clast	Subangular	2	Ovoid	
5H	2	27	35.47	Pyrite clast	Subangular	2	Ovoid	
5H	2	33	35.53	Pyrite clast	Subrounded	1	Ovoid	
5H	2	80	36.00	Pyrite clast	Subangular	2	Ovoid	
5H	2	122	36.42	Metamorphic?	Subangular	3	Ovoid	
5H	3	75	37.45	Granite gneiss	Subrounded	7	Ovoid	
5H	4	34	38.54	Intermediate igneous	Subrounded	3	Quadratic	
5H	4	62	38.82	Schist	Rounded	1	~Spherical	
5H	5	21	39.56	Schist	Subrounded	3	Oblate	
7X	1	33	40.03	Quartzite	Rounded	5	Oblong	
7X	1	37	40.07	Gneiss	Subrounded	3	~Spherical	
7X	1	40	40.10	Dark, dense, unknown	Subang.	4	Oblong	
7X	2	40	41.60	Tonalite	Subrounded	3	Oblong	
7X	2	53	41.73	Tonalite	Subrounded	2	Oblong	
8X	1	133	46.33	Granite gneiss	Rounded	4	Oblong	

Note: Only a portion of this table appears here. The complete table is available in **ASCII format.**

Table T4. Abundance of foraminifers in samples, Hole 1167A.

Core, section, interval (cm)	Very good	Good	Poor	Barren
188-1167A-				
1H-CC				X
2H-CC		X		
3H-CC			X	
4H-CC			X	
5H-3, 34-36	X			
5H-CC			X	
7X-CC		X		
8X-CC		X		
9X-CC			X	
10X-CC		X		
11X-CC			X	
12X-CC			X	
13X-CC		X		
14X-CC		X		
17X-CC	X			
19X-CC		X		
20X-CC		X		
21X-CC			X	
22X-CC			X	
23X-CC			X	
24X-CC			X	
25X-CC, 22-23	X			
25X-CC				X
26X-CC				X
27X-CC			X	
28X-CC				X
29X-CC				X
30X-CC			X	
31X-CC				X
32X-CC		X		
33X-CC			X	
34X-CC				X
35X-1, 68-73			X	
36X-CC		X		
37X-CC			X	
38X-CC			X	
39X-CC		X		
40X-CC				X
41X-CC			X	
42X-CC			X	
43X-CC		X		
44X-CC				X
45X-CC				X
46X-CC			X	
47X-CC				X
48X-CC		X		
49X-CC				X

Note: Very good = >100 specimens per sample; good = ~50; poor = ~10 or less; barren = none.

Table T5. Interstitial water chemistry from shipboard measurements, Site 1167.

Core, section	Depth (mbsf)	Salinity	pH	Alkalinity (mM)	Cl (mM)	SO_4 (mM)	NH_4 (μM)	PO_4 (μM)	H_4SiO_4 (μM)	Ca (mM)	Mg (mM)	Sr (μM)	K (mM)	Na (mM)	Li (μM)	Mn (μM)
188-1167A-																
1H-1	1.45	35.0	7.67	3.11	565.0	28.8	0.0	6.0	568.1	11.3	54.6	101.7	12.3	481.6	29.0	14.5
1H-2	2.95	35.0	7.84	2.74	559.5	29.2	0.0	4.6	672.7	11.6	54.5	92.1	12.6	476.0	24.8	25.5
1H-3	4.45	35.0	7.84	2.55	566.0	28.8	0.0	6.0	648.1	11.5	52.6	95.3	12.3	485.8	27.4	19.1
2H-1	6.65	35.0	7.86	2.74	563.5	29.3	0.0	2.3	274.8	12.4	52.2	101.1	11.4	484.3	25.9	20.4
2H-2	8.10	35.0	8.06	2.70	559.5	29.2	3.3	0.7	178.4	12.7	50.0	153.0	11.1	484.0	21.9	14.4
3H-3	9.65	35.0	7.88	2.60	576.6	29.3	9.9	0.7	186.6	13.4	50.6	103.2	10.5	499.2	20.8	15.7
2H-4	11.15	35.0	7.91	2.50	568.6	29.4	16.4	0.0	194.8	13.7	49.7	105.2	10.0	493.1	20.2	16.6
3H-1	16.10	35.5	7.92	2.11	574.6	29.6	19.7	0.0	186.6	15.0	48.2	116.0	8.2	501.3	17.6	19.7
3H-2	17.60	35.0	8.06	2.23	574.6	29.8	29.5	0.0	186.6	15.6	48.3	115.9	7.7	500.9	13.3	16.9
3H-3	19.10	35.0	7.97	2.04	572.1	29.8	36.0	0.0	221.5	16.5	50.1	122.0	8.2	492.3	16.5	16.8
3H-4	20.60	35.0	7.82	1.90	573.1	29.5	44.2	0.0	215.4	17.5	50.4	125.9	7.7	490.3	15.4	20.2
3H-5	22.10	35.5	7.97	1.85	573.1	29.8	42.5	0.0	194.8	17.9	49.9	128.8	7.0	491.9	13.9	19.0
4H-1	25.60	35.5	8.07	2.01	573.1	29.7	39.3	0.0	198.9	17.9	46.8	125.5	6.0	499.0	11.9	19.6
4H-2	27.10	35.5	7.99	1.51	572.6	29.7	47.4	0.0	203.0	10.2	25.2	125.2	5.1	557.6	8.9	19.4
4H-3	28.60	35.5	8.15	1.78	577.1	29.7	54.0	0.0	215.4	19.7	48.2	133.4	6.4	496.2	11.5	18.3
4H-4	30.10	35.5	8.25	1.86	576.1	29.5	57.2	0.0	190.7	19.9	47.5		5.6	496.6	0.1	17.7
5H-1	35.10	35.5	7.86	1.61	568.0	29.1	49.1	0.0	213.3	20.1	44.2	131.2	4.4	494.7	5.5	17.7
5H-2	36.60	35.5	7.99	1.51	562.5	29.2	62.1	0.0	219.5	19.9	43.5	142.7	4.3	491.2	8.7	14.4
5H-3	38.10	35.5	7.82	1.35	571.6	29.0	58.9	0.0	229.7	21.7	45.7	136.5	4.0	492.1	8.6	18.3
7X-1	41.10	35.5	8.02	1.34	565.5	28.9	81.7	0.0	225.6	23.4	46.2	140.0	3.9	481.5	5.3	15.8
8X-1	46.40	35.5	8.19	1.57	570.6	29.0	76.8	1.4	211.3	22.5	45.4	142.2	4.2	490.2	9.5	1.0
8X-2	47.90	35.5	8.21	1.69	571.1	29.0	81.7	2.1	225.6	23.5	46.1	137.8	4.2	487.4	6.3	17.7
8X-3	49.40	35.5	8.23	1.46	554.5	28.7	81.7	0.9	276.9	23.6	43.5	142.4	3.4	475.8	8.7	18.2
10X-2	67.20	35.0	7.84	1.29	566.0	28.1	78.5	0.0	244.1	24.2	41.1	149.3	2.7	490.1	9.7	18.5
11X-5	79.50	35.0	8.28	1.59	565.0	28.2	91.5	0.0	221.5	24.5	40.8	143.1	2.2	490.3	5.4	16.6
12X-1	84.70	34.5	8.19	1.43	561.0	28.0	80.1	0.0	240.0	24.6	40.3	149.5	2.5	486.2	5.7	18.7
13X-4	98.78	34.5	7.92	1.31	562.5	27.8	89.9	0.0	256.4	26.2	38.8	159.8	2.1	487.2	8.4	17.6
19X-3	154.70	34.5	8.02	1.49	549.4	27.4	89.9	0.0	311.8	23.8	37.3	161.8	2.5	481.0	11.7	19.9
21X-1	171.00	34.5	7.91	1.22	555.0	26.9	70.3	0.0	324.1	26.8	36.6	134.4	2.5	480.6	10.8	10.5
25X-4	213.90	34.5	8.11	1.48	551.0	26.7	63.8	0.0	301.5	25.0	36.9	168.9	1.8	480.3	9.3	20.0
28X-3	241.40	34.5	8.13	1.54	552.0	27.3	80.1	0.0	309.7	27.7	41.5	183.1	2.3	467.4	12.8	20.4
30X-3	260.50	34.5	8.30	1.44	552.5	26.7	89.9	0.0	328.2	24.7	35.6	188.9	2.1	484.6	11.8	16.0
33X-3	286.00	34.0	8.30	1.58	553.0	26.4	54.0	0.0	301.5	25.4	35.8	181.4	1.9	483.0	9.4	18.3
38X-2	334.96	34.0	8.32	1.57	540.9	25.2	52.3	0.0	324.1	26.8	33.9	204.3	2.4	469.1	14.8	14.4
40X-2	354.20	34.0	7.87	4.25	532.9	25.0	63.8	0.0	422.5	28.7	31.0		2.7	465.0		
43X-1	381.60	34.0	8.25	1.95	544.9	24.9	54.0	0.0	311.8	26.6	35.2		2.4	470.9		
48X-3	432.65	34.0	8.33	1.94	552.0	24.1	58.9	0.0	311.8	28.2	31.9		2.7	479.3		

Table T6. Carbon, nitrogen, and sulfur analyses of sediments, Site 1167.

Core, section, interval (cm)	Depth (mbsf)	IC (wt%)	$CaCO_3$ (wt%)	TC (wt%)	OC (wt%)	TN (wt%)	TS (wt%)	C/N
188-1167A-								
1H-1, 0-5	0.33	0.058	0.48					
1H-3, 39-40	3.39	0.030	0.25	0.24	0.21	0.02	0.11	50.00
1H-4, 44-45	4.94	0.044	0.36					
2H-1, 38-39	5.58	0.096	0.80					
2H-3, 80-81	9.00	0.065	0.54	0.47	0.41	0.03	0.03	15.67
2H-5, 84-85	12.04	0.092	0.77					
3H-5, 85-86	21.55	0.095	0.79	0.49	0.39	0.02	0.04	24.50
4H-1, 48-49	24.68	0.099	0.83					
5H-1, 50-51	34.20	0.082	0.68	0.77	0.69	0.03	0	25.67
5H-3, 50-51	37.20	0.155	1.29					
7X-1, 50-51	40.20	0.110	0.92					
8X-1, 50-51	45.50	0.118	0.98	0.44	0.32	0.02	0.01	22.00
8X-3, 50-51	48.50	0.109	0.91					
9X-1, 26-27	54.96	0.121	1.01	0.46	0.34	0.04	0.01	11.50
10X-1,120-121	65.50	0.112	0.93					
10X-3,120-121	68.50	0.209	1.74					
11X-1, 30-31	74.00	0.096	0.80					
11X-3, 31-32	75.84	0.111	0.93	0.37	0.26	0.02	0.01	18.50
11X-5, 29-30	78.39	0.008	0.06					
12X-1, 40-41	83.70	0.111	0.93					
13X-1, 39-40	93.39	0.115	0.96	0.46	0.34	0.04	0.02	11.50
13X-3, 40-41	96.28	0.094	0.79					
13X-5, 39-40	99.27	0.116	0.97					
14X-1, 66-67	103.26	0.114	0.95					
14X-3, 71-72	106.31	0.096	0.80	0.46	0.36	0.04	0.02	11.50
19X-1, 101-102	151.31	0.120	1.00					
19X-3, 83-84	154.13	0.382	3.18					
20X-3, 31-32	163.21	0.133	1.11	0.49	0.36	0.03	0.02	16.33
21X-1, 65-66	170.25	0.079	0.66					
22X-1, 103-105	180.23	0.107	0.89	0.77	0.66	0.02	0	38.50
25X-1, 125-126	209.25	0.408	3.40					
25X-4, 34-35	212.84	0.080	0.67	0.76	0.68	0.04	0	19.00
25X-7, 16-17	217.16	0.087	0.72					
26X-1, 50-51	218.10	0.108	0.90					
26X-3, 50-51	221.10	0.148	1.23					
26X-5, 50-51	224.10	0.170	1.41	0.84	0.67	0.04	0	21.00
27X-1, 50-51	227.58	0.103	0.86					
28X-2, 37-38	238.77	0.099	0.83					
28X-4, 39-40	241.89	0.087	0.73	0.65	0.56	0.03	0	21.67
29X-1, 85-86	247.35	0.088	0.74					
29X-2, 42-43	248.42	0.058	0.49					
30X-1, 73-74	256.83	0.087	0.72	0.52	0.43	0.02	0	26.00
30X-3, 66-67	259.76	0.063	0.53					
30X-5, 47-48	262.57	0.156	1.30					
31X-1, 55-56	266.25	0.104	0.86					
32X-3, 73-74	279.03	0.064	0.54	1.06	0.99	0.03	0	35.33
33X-2, 43-44	286.53	0.093	0.77					
34X-2, 39-40	295.79	0.114	0.95					
35X-1, 37-38	303.57	0.114	0.95	0.44	0.32	0.02	0	22.00
38X-1, 59-60	332.69	0.157	1.31	0.53	0.37	0.02	0.03	26.50
38X-3, 28-29	335.34	0.122	1.01					
40X-2, 64-65	353.44	0.111	0.93	0.52	0.41	0.02	0	26.00
42X-2, 69-70	372.79	0.126	1.05	0.55	0.42	0.02	0	27.50
43X-2, 104-105	382.74	0.137	1.14	0.82	0.68	0.03	0	27.33
44X-1, 47-48	390.27	0.116	0.97	0.49	0.37	0.03	0	16.33
45X-1, 42-43	399.82	0.105	0.88	0.45	0.34	0.02	0	22.50
46X-CC, 4-5	409.04	0.084	0.70	0.93	0.85	0.02	0	46.50
47X-1, 56-57	419.26	0.111	0.92	0.53	0.42	0.02	0	26.50
47X-CC, 40-41	420.49	0.122	1.02					
48X-1, 84-85	429.14	0.087	0.73					
48X-2, 35-38	430.15	0.105	0.87					
48X-4, 79-80	433.59	0.098	0.81	0.50	0.40	0.50	0	1.00
49X-1, 70-71	438.60	0.098	0.82					
49X-3, 101-102	441.91	0.091	0.76	0.50	0.41	0.70	0	0.71
49X-4, 54-55	442.94	0.085	0.71					

Note: IC = inorganic carbon, $CaCO_3$ = calcium carbonate, TC = total carbon, OC = organic carbon, TN = total nitrogen, TS = total sulfur.

Table T7. Organic carbon and Rock-Eval pyrolysis on selected samples, Site 1167.

Core, section, interval (cm)	Depth (mbsf)	OC wt%	S_1 (mg/g)	S_2 (mg/g)	S_3 (mg/g)	HI (mg/g C)	T_{max} (°C)
188-1167A-							
5H-1, 50-51	34.20	0.69	0.02	0.12	0.14	17	515
14X-3, 71-72	106.31	0.40	0.02	0.09	0.20	23	534
22X-1, 103-105	180.23	0.66	0.12	0.18	0.40	27	480
25X-4, 34-35	212.84	0.68	0.08	0.21	0.29	31	462
26X-5, 50-51	224.10	0.67	0.08	0.13	0.40	19	480
28X-4, 39-40	241.89	0.56	0.15	0.21	0.42	38	451
32X-3, 73-74	279.03	0.99	0.12	0.21	0.37	21	480
43X-2, 104-105	382.74	0.68	0.16	0.15	0.53	22	465
46X-CC, 4-5	409.04	0.88	0.15	0.21	0.42	24	471

Note: For explanation of column headings, see **"Organic Matter Characterization,"** p. 21, in "Organic Geochemistry," in the "Explanatory Notes" chapter.

Table T8. Discrete *P*-wave measurements, Site 1167.

Core, section, interval (cm)	Depth (mbsf)	Direction	Velocity (m/s)	Core temperature (°C)	Method
188-1167A-					
1H-1, 125.3	1.25	y	1505	20.8	PWS2
1H-1, 125.2	1.25	z	1516	20.1	PWS1
1H-2, 45.1	1.95	y	1551	21.1	PWS2
1H-2, 44.8	1.95	z	1553	20.0	PWS1
1H-3, 26.3	3.26	z	1522	20.0	PWS1
1H-3, 28.1	3.28	y	1507	21.1	PWS2
2H-1, 36.4	5.56	y	1656	18.1	PWS2
2H-1, 36.4	5.56	z	1623	18.0	PWS1
2H-2, 33.4	7.03	y	1643	17.9	PWS2
2H-2, 33.3	7.03	z	1776	17.9	PWS1
2H-3, 76.5	8.97	z	1678	19.1	PWS1
2H-3, 77.7	8.98	y	1613	19.2	PWS2
2H-4, 32.5	10.02	y	1641	19.2	PWS2
2H-4, 32.4	10.02	z	1728	19.3	PWS1
2H-5, 34.4	11.54	y	1659	19.3	PWS2
2H-5, 33.7	11.54	z	1706	19.2	PWS1
3H-1, 35.1	15.05	z	1692	19.7	PWS1
3H-2, 35.4	16.55	z	1740	20.2	PWS1
3H-2, 36.4	16.56	y	1572	20.1	PWS2
3H-3, 36.1	18.06	y	1621	19.8	PWS2
3H-3, 36.3	18.06	z	1731	19.8	PWS1
3H-4, 31.0	19.51	z	1772	19.9	PWS1
3H-4, 32.9	19.53	y	1634	19.9	PWS2
3H-5, 38.0	21.08	z	1758	20.0	PWS1
3H-5, 40.2	21.10	y	1642	20.1	PWS2
3H-6, 19.9	22.40	y	1794	20.5	PWS2
3H-6, 19.9	22.40	z	1811	20.4	PWS1
4H-1, 36.9	24.57	x	1934	23.6	PWS3
4H-2, 45.5	26.16	z	1840	20.8	PWS1
4H-3, 81.2	28.01	x	1820	20.6	PWS3
4H-4, 38.9	29.09	x	1965	20.2	PWS3
4H-5, 54.3	30.74	x	1893	20.0	PWS3
5H-1, 54.2	34.24	x	1860	20.3	PWS3
5H-2, 58.4	35.78	x	1895	20.8	PWS3
5H-3, 55.4	37.25	x	1771	21.0	PWS3
5H-4, 43.9	38.64	x	1898	20.9	PWS3
7X-1, 50.1	40.20	x	1889	21.1	PWS3
7X-2, 25.7	41.46	x	1936	20.7	PWS3
8X-1, 55.5	45.56	x	1944	20.7	PWS3
8X-2, 48.2	46.98	x	1955	20.4	PWS3
8X-3, 62.1	48.62	x	1987	20.6	PWS3
8X-4, 60.0	50.10	x	1987	23.2	PWS3
10X-1, 97.8	65.28	x	2054	19.5	PWS3
10X-2, 74.2	66.54	x	1958	19.8	PWS3
10X-3, 79.4	68.09	x	1944	19.5	PWS3
11X-1, 27.8	73.98	x	1903	21.0	PWS3
11X-2, 60.5	74.64	x	1992	20.1	PWS3
11X-3, 55.9	76.09	x	1984	20.1	PWS3
11X-4, 67.4	77.27	x	1984	20.4	PWS3
11X-5, 68.9	78.79	x	1957	20.3	PWS3
11X-6, 69.2	80.29	x	1941	20.5	PWS3
12X-1, 44.4	83.74	x	1904	20.6	PWS3
12X-2, 58.0	85.38	x	2003	19.7	PWS3
13X-1, 75.1	93.75	x	2013	20.1	PWS3
13X-2, 77.3	95.27	x	1911	20.0	PWS3
13X-3, 58.9	96.47	x	1983	19.7	PWS3
13X-4, 71.8	98.10	x	1944	20.0	PWS3
13X-5, 35.7	99.24	x	1922	20.5	PWS3
14X-1, 66.2	103.26	x	2082	19.4	PWS3
14X-2, 69.9	104.80	x	1890	19.3	PWS3
14X-3, 74.6	106.35	x	2028	19.4	PWS3
14X-4, 57.0	107.67	x	2215	20.4	PWS3
14X-5, 70.8	109.31	x	1955	20.4	PWS3
14X-6, 49.9	110.60	x	1925	20.6	PWS3
14X-7, 17.1	111.77	x	1886	20.5	PWS3
19X-1, 98.3	151.28	x	1976	20.4	PWS3
19X-2, 113.0	152.93	x	2053	20.6	PWS3
19X-3, 83.7	154.14	x	2055	20.3	PWS3
19X-4, 39.4	155.19	x	1942	19.7	PWS3
20X-1, 115.2	161.05	x	1984	19.7	PWS3
20X-2, 71.0	162.11	x	1997	19.1	PWS3
20X-3, 33.1	163.23	x	1925	19.0	PWS3
21X-1, 68.8	170.29	x	1944	18.5	PWS3
22X-1, 120.8	180.41	x	1987	19.8	PWS3
23X-1, 17.1	188.97	x	2199	20.6	PWS3
24X-1, 42.4	198.82	x	2117	19.7	PWS3
25X-1, 57.1	208.57	x	1964	20.1	PWS3
25X-2, 54.7	210.05	x	2152	20.6	PWS3
25X-3, 57.9	211.58	x	2103	20.6	PWS3
25X-4, 83.5	213.34	x	2067	20.3	PWS3
25X-5, 81.7	214.82	x	2054	20.2	PWS3
25X-6, 84.3	216.34	x	2036	19.7	PWS3
25X-7, 27.0	217.27	x	1695	20.0	PWS3
25X-7, 27.0	217.27	z	1652	19.8	PWS3
25X-7, 27.0	217.27	y	1714	19.7	PWS3
26X-1, 38.0	217.98	x	2098	22.5	PWS3
26X-1, 38.0	217.98	z	2113	22.6	PWS3
26X-1, 38.0	217.98	y	2109	22.5	PWS3
26X-2, 37.0	219.47	x	2090	22.5	PWS3
26X-2, 37.0	219.47	z	2072	22.5	PWS3
26X-2, 37.0	219.47	y	2129	22.6	PWS3
26X-3, 37.0	220.97	x	2086	22.7	PWS3
26X-3, 37.0	220.97	z	2152	22.7	PWS3
26X-3, 37.0	220.97	y	2117	22.6	PWS3
26X-4, 122.0	223.32	x	2048	22.7	PWS3
26X-4, 122.0	223.32	z	2103	22.6	PWS3
26X-4, 122.0	223.32	y	2058	22.7	PWS3
26X-5, 122.0	224.82	x	2051	22.6	PWS3
26X-5, 122.0	224.82	z	2088	22.6	PWS3
26X-5, 122.0	224.82	y	2063	22.6	PWS3
26X-6, 122.0	226.32	x	2070	22.6	PWS3
26X-6, 122.0	226.32	z	2070	22.6	PWS3
26X-6, 122.0	226.32	y	2065	22.7	PWS3
27X-1, 51.2	227.71	x	2190	20.2	PWS3
28X-1, 67.0	237.57	y	2151	18.8	PWS3
28X-2, 75.4	239.15	x	2570	19.2	PWS3
28X-3, 75.0	240.65	x	2047	18.7	PWS3
28X-4, 76.1	242.26	x	2141	19.0	PWS3
29X-1, 85.9	247.36	x	2117	20.3	PWS3
29X-2, 44.2	248.44	x	2182	20.3	PWS3
29X-CC, 19.7	249.10	x	2191	20.2	PWS3
30X-1, 75.7	256.86	x	2161	20.9	PWS3
30X-2, 87.8	258.48	x	2221	20.4	PWS3
30X-3, 70.0	259.80	x	2181	22.8	PWS3
30X-4, 86.4	261.46	x	2204	19.5	PWS3
30X-5, 49.8	262.60	x	2185	19.3	PWS3
31X-1, 46.3	266.16	x	2136	21.2	PWS3
32X-1, 74.2	276.04	x	2079	20.7	PWS3
32X-2, 65.0	277.45	x	2039	19.9	PWS3
32X-3, 72.5	279.02	x	2076	19.7	PWS3
32X-4, 52.8	280.33	x	2101	19.5	PWS3
32X-5, 76.2	282.06	x	2095	19.8	PWS3
33X-1, 64.6	285.25	x	2090	19.7	PWS3
33X-2, 50.4	286.60	x	2075	19.6	PWS3
34X-1, 69.5	294.60	x	2123	20.1	PWS3
34X-2, 42.3	295.82	x	2129	19.9	PWS3
35X-1, 32.9	303.53	x	2228	18.5	PWS3
36X-CC, 21.4	313.01	x	2111	17.9	PWS3
38X-1, 61.1	332.71	x	2062	20.0	PWS3
38X-2, 47.3	334.07	x	2038	20.4	PWS3
38X-3, 32.5	335.39	x	2139	20.3	PWS3

Notes: PWS1 = *P*-wave sensor 1, PWS2 = *P*-wave sensor 2, PWS3 = *P*-wave sensor 3. Only a portion of this table appears here. The complete table is available in **ASCII format.**

Table T9. Measurements of undrained shear strength, Site 1167.

Automated vane shear data		Fall cone data		Pocket penetrometer data	
Depth (mbsf)	C_u (kPa)	Depth (mbsf)	C_u (kPa)	Depth (mbsf)	C_u (kPa)
1.25	5.21	1.95	12.00	50.10	106.67
1.95	10.20	3.30	11.00	65.28	58.33
3.28	11.09	5.52	28.00	66.54	71.67
5.58	34.60	7.02	24.00	68.09	53.33
7.08	34.60	8.98	28.00	73.98	63.33
8.95	19.52	10.02	18.00	74.64	71.67
10.05	9.09	11.53	22.00	76.09	61.67
11.45	10.98	15.05	60.00	77.27	76.67
16.54	15.97	16.53	30.00	78.79	82.50
16.54	15.97	18.06	38.00	80.29	80.00
18.09	16.08	19.46	72.00	83.76	67.50
19.53	20.18	21.10	72.00	85.38	65.83
21.07	29.39	22.40	80.00	93.75	72.50
22.40	16.74	24.69	80.00	95.27	70.00
24.57	17.41	26.24	80.00	96.47	78.33
26.26	42.91	27.93	62.00	98.10	78.33
27.97	15.86	34.18	103.00	99.24	65.00
29.03	34.49	35.82	103.00	103.26	73.33
30.57	32.60	37.26	59.00	104.80	67.50
34.20	53.67	38.58	190.00	106.35	82.50
35.81	25.39	40.28	88.00	107.60	101.67
37.27	22.62	41.52	119.00	109.35	83.33
38.59	53.11	45.32	170.00	110.50	90.83
40.30	33.16	47.02	175.00	111.85	113.33
40.30	33.16	48.54	275.00	151.28	60.00
47.03	51.23	65.28	140.00	152.93	87.33
48.56	44.24	66.54	155.00	154.14	69.17
		68.09	113.00	155.19	105.00
		73.98	155.00	161.05	81.67
		74.64	175.00	162.11	119.17
		76.09	119.00	163.23	116.67
		77.27	170.00	170.29	125.00
		78.79	235.00	180.40	175.00
		80.29	215.00	188.95	180.83
		83.76	80.00	198.78	153.33
		85.38	113.00	208.58	130.83
		93.75	205.00	210.09	195.00
		95.27	175.00	211.59	171.67
		96.47	190.00	213.38	170.00
		98.10	205.00	214.89	168.33
		99.24	140.00	216.35	193.33
		103.26	99.00	217.30	185.00
		104.80	155.00	218.00	193.33
		106.35	140.00	219.50	111.67
		107.60	155.00	221.00	151.67
		109.35	205.00	222.50	120.00
		110.50	215.00	224.00	146.67
		111.85	235.00	225.50	153.33
		151.28	89.00	226.90	163.33
		152.93	215.00	227.75	164.17
		154.14	155.00	237.63	177.50
		155.19	140.00	239.04	333.33
		161.05	215.00	240.69	210.00
		162.11	175.00	242.30	200.00
		163.23	275.00	247.35	266.67
		170.29	205.00	248.44	192.50
		180.40	235.00	249.10	193.33
		188.95	370.00	256.86	170.00
		198.78	305.00	258.46	211.67
		208.58	205.00	259.75	205.00
		237.58	345.00	261.43	216.67
		239.04	370.00	262.55	213.33
		242.30	305.00	266.17	176.67
		256.86	275.00	276.00	340.00
		258.46	275.00	277.40	195.00
		259.96	345.00	279.00	290.00
		276.00	370.00	280.38	320.00
		277.40	370.00	282.00	413.33
		285.20	305.00	285.20	180.00
		286.55	345.00	286.55	213.33
		294.55	305.00	295.80	353.33
				303.53	353.33
				313.03	256.67
				332.65	290.00
				334.05	236.67
				335.36	373.33
				352.15	306.67
				353.45	320.00
				355.02	293.33
				361.81	460.00
				363.10	406.67
				364.59	343.33
				365.97	543.33
				367.20	553.33
				371.08	486.67
				372.78	286.67
				380.84	266.67
				382.74	430.00
				383.69	620.00
				390.70	500.00
				392.03	450.00
				399.74	513.33
				419.20	480.00
				420.49	1000.00
				429.15	340.00
				430.67	446.67
				431.90	306.67
				433.60	483.33
				434.65	490.00
				438.62	506.67
				439.85	546.67
				442.00	440.00
				443.00	653.33

Note: This table is also available in **ASCII format.**

Table T10. Full-space needle measurements of thermal conductivity, Site 1167.

Core, section, interval (cm)	Top of section depth (mbsf)	Depth (mbsf)	Thermal conductivity measurements (W/[m·°C]) Reading 1	Reading 2	Reading 3	Average
188-1167A-						
1H-1, 75	0.00	0.75	1.059	1.040	1.113	1.071
1H-2, 75	1.50	2.25	1.199	1.209	1.220	1.209
1H-3, 75	3.00	3.75	1.404	1.391	1.389	1.395
2H-1, 75	5.20	5.95	1.747	1.609	1.622	1.659
2H-2, 75	6.70	7.45	1.701	1.744	1.785	1.743
2H-3, 75	8.20	8.95	1.840	1.740	1.786	1.789
2H-5, 50	11.20	11.70	1.906	1.919	1.903	1.909
3H-1, 75	14.70	15.45	1.751	1.726	1.718	1.732
3H-3, 75	17.70	18.45	2.051	2.002	1.945	1.999
3H-5, 75	20.70	21.45	2.044	2.012	2.022	2.026
4H-3, 75	27.20	27.95	1.908	1.812	1.952	1.891
4H-5, 75	30.20	30.95	1.846	1.857	1.908	1.870
5H-3, 73	36.70	37.43	1.582	1.574	1.608	1.588
7X-1, 75	39.70	40.45	1.502	1.599	1.714	1.605
8X-3, 75	48.00	48.75	1.546	1.549	1.452	1.516
10X-2, 75	65.80	66.55	1.283	1.271	1.328	1.294
11X-2, 75	74.03	74.78	1.645	1.663	1.645	1.651
11X-4, 75	76.60	77.35	1.603	1.533	1.706	1.614
11X-6, 75	79.60	80.35	1.532	1.534	1.540	1.535
12X-1, 75	83.30	84.05	1.599	1.627	1.510	1.579
13X-1, 75	93.00	93.75	1.710	1.636	1.607	1.651
13X-3, 75	95.88	96.63	1.610	1.592	1.706	1.636
13X-5, 60	98.88	99.48	1.734	1.632	1.823	1.730
14X-1, 75	102.60	103.35	1.497	1.633	1.603	1.578
14X-3, 75	105.60	106.35	1.672	1.588	1.565	1.608
14X-6, 50	110.10	110.60	1.514	1.497	1.484	1.498
19X-1, 75	150.30	151.05	1.902	1.943	1.759	1.868
19X-4, 40	154.80	155.20	1.732	1.900	1.944	1.859
20X-1, 70	159.90	160.60	1.726	1.546	1.730	1.667
21X-1, 70	169.60	170.30	1.748	1.708	1.651	1.702
23X-1, 17	188.80	188.97	1.651	1.619	1.533	1.601
24X-1, 50	198.40	198.90	1.554	1.759	1.613	1.642
24X-1, 50	198.40	198.90	1.610	1.576	1.541	1.576
25X-3, 80	211.00	211.80	1.729	1.949	1.965	1.881
25X-5, 75	214.00	214.75	2.099	2.201	2.093	2.131
26X-1, 75	217.60	218.35	1.760	1.842	1.823	1.808
26X-4, 75	222.10	222.85	1.980	1.817	1.962	1.920
26X-6, 75	225.10	225.85	1.973	1.960	1.898	1.944
28X-1, 75	236.90	237.65	1.889	1.802	1.838	1.843
28X-3, 75	239.90	240.65	1.804	1.708	1.699	1.737
29X-1, 75	246.50	247.25	1.601	1.713	1.850	1.721
29X-CC, 17	248.90	249.07	1.800	2.017	1.938	1.918
30X-1, 75	256.10	256.85	2.063	2.067	2.047	2.059
30X-3, 75	259.10	259.85	2.157	2.083	2.136	2.125
30X-5, 75	262.10	262.85	1.864	2.022	1.801	1.896
31X-1, 50	265.70	266.20	1.857	1.859	1.719	1.812
32X-1, 74	275.30	276.04	1.910	1.920	1.888	1.906
32X-3, 74	278.30	279.04	1.639	1.801	1.717	1.719
32X-5, 75	281.30	282.05	1.630	1.862	1.704	1.732
33X-1, 75	284.60	285.35	1.911	1.840	1.921	1.891
34X-1, 75	293.90	294.65	1.841	1.983	1.933	1.919
35X-1, 28	303.20	303.48	1.424	1.429	1.421	1.425
37X-1, 75	322.50	323.25	1.731	1.713	1.764	1.736
37X-3, 50	325.50	326.00	2.139	2.121	2.033	2.098
38X-1, 75	332.10	332.85	1.610	1.726	1.702	1.679
38X-3, 50	335.06	335.56	1.964	1.874	1.937	1.925
40X-1, 75	351.30	352.05	1.630	1.702	1.728	1.687
40X-3, 75	354.30	355.05	1.890	1.970	1.834	1.898
41X-1, 75	360.90	361.65	1.847	1.961	1.687	1.832
41X-3, 75	363.90	364.65	2.070	2.036	2.116	2.074
42X-1, 75	370.60	371.35	1.656	1.748	1.714	1.706

Notes: Probe number V00694 was used to take measurements. Only a portion of this table appears here. The complete table is available in **ASCII format.**

Table T11. Measured and estimated temperatures, geothermal gradients, and heat-flow estimates, Site 1167.

Depth (mbsf)	Measured conductivity (W/[m·°C])	Stabilized temperature (°C)	Thermal gradient (°C/km)	Heat flow (mW/m^2)	Average thermal gradient (°C/km)
0.0		**0.09**			
39.7	**1.59**	**0.77**	**17.1**	**27.2**	
40.5	1.61	0.8	17.0	27.2	17.3
48.8	1.52	0.9	18.0	27.2	17.3
66.6	1.29	1.3	21.0	27.2	17.9
74.8	1.65	1.4	16.5	27.2	18.0
77.4	1.61	1.5	16.9	27.2	18.0
80.4	1.54	1.5	17.7	27.2	17.9
84.1	1.58	1.6	17.2	27.2	17.9
93.8	1.65	1.8	16.5	27.2	17.8
96.6	1.64	1.8	16.6	27.2	17.8
99.5	1.73	1.9	15.7	27.2	17.7
103.4	1.58	1.9	17.3	27.2	17.7
106.4	1.61	2.0	16.9	27.2	17.7
110.6	1.50	2.0	18.2	27.2	17.7
151.1	1.87	2.7	14.6	27.2	17.3
155.2	1.86	2.8	14.6	27.2	17.2
160.6	1.67	2.8	16.3	27.2	17.2
170.3	1.70	3.0	16.0	27.2	17.1
189.0	1.62	3.3	16.8	27.2	17.1
198.9	1.58	3.5	17.3	27.2	17.0
211.8	1.95	3.7	14.0	27.2	16.9
214.8	2.20	3.7	12.4	27.2	16.9
218.4	1.84	3.8	14.8	27.2	16.8
222.9	1.82	3.8	15.0	27.2	16.8
225.9	1.96	3.9	13.9	27.2	16.7
237.7	1.80	4.1	15.1	27.2	16.6
240.7	1.71	4.1	15.9	27.2	16.6
247.3	1.71	4.2	15.9	27.2	16.6
249.1	2.02	4.2	13.5	27.2	16.6
256.9	2.07	4.3	13.2	27.2	16.5
259.9	2.08	4.4	13.1	27.2	16.4
262.9	2.02	4.4	13.5	27.2	16.4
266.2	1.86	4.5	14.6	27.2	16.4
276.0	1.92	4.6	14.2	27.2	16.3
279.0	1.80	4.6	15.1	27.2	16.3
282.1	1.86	4.7	14.6	27.2	16.3
285.4	1.84	4.7	14.8	27.2	16.3
294.7	1.98	4.9	13.7	27.2	16.2
303.5	1.43	5.0	19.0	27.2	16.2
323.3	1.71	5.4	15.9	27.2	16.3
326.0	2.12	5.4	12.8	27.2	16.3
332.9	1.73	5.5	15.8	27.2	16.2
335.6	1.87	5.5	14.5	27.2	16.2
352.1	1.70	5.8	16.0	27.2	16.2
355.1	1.97	5.8	13.8	27.2	16.2
361.7	1.96	5.9	13.9	27.2	16.1
364.7	2.04	6.0	13.4	27.2	16.1
371.4	1.75	6.1	15.6	27.2	16.1
382.5	1.63	6.2	16.7	27.2	16.1
392.1	1.80	6.4	15.1	27.2	16.1
429.1	2.00	6.9	13.6	27.2	15.9
432.1	1.93	7.0	14.1	27.2	15.9
438.7	1.63	7.1	16.7	27.2	15.9
437.9	1.61	7.1	16.9	27.2	15.9
441.7	1.51	7.1	18.0	27.2	15.9

Note: Bold numbers show measured values. All others are estimated values based on projection of the temperature gradient.

Table T12. Logging operations summary, Site 1167.

Operations depth summary	Run 1	LWD/MWD	Comments
Holes 1167A and 1167B	Triple combo	Power Pulse CDR	Logging operations commenced at 1700 on 2/27/00. Wiper trip, sepiolite was circulated; no KCl used. Sea state/heave: average 2.5 m; maximum 4.5 m.
Water depth, seafloor or mudline:			
Mudline (mbrf): driller's depth	1651.3		Run into hole speed = 7000 ft/hr.
Mudline (mbrf): logger's depth	1649.0	1652.0	Triple combo uprun speed = 500-900 ft/hr.
Mudline (mbsl)	1640.3	1641.0	LWD/MWD average rate of penetration = 20 m/hr (calculation includes time for making drill-pipe connections).
Drill-pipe depth during logging:			Logging operations ceased at 0930 on 2/29/00.
Initial pipe depth (mbrf): driller's depth	1738.3		
Initial pipe depth (mbsf): using driller's depth	87.0		Initial pipe depth was set at 86.95 mbsf.
Final pipe depth (mbrf): driller's depth	1738.3	1913.1	
Final pipe depth (mbrf): depth from logs	1734.0		
Final pipe depth (mbsf): using driller's depth	87.0	262.1	
Final pipe depth (mbsf): using logger's depth	85.0		Final pipe depth = initial log depth.
Sticking encountered during logging:			
Depth of first bridge or ledge (mbrf; winch)	1740.0		Tool got stuck at a bridge only 12 m below the base of the pipe. Fluid was pumped downhole until pressure increased enough to release the tool.
Depth of first bridge or ledge (mbsf)	91.0		
Depth of second bridge or ledge (mbrf; winch)	1800.0		A second bridge was encountered at 151 mbsf; the tool could not break through this obstruction.
Depth of second bridge or ledge (mbsf)	151.0		
Final tool depth:			
(mbrf; winch)	1800.0	1913.1	
(mbsf): using logger's depth	151.0	261.1	
Total hole depth (m):	447.5	261.1	Wireline logging failed to reach total cored depth; however, the upper 265 m was successfully logged with LWD/MWD.
Length of logging run (m):	66.0	261.1	

Note: CDR = compensated dual resistivity tool; LWD = logging while drilling; MWD = measurement while drilling; mbrf = meters below rig floor; mbsl = meters below sea level.

Table AT1. Summary of accessory components retained on a 125-µm sieve after preparation of foraminifer samples, Site 1167.

Core, section, interval (cm)	Residue size	Planktonic foraminifers	Benthic foraminifers	Planktonic percentage	Sponge spicules	Echinoid spines	Ostracods	Shell fragments	Glauconite	Black coal	Lignite	Detrital pyrite	Diagenetic pyrite
188-1167A-													
1H-CC	L	B	B		X								
2H-CC	L	C	R	94		X				X			
3H-CC	L	R	B							X		X	
4H-CC	L	R	R			X				X		X	
5H-3, 34-36	S	A	C	99		X			X				
5H-CC	S	R	R	61					X	X		X	
7X-CC	L	R	R	72		?				X			
8X-CC	L	C	C	74		X	X			X			
9X-CC	L	R	R	67						X			
10X-CC	L	R	R	78							X	X	X
11X-CC	L	R	R	62							X	X	X
12X-CC	L	C	R	78					X	X		X	
13X-CC	L	R	C	53		X		X		X		X	
14X-CC	L	C	R	82		X		X		X			
17X-CC	L	C	C	84						X			
19X-CC	L	C	C	86						X		X	
20X-CC	L	R	R	78					X	X		X	
21X-CC	L	R	R	78				X		X		X	
22X-CC	L	R	R	74						X	X	X	
23X-CC	L	R	R	67						X		X	
24X-CC	L	R	R	84						X		X	
25X-CC, 22-23	S	A	R	99		X	X		X				
25X-CC	L	B	B							X		X	X
26X-CC	L	B	B							X		X	
27X-CC	L	R	B	100						X	X		
28X-CC	L	B	B							X		X	
29X-CC	L	B	B							X		X	
30X-CC	L	R	B	100						X		X	
31X-CC	L	B	B							X		X	
32X-CC	L	C	R	83						X			
33X-CC	L	B	R	0						X		X	
34X-CC	L	B	B									X	
35X-1, 68-73	L	R	B	100									
35X-CC													
36X-CC	L	C	R	98									
37X-CC	L	R	B	100									
38X-CC	L	R	R	67						X		X	
39X-CC	L	C	R	95		X							
40X-CC	L	B	B							X		X	X
41X-CC	L	R	R	88									
42X-CC	L	C	B	100									
43X-CC	L	C	R	84						X		X	
44X-CC	L	B	B									X	
45X-CC	L	B	B										
46X-CC	L	R	R	75						X		X	
47X-CC	L	B	B										
48X-CC	L	A	C	89						X		X	X
49X-CC	L	B	B							X		X	

Notes: Planktonic percentage = planktonic foraminifers as percentage of total foraminifers. Residue size: L = large, S = small. Foraminifers: A = abundant, C = common, R = rare, B = barren. Other components: X = present, ? = uncertain identification.